X-ray astrophysics of compact objects

by Anna Marishka Krickovich LeRoux

A thesis submitted in partial fulfillment of the requirements for the degree of Doctor of Philosophy in Physics
Montana State University

Abstract:
Seyfert galaxies have long been known to exhibit rapid X-ray Variability. As yet, no definitive mechanism for this variability has been identified, but shocks and flare-like events have been suggested as viable possibilities. An ASCA observation of the galaxy NGC 3227 had flares which followed a linear increase and exponential decrease, which is the same pattern followed by solar flares. Using the same techniques previously used to derive scaling laws for solar flares, a scaling law for flares on the accretion disks of AGN is derived. The law relates the loop length to the loop apex temperature, rise time, and decay time of the flare in the light curve, and from the data obtained from the observation of NGC 3227, the flarelike events are consistent with a physically viable region in the parameter space of loop length and apex temperature. Thus, at least by this measure, flares caused by magnetic loops remain a physically viable mechanism for AGN variability.

Observations of Seyfert Galaxies, whether by ASCA or by other satellites, have previously divided the data of long observations by observation time or by luminosity to create spectra which average over one of these. Here an alternative method for classifying bins in the light curve according to hardness is developed, and correlated to the phenomenology of the light curve. This method is applied to the 1994 150 ks exposure ASCA observation of MCG-6-30-15. The results are that, when coupled with very conservative spectral fitting techniques, the new extraction technique suggests that local minima and maxima are spectrally different from other regions of the light curve with the same luminosity. The Seyfert galaxy Arkarian 120 is also analyzed, but has too short an exposure to extract statistically viable spectra. The spectral fitting of this source shows no evidence for a warm absorber, but suggests a soft energy excess due to blackbody radiation.

chapterdottedtocline00em2.3em

X-RAY ASTROPHYSICS OF COMPACT OBJECTS

by

Anna Marishka Krickovich LeRoux

A thesis submitted in partial fulfillment
of the requirements for the degree

of

Doctor of Philosophy

in

Physics

MONTANA STATE UNIVERSITY — BOZEMAN
Bozeman, Montana

April 2000

APPROVAL

of a thesis submitted by

Anna Marishka Krickovich LeRoux

This thesis has been read by each member of the thesis committee, and has been found to be satisfactory regarding content, English usage, format, citations, bibliographic style and consistency, and is ready for submission to the College of Graduate Studies.

Sachiko Tsuruta, Ph. D. ______________ (Signature) 4/15/2000 Date

Approved for the Department of Physics

John C. Hermanson, Ph. D. ______________ (Signature) 4-15-2000 Date

Approved for the College of Graduate Studies

Bruce McLeod, Ph. D. ______________ (Signature) 4-17-00 Date

STATEMENT OF PERMISSION TO USE

In presenting this thesis in partial fulfillment of the requirements for a doctoral degree at Montana State University — Bozeman, I agree that the Library shall make it available to borrowers under rules of the Library. I further agree that copying of this thesis is allowable only for scholarly purposes, consistent with "fair use" as prescribed in the U. S. Copyright Law. Requests for extensive copying or reproduction of this thesis should be referred to University Microfilms International, 300 North Zeeb Road, Ann Arbor, Michigan, 48106, to whom I have granted "the exclusive right to reproduce and distribute my dissertation in and from microform along with the non-exclusive right to reproduce and distribute my abstract in any format in whole or in part."

Signature [signature]

Date April 16, 2000

ACKNOWLEDGEMENTS

I would like to thank a number of individuals who have made the thesis-writing process survivable. I would like to thank Sachiko Tsuruta for her guidance as a thesis advisor, and also Dana Longcope and George Fisher for extensive discussion of solar flares and magnetic reconnection. I would further like to thank Hideyo Kunieda for providing much of the data analyzed in this thesis, and for extremely helpful comments on spectral fitting techniques.

I would also like to thank the large number of additional individuals in physics who have read and critiqued parts of my thesis, particularly, Loren Acton, Jyostna Krishnamoorthi, and Darrell Rilett. I would also like to thank the two non-physicists who have done extensive technical editing for me- my two dads, Jeff LeRoux and Everett Hansen. I would also like to thank my mother for taking care of me during the very last days of writing. Writing in absentia is an undertaking in itself, and I would like to acknowledge those of my colleagues who have been particularly supportive in the more difficult times, Frank Herrmann and Michelle Volken.

TABLE OF CONTENTS

LIST OF TABLES

LIST OF FIGURES

ABSTRACT

Seyfert galaxies have long been known to exhibit rapid X-ray variability. As yet, no definitive mechanism for this variability has been identified, but shocks and flare-like events have been suggested as viable possibilities. An ASCA observation of the galaxy NGC 3227 had flares which followed a linear increase and exponential decrease, which is the same pattern followed by solar flares. Using the same techniques previously used to derive scaling laws for solar flares, a scaling law for flares on the accretion disks of AGN is derived. The law relates the loop length to the loop apex temperature, rise time, and decay time of the flare in the light curve, and from the data obtained from the observation of NGC 3227, the flarelike events are consistent with a physically viable region in the parameter space of loop length and apex temperature. Thus, at least by this measure, flares caused by magnetic loops remain a physically viable mechanism for AGN variability.

Observations of Seyfert Galaxies, whether by ASCA or by other satellites, have previously divided the data of long observations by observation time or by luminosity to create spectra which average over one of these. Here an alternative method for classifying bins in the light curve according to hardness is developed, and correlated to the phenomenology of the light curve. This method is applied to the 1994 150 ks exposure ASCA observation of MCG-6-30-15. The results are that, when coupled with very conservative spectral fitting techniques, the new extraction technique suggests that local minima and maxima are spectrally different from other regions of the light curve with the same luminosity. The Seyfert galaxy Arkarian 120 is also analyzed, but has too short an exposure to extract statistically viable spectra. The spectral fitting of this source shows no evidence for a warm absorber, but suggests a soft energy excess due to blackbody radiation.

chapterdottedtocline00em2.3em

CHAPTER 1

INTRODUCTION

Now you have just been able to reduce the countless embattled troops to an array that is, to be sure, very large but still calculable in a finite number; but this relative relief is undermined by the ambush of the Books Read Long Ago Which It's Now Time To Reread and the Books You've Always Pretended to Read And Now It's Time To Sit Down and Really Read Them.

(Italo Calvino, **If on a Winter's Night a Traveler**)

Introduction

In 1962 Giacconi discovered X-rays from Scorpius X-1 (Giacconi *et. al.* 1962), marking the beginning of X-ray studies of compact objects. While Cygnus X-1 is thought to consist of an accretion disk orbiting a Galactic black hole of less than $20M_{sun}$, the accretion disks orbiting the 10^8 solar mass black holes thought to exist in the centers of active galaxies, which include quasars and Seyfert galaxies, can also be analyzed in the X-ray window. These galaxies are characterized by their bright nuclei, which typically have luminosities between 10^{41} erg s^{-1} and 10^{47} erg s^{-1}, of which a large fraction occurs in the X-ray spectral region. The generally accepted disk-corona model suggests that the disk is surrounded by a hot corona, and hard X-rays are produced by inverse Compton processes on the lower energy photons from the disk.

Seyfert 1 galaxies are a relatively quiet relation in the family of active galaxies, having luminosities near 10^{44} erg s^{-1} in the X-ray band, broad permitted and narrow forbidden optical lines, and relatively weak radio emission. Seyfert 2 galaxies typically show only forbidden transitions in the optical region and exhibit strong emission in the UV. Seyfert 1 galaxies are related to the brighter Quasi-Stellar Objects (QSO) in that they are radio-quiet and typically associated with spiral galaxies, although QSO's generally have X-ray fluxes one or two orders of magnitude larger than Seyfert 1 galaxies and tend to be located at higher redshift. Quasi Stellar Radio Sources (QSR's) are radio-loud, but are as bright as QSO's and have broad lines. Both kinds of Seyfert galaxy, QSO, and QSR are associated with spiral galaxies. Radio galaxies are radio-loud, and are often associated with giant elliptical galaxies. BL Lacertae objects, named after the first known example, are galaxies with very few broad emission lines, and vary rapidly ($\tau < 1$ day) in both the optical and X-ray. LINERS (Low Ionization Nuclear Emission-Line Regions) show lower ionization states than do other AGN, and are often associated with elliptical galaxies. Generally, radio galaxies, BL Lac galaxies, and Optically Violent Variables (OVV's) are associated with elliptical or S0 galaxies, while QSO's, QSR's and both flavors of Seyfert galaxies are associated with early spiral galaxies (Woltjer, 1990). Starbursts galaxies are associated with both spiral and elliptical morphologies (Aretxaga, 1996).

X-ray Observation of Seyfert Galaxies

In the 1970's, X-ray observation was done with temporary missions on satellites. Such missions discovered X-rays from 3C273, the first AGN to show X-ray emission (Bowyer *et. al.*, 1970). HEAO-1 was launched in 1977, and provided the first map of the X-ray sky. In addition, the telescopes of HEAO-1 made the first measurements of the X-ray spectra of quasars and Seyfert galaxies, showing the now well known power-law spectrum they exhibit in that spectral window. In 1978, the Einstein observatory was launched. Spectra from Einstein had emission lines which were noticeably red-shifted from their nominal values; from this, researchers concluded that AGN are receding. In addition, the first evidence of fluorescence from cold iron was observed in Centaurus A (Mushotzky *et. al.* 1978).

A spectral survey performed by EXOSAT showed that AGN had a 2–10 keV spectrum which was well-described by a simple powerlaw model, but had rapidly varying soft energy features and "leaky" absorption columns (Turner and Pounds 1988); that is, absorption columns which only partially cover the continuum radiation. The photon index of the 48 measured AGN was found to be $\Gamma = 1.7 \pm 0.17$, with a few outlier objects. GINGA observations of Seyfert galaxies provided the first measurement of the iron Kα emission line and the cold reflection hump. These two features are thought to originate on the innermost accretion disk; the ionized iron line provides information about the ionization state of the disk, and the reflection hump size is directly proportional to the column density of material in the disk and the solid angle Ω of the thickness of the disk. ROSAT was designed to measure soft X-rays from AGN and neutron stars; observations with ROSAT first showed the presence of a large neutral hydrogen column in the line of sight of many AGN. This hydrogen column is thought to exist mostly in our own galaxy, with an excess occurring in the interstellar medium and in the outer regions of the AGN itself.

Unified Model of Active Galactic Nuclei

While it has been postulated that interactions with neighboring galaxies play some role in the origin of AGN, at least some studies suggest that the occurrence of Seyfert galaxies with close companions is no higher than for normal galaxies (de Robertis *et. al* 1998). In order to explain the differences between varieties of AGN, the *Standard Model* of AGN has been developed (see, for example, Rees,1997). The underlying premise of the standard model is that the structure of all active galaxies is the same: the hard X-rays and γ-rays are produced from an inner accretion disk, which runs perpendicular to the radio jets produced by the object. The inner accretion region is surrounded by a plasma which absorbs and reflects the continuum, referred to as the broadline region (BLR), which is in turn surrounded by a torus of molecular gas. Outside this torus lies the narrowline region (NLR), which consists of a less dense plasma. Outside this lie the nebulae and stars which comprise the outer regions of all galaxies. This model is illustrated in Figure 1.1.

Seyfert galaxies and quasars are thought to form the class of objects with high accretion rates, while radio galaxies are thought to form the class of objects for low accretion rates. LINERS are thought to correspond to rare objects for which we are viewing the galaxy directly along its rotation axis, which dominates the continuum

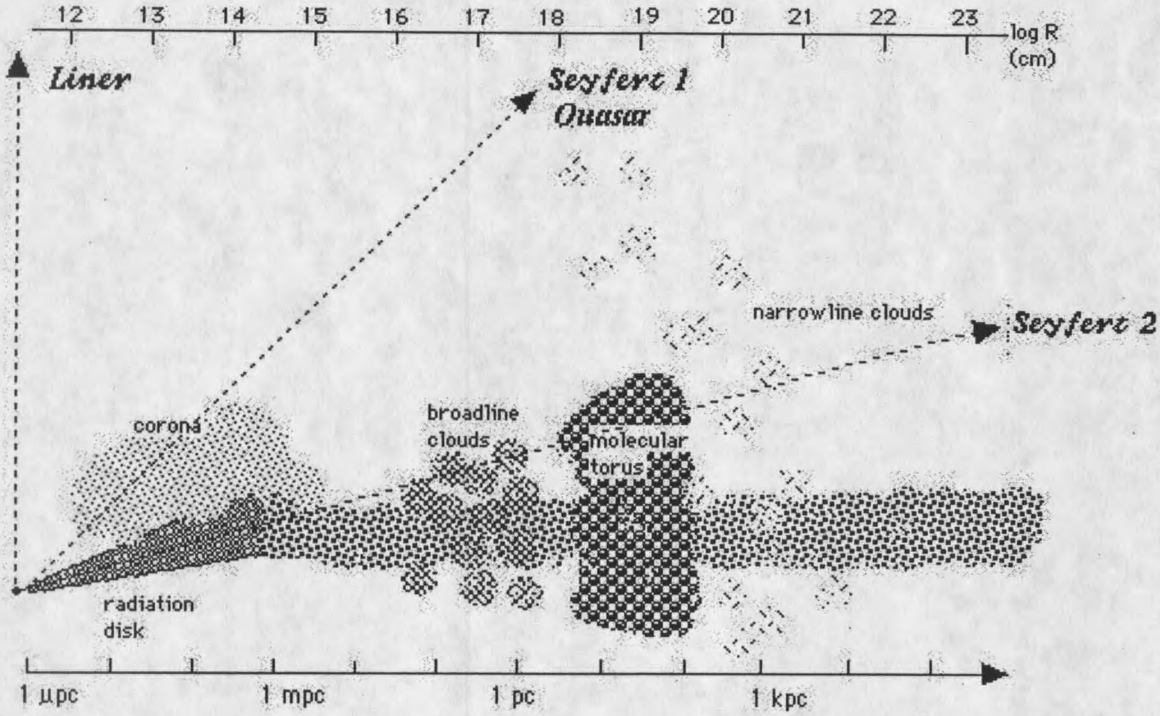

Figure 1.1: Unified Model for Active Galactic Nuclei.

radiation. Seyfert 1 galaxies and QSO's correspond to viewing angles which vary from just off the line of sight of the jet to just grazing the broadline clouds of the galaxy. Seyfert 2 galaxies correspond to high viewing angles (close to edge-on) which require photons to travel through the molecular torus, although the dearth of high-luminosity Seyfert 2 galaxies suggests that molecular tori are thin or unstable under such conditions (Osterbrock, 1993).

More recently, the broadband continuum of some members of the AGN family has been modeled with advection dominated accretion flows, in which the high-energy radiation is produced from the disk itself. The presence of the iron Kα emission line and the Compton reflection hump in Seyfert 1 galaxies strongly contraindicates that their accretion disks are advection-dominated (Ptak *et. al.*, 1998), so the objects observed in this work are analyzed with reference to the standard α disk model (Shakura and Sunyaev, 1973).

While aesthetically pleasing, the standard model does have some inconsistencies with observation. Seyfert 2 galaxies have a far stronger UV continuum and a far weaker hard X-ray continuum than one would predict from reasonable models of the torus of molecular clouds, suggesting that they have less active central engines and more active star forming regions than do Seyfert 1 galaxies. In addition, careful study of the environments of Seyfert galaxies indicates that Seyfert 2 galaxies are far more likely than either Seyfert 1 galaxies or an equivalent population of normal galaxies to have large companion galaxies, suggesting that tidal interactions, and not only obscuration of the BLR and nucleus by a molecular torus, may play a part in the formation of Seyfert 2 galaxies (Dultzin-Hacyan *et. al.*, 1999).

X-ray Variability of AGN

The X-ray continuum of many AGN varies by a full factor of 100 % of its baseline value over timescales of hours. The X-ray and UV spectra of most AGN are variable (Elvis *et. al.*, 1978). A recent study of 24 Seyfert 1 galaxies found that most varied significantly (Reynolds, 1997). Typical X-ray variability of a Seyfert galaxy is shown in Figure 1.2, which shows a 1993 observation of NGC 4593.

The exact mechanism of the rapid X-ray variability in AGN is not known. One theory was that hot spots on the accretion disk were orbiting the black hole with some angular velocity as they accreted material, thus causing variations in the X-ray luminosity. Were this the case, we would expect to see a periodic component in the

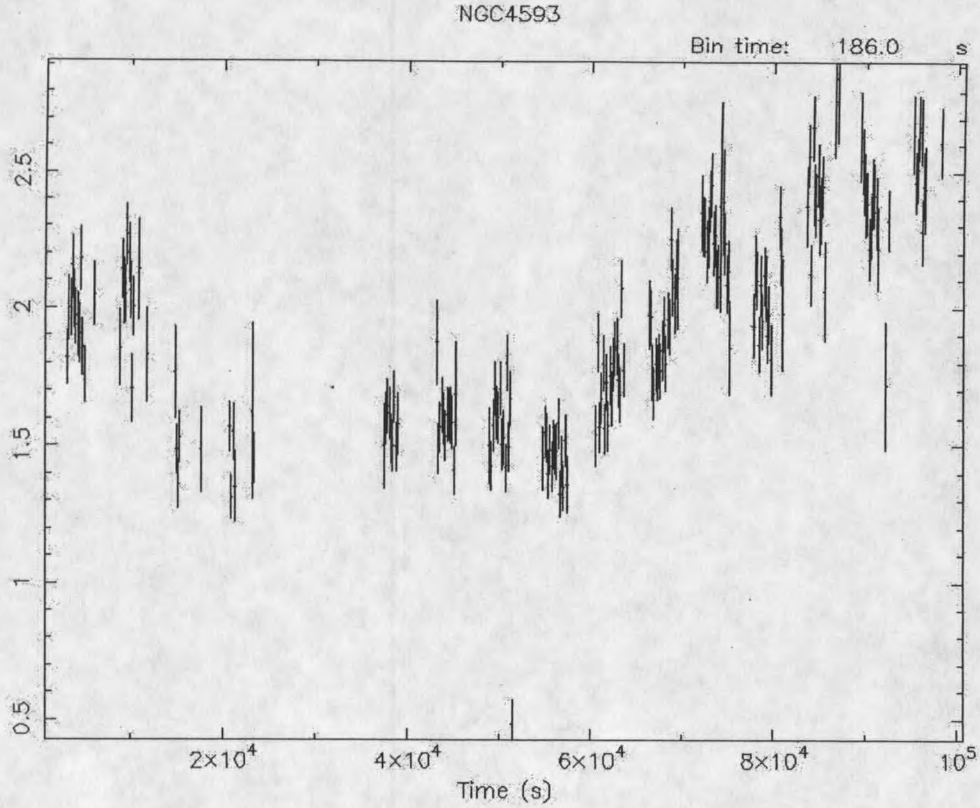

Figure 1.2: Light curve of NGC 4593. The flare maximum is double the baseline luminosity of the galaxy. This light curve was made by the author from an archival ASCA observation of NGC 4593.

power spectrum of the X-ray light curve which was associated with the rotational period of such a hot spot, and this is emphatically contrary to observation (Kuras, 1997). Another possible source of the variation is ionizing shocks which move through the accretion disk (Caditz, Tsuruta, Sivron 1997); this possibility is still viable and may prove to be the source of variation in many objects. Another possibility is that magnetic flux tubes in the AGN's radiation disk are pushed out of the disk by buoyancy forces, creating a tube of hot plasma similar to those which host flares in the solar corona. This possibility was first explored by Rosner, Tucker and Vaiana (1978). who hypothesized that the corona of an accretion disk around a Galactic black hole such as Cygnus X-1 consists of a forest of flare loops anchored in the accretion disk.

Solar and stellar flares have well-studied scaling laws which relate the loop length L to the temperature T of the loop plasma and the rise and decay times of the flare, represented by τ_R and τ_D respectively. These are based on assumptions about the energy balance of the loop plasma during various stages of the flare (Fisher and Hawley, 1990) and have also been found to apply to at least one X-ray star (Hawley *et. al.* 1995). The scaling law for stellar and solar flares is (Metcalf and Fisher, 1996):

$$2L = 0.0126\tau_R^{3/7}\tau_D^{4/7}T^{1/2}, \tag{1.1}$$

so longer loops of the same temperature have longer rise and decay times. This scaling law is based on cooling by thermal bremsstrahlung alone in a region of plasma cooling curve where the photon emissivity is proportional to $T^{1/2}$ (Raymond and Smith, 1977). The hotter, denser plasmas expected from models of AGN radiation disks would not only have a different dependence of emissivity on temperature, they would also have the additional cooling mechanism of inverse Compton scattering. These two factors give rise to a new scaling law for AGN flare loops.

The X-ray spectrum of at least some AGN also varies during luminosity changes. Galactic black hole candidates show five distinct states during a flare cycle which can be explained by a magnetic reconnection model of flares (Di Matteo, Celotti, and

Fabian, 1998), but as yet the X-ray variation of AGN does not follow such a simple pattern. The warm absorber of the Seyfert 1 galaxy MCG-6-30-15 has been seen to vary during luminosity variations (Otani *et. al.*, 1995) as has the Iron Kα line (Tanaka *et. al.*, 1995).

In this work, a new scaling law is derived for AGN flares and used to predict the loop length of a magnetic flux tube associated with two large flares during an ASCA observation of NGC 3227, discussed in Chapter 2 of this work. This loop length allows us to evaluate the feasibility of reconnection of magnetic flux tubes as a mechanism of AGN variability in terms of energetics, pressure balance, and consistency with spectral (non-) variability of the AGN continuum slope during flares.

Structure of the Warm Absorber and Broadline Region

ROSAT observations first showed the presence of O VIII absorption in the soft X-ray spectrum of Seyfert Galaxies (Nandra and Pounds, 1992). Outside the inner accretion disk and its corona lie the broadline clouds. Since they exhibit a variety of emission and absorption features, optical spectra of the broadline region can be used to study the composition of the broadline plasma. When ASCA was launched in 1993, the soft X-ray region from 0.5–2.0 keV of many Seyfert 1 galaxies showed two absorption edges; one near 0.87 keV corresponds to O VIII and another near 0.72 keV corresponds to O VII (Ferland, 1993). The plasma containing these lines was duly christened the warm absorber. In early analysis, the warm absorber was thought to be located near the broadline region, 10^{18} cm from the central black hole.

A variety of analytical tools are available for analyzing the warm absorber. Study-ing the variation of individual line features is one means of doing this; from the timescale of variation of a spectral feature, we can infer the maximum distance between that feature and the central black hole. A macroscopic plasma cannot change state faster than the light-crossing time of the plasma, so the maximum radius, R_{max}, of a plasma which varies on a minimum timescale τ must be:

$$R_{max} = \frac{c}{\tau}. \tag{1.2}$$

As plasma could hypothetically vary more slowly than the light-crossing time as well, so lack of variation of a spectral feature on a particular timescale does not necessarily require that it is located further from the nucleus than the light crossing time.

The exact structure of the warm absorber is also an open research question. Most studies to date have suggested that the warm absorber is one (presumably inhomogeneous) region of gas and dust spanning a radial region from 10^{14} cm to 10^{17} cm from the central black hole. Timescale variations of O VII and O VIII in MCG-6-30-15 suggested that the warm absorber had two distinct regions, one located 10^{17} cm from the central black hole and containing O VIII and the other located 10^{19} cm from the central black hole containing predominantly O VII (Otani *et. al.* 1995). The argument here was based not only on the timescale of variation of each oxygen edge, but also on the recombination physics of O VIII; had the two been located in the same region, O VII would decrease during periods of increased luminosity as it was promoted to O VIII, although the timescale of recombination, which is much larger than that of ionization, limits the probability that an increase in O VII could be rigorously correlated to luminosity changes. No other AGN with similar warm absorber structure has been identified to date.

In addition, a variety of photoionization codes are available for modeling, including the widely used CLOUDY (Ferland, 1996), the less dominant ION (Netzer 1993), and the shock treatment of MAPPINGS (Dopita *et. al.* 1995). These models all produce at least two variable parameters when translated into a model for data analysis; first, an ionization parameter, which is defined as:

$$U_x = \int_{0.1keV}^{10keV} \frac{Q(E)}{4\pi n_H r^2} dE \qquad (1.3)$$

by ION, where Q(E) is the radiation density at energy E, n_H the equivalent hydrogen density, and r the distance of the absorptive material from the central engine. The other variable in all of these codes is the column density of photoionized gas, N_h. Many models also contain other parameters, such as the composition of the plasma, the shape and filling factor of the gas, and the photon index of the continuum spectrum which causes the ionization. In this work, we use ION as a one-zone photoionization model of the warm absorber region because it is valid for plasmas closer to the inner accretion disk than are any of the other models.

Contents of this Work

In this thesis, we will attempt to discuss some of the open issues regarding the structure and dynamics of Active Galactic Nuclei discussed above by analyzing ASCA data. In Chapter 2, we explore the magnetic reconnection of flux tubes as a possible mechanism for X-ray variability of AGN by deriving a scaling law similar to that used for solar flares and comparing it to an observation of the Seyfert 1 galaxy NGC 3227. In Chapter 3, we describe models of the warm absorber, X-ray continuum, and iron Kα emission line which are later used to analyze two Seyfert 1 galaxies: Arkarian 120 and MCG-6-30-15. Chapter 3 also describes analysis techniques developed by the author to sort light curves according to phenomenology (that is, where they occur in a flare cycle) to address the question of X-ray spectral variability during luminosity changes. Chapter 3 is supplemented by Appendix A, which describes the models and fitting statistics used for spectral data analysis. Chapter 4 describes the analysis of the Seyfert 1 galaxy Arkarian 120. Chapter 5 describes both the modification of the method of spectral selection developed by Kunieda and its application to the analysis of the Seyfert 1 galaxy MCG-6-30-15, and is supplemented by the specific measurements in Appendices B through E. Chapter 6 presents concluding remarks on subjects discussed throughout the thesis. All tables and figures in the thesis are the work of the author unless otherwise stated.

CHAPTER 2

CAN MAGNETIC FLUX TUBES CAUSE AGN VARIABILITY

Le soleil se noyait dans son sang qui se fige.

-Baudelaire, "Harmonie du soir", **Fleurs du Mal** [1]

Introduction

Why do Seyfert galaxies vary in luminosity by more than 100% ? X-ray observation of most bright Seyfert galaxies show luminosity variations of 10^{43} erg s^{-1} on timescales as short as minutes (Kunieda *et. al.*, 1990) although higher luminosity Seyfert galaxies have smaller luminosity changes (Barr and Muschotzky, 1986). Since currently accepted theories of the innermost structure of AGN require extraction of energy from the material accreting onto a central black hole, the mechanism of these variations may cast light onto the very nature of the central engine. Fourier phase analysis has shown that the orbit of bright spots on the accretion disk near the core of an AGN cannot account for all of the observed AGN variability (Kuras, 1997).

[1] trans: *The sun is drowning in its clotting blood.* (-Baudelaire"Harmony of the Evening", **Fleurs du Mal**)

In 1977 Rosner, Tucker and Vaiana suggested that the AGN corona consists of many magnetic flux tubes emerging from the relatively cool, dense accretion disk orbiting a black hole. This model has been used in explaining how individual flare loops on an accretion disk can cause changes in the Iron Kα line shape (Begelman, 1998). Recently Di Matteo (1998) has explored the possibility that AGN variability results from reconnection of magnetic flux tubes by Petschek reconnection. Despite the fact that numerical simulations have shown that Petschek reconnection is not a viable mechanism for magnetic reconnection (Biskamp, 1986) many of DiMatteo's results are independent of reconnection mechanism and thus remain valid for Sweet-Parker reconnection. This model of magnetic flares has also been used to explain spectral changes in galactic black holes (Poutanen and Fabian, 1999).

A cartoon of a magnetic flux tube is shown in Figure 2.1; the flux tube of total length 2L is anchored to a high-density, low-temperature medium, which might be the chromosphere for a solar flux tube or the inner accretion disk for an AGN. When energy is deposited into the tube by the flare, material below the foot points evaporates and travels upward through the flux tube. The exact heating mechanism is not known for flux tubes; its magnitude can be determined by observation in solar (Kankelborg, Walker, and Hoover 1997) and stellar (Fisher and Hawley, 1990; hereafter, FH90) flares, in which the rise and decay times of the flare event and the apex temperature can be measured independently. As the heating mechanism diminishes, the cooling processes dominate, resulting in decay of the luminosity. Most of the cooling occurs at the loop foot points as the density is higher there, although the

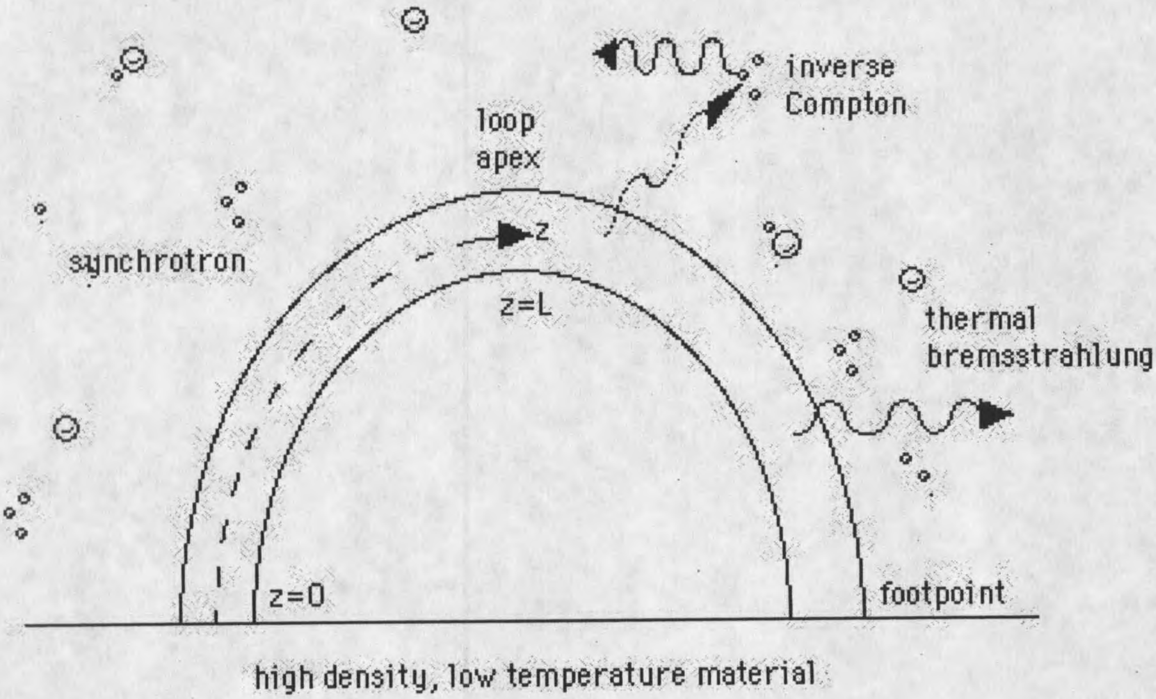

Figure 2.1: A magnetic flux tube anchored to a lower-temperature disk creates part of the hot plasma of an AGN accretion disk.

apex is hotter (FH90). A scaling law which relates the rise time, decay time, and loop plasma temperature to the loop length was first derived by (FH90) and extended to flares on the dMe flare star AD Leonis (Hawley *et. al.* 1995).

Magnetic reconnection is hypothesized to cause solar flares (Lin and Hudson, 1976) and flares in X-ray stars (Hawley *et. al.* 1995); while the exact mechanism of converting magnetic energy into thermal energy is the subject of continued research, the effects of this energy release on the solar plasma are well understood from study of solar flares and X-ray bright points. We naturally expect that there will be some differences between the flares on the Sun or AD Leonis and those on an AGN. Solar and stellar chromospheres host flux tubes that radiate predominantly by thermal bremsstrahlung (FH90). In contrast, an AGN plasma has cooling dominated by self-Comptonized synchrotron radiation and pair production and annihilation mechanisms, although thermal bremsstrahlung is still present (Blandford, 1990). Solar flares have X-ray luminosity that is correlated to their white-light luminosity (Canfield *et. al.*, 1986) while the X-ray and optical luminosities of AGN are not correlated (Muschotzky, Done and Pounds, 1993). The length of flux tubes which create solar flares, that are associated with temperatures of 10^7 K and densities of 10^{10} cm^{-3}, are typically 10^9 cm (Metcalf and Fisher, 1996); in contrast, AD Leonis had calculated flare lengths near 2×10^{10} cm (FH90).

In this chapter, I develop a scaling law for flares in the corona of an AGN accretion disk. Since the flare rise and decay time are measurable, this allows us to determine an allowed region in the parameter space defined by loop length and apex temperature evaluate the feasibility of this model. The strong similarity between X-ray emissivity of solar flares and those found in ASCA observations of Seyfert 1 galaxies suggests that the underlying mechanisms may be related. Thus, following the same methodology of deriving a scaling law from the plasma dynamics in a solar flare, as previously done by Fisher and Hawley (1990), I will develop one for AGN, taking into account the differences between plasma parameters and cooling mechanisms, using NGC 3227 as a test case.

In this chapter, we explore whether the flares observed in the Seyfert 1 galaxy NGC 3227 are consistent with scaling laws from a single reconnection event such as a solar flare. In Section 2.2, the calculations of FH90, in which they derived a scaling law for solar flares, are summarized. In Section 2.3 a similar scaling law is derived for

AGN for a temperature range of 10^5 - 10^{10} K. In Section 2.4 the flares of the Seyfert 1 Galaxy NGC 3227 are analyzed, and changes in spectral hardness briefly addressed. In Section 2.5 we calculate the maximum energy produced by a flux tube consistent with the scaling law, and compare the length to the pressure scale height of the disk and sound transit length of the loop. Section 2.6 contains concluding remarks.

Scaling Law for Solar and Stellar Flares

A scaling law relating the loop length of solar flares to apex temperature, flare rise time, and flare decay time was first derived in FH90. Here their work is summarized in order to clarify the modifications by the author, presented in the later sections of this chapter.

We begin by writing the gas dynamic equations for the plasma in a loop with uniform pressure and constant cross section; we first have the equation of state for the plasma:

$$P = 2nkT \tag{2.1}$$

where we make the simplifying assumption that electrons and ions have the same density n and temperature T. We can consider the loop a one-dimensional entity based on similar loops in the Sun, which have cross sectional areas which are small relative to the length. The remaining spatial dimension, z, is the distance along the arc of the loop. We also have continuity:

$$\dot{n} + \frac{\partial}{\partial z} nv = 0 \tag{2.2}$$

and conservation of energy (as per FH90):

$$\frac{3}{2}\dot{P} = Q - R - \frac{5}{2}P\frac{dv}{dz} - \frac{dF_c}{dz} \tag{2.3}$$

where P is the pressure in the flare loop, Q the heating rate of the plasma, R the cooling rate of the hot plasma, F_c the conductive flux of the plasma, v the plasma velocity and z the distance from the foot point along the flux tube. The plasma is assumed to be an ideal gas, and the cooling law is assumed to have the form:

$$R = n^2AT^{\alpha} \tag{2.4}$$

where n is the plasma density, A=$10^{-10.4}$ and α=$\frac{1}{2}$ for chromospheric temperatures near 10^5 K (FH90). The conductive flux is described by:

$$F_c = \kappa_0 T^{\frac{5}{2}}\frac{dT}{dz} \tag{2.5}$$

where κ_0=10^{-6} cgs is the Spitzer heating constant. The energy conservation equation is then integrated over the loop, yielding:

$$\frac{3}{2}\dot{P} =< Q > - < R > -\frac{5}{2}Pv_{ch} \tag{2.6}$$

where the heat flux is zero at the loop's foot points, and the pressure is assumed uniform throughout the loop. Here the velocity v_{ch} in the enthalpy term is the bulk electron velocity in the chromosphere. The enthalpy term does not vanish, but can be shown (FH90) to be significantly smaller than the other terms in the equation, giving:

$$\frac{3}{2}\dot{P} = < Q > - < R > . \tag{2.7}$$

Earlier numerical simulations of coronal loops (Craig, McClymont, Underwood, 1979; McClymont and Craig 1987) have shown that the spatial velocity distribution is:

$$v(z) = \frac{\dot{N}_t}{n(z)}\left[1 - \frac{N(z)}{N_t}\right] \tag{2.8}$$

where N(z) is the integrated density, or column depth, and is defined by:

$$N(z) = \int_0^z n(z')\, dz'. \tag{2.9}$$

We then relate the pressure to the total column depth N_t(which is just the value of the column depth when z=l):

$$\frac{\dot{N}_t}{N_t} = \Omega \frac{\dot{P}}{P} \tag{2.10}$$

where Ω is a parameter determined by the loop properties, and changes as the loop evolves from evaporative to condensing states. The parameter Ω is an ad hoc parameter created to cover boundary conditions during the various stages of loop evolution. The relation between column depth and pressure is key to the dynamics of the loop; thus, we examine values for Ω in the strongly evaporating and strongly condensing limits. During strong evaporation, the flux tube is filling with plasma, so we expect that it heats very quickly and $\Omega << 1$.

Strongly Evaporating Loops

Here the most important steps in the derivation of the expressions for maximum pressure and Ω for a strongly evaporating loop are presented; all calculations are due to FH90, and are presented here so that they may be referenced later for the work of the author. During the initial phase of loop formation, heating dominates the loop dynamics; that is, $< Q >>>< R >$. The integrated energy equation gives

$$\frac{3}{2}\dot{P} =< Q > - < R >\approx< Q > \tag{2.11}$$

so that the local energy equation, following the previous assumptions that the pressure and heating are uniform throughout the loop, becomes by substitution

$$\frac{dF_c}{dz} + \frac{5}{2}P\frac{dv}{dz} = 0. \tag{2.12}$$

Integrating and defining

$$x = \frac{N}{N_t} \tag{2.13}$$

so that, using the definition of the semi-loop length L, and the fact that the apex has a higher temperature than do the foot points,

$$L = \frac{kN_t}{P}\left(\frac{15k^2\dot{N}_tN_t}{\kappa_0 P}\right)^{2/3} \int_0^1 (x - \frac{1}{2}x^2)^{2/3}, dx. \tag{2.14}$$

We then define a parameter

$$\eta = \int_0^1 (x - \frac{1}{2}x^2)^{2/3}, dx \qquad (2.15)$$

which, when integrated numerically, has the value $\eta = 0.4656$, and the loop half-length is:

$$L = \frac{2\eta N_t k}{P}\left(\frac{15k^2 \dot{N}_t N_t}{\kappa_0 P}\right)^{2/3}. \qquad (2.16)$$

This can then be rewritten to give an expression for the pressure:

$$P = \frac{22^{2/3}\eta k T_A N_t}{L} \qquad (2.17)$$

which by assumption is uniform throughout the flux tube; T_A represents the apex temperature in this equation. This then leads to

$$\frac{\dot{N}_t}{N_t} = \frac{16}{15}2^{1/2}\eta^2\frac{\kappa_0 T_A^{7/2}}{PL^2}. \qquad (2.18)$$

At this point, it is expedient to define the parameter

$$\zeta = \frac{16}{15}2^{1/3}\eta^2 = 0.2913 \qquad (2.19)$$

The apex loop temperature evolution is then described by:

$$\frac{d[ln(T_A)]}{d[ln(t)]} = \left(1 - \frac{3}{2}\frac{\zeta\kappa_o T_A^{7/2}}{QL^2}\right). \qquad (2.20)$$

Depending on the size of Q, the loop temperature can either increase linearly (slower heating) or exponentially approach a maximum apex temperature:

$$T_{A,max} = \left[\frac{2}{3}\frac{L^2 Q}{\zeta \kappa_o}\right]^{2/7} \tag{2.21}$$

where

$$\zeta = 0.2913. \tag{2.22}$$

Finally, the density and pressure for strongly evaporating loops are related by Ω such that

$$\Omega = \left[\frac{1 + \frac{2}{7}\dot{Q}}{Q}\frac{PL^2}{\zeta \kappa_o T_A^{7/2}}\right]^{-1} \tag{2.23}$$

which means that we can theoretically have $\Omega > 1$; however, for situations where the heating rate is very large compared to the net cooling rate $\Omega << 1$.

Strongly Condensing Loops in the Solar Environment

After the flare has cooled for some time, the plasma begins to condense and recombine with the chromosphere. During this phase, the heating term is negligible compared with the cooling term, and the flux is minimal, so that the energy equation becomes:

$$\frac{3}{2}\dot{P} + R + \frac{5}{2}P\frac{dv}{dz} = 0 \tag{2.24}$$

or, inserting the known form of the cooling term,

$$\frac{3}{2}\dot{P} + n^2 A T^\alpha + \frac{5}{2} P \frac{dv}{dz} = 0 \tag{2.25}$$

but since

$$\frac{5}{2} P \frac{dv}{dz} = -\frac{5}{2} P \frac{\dot{N}_t}{N_t} - \frac{5}{2} P \dot{N}_t \Big(1 - \frac{N}{N_t}\Big) \tag{2.26}$$

and

$$\frac{\partial T}{\partial z} = n \frac{\partial T}{\partial N} \tag{2.27}$$

the energy equation can be written as:

$$\frac{3}{2}\dot{P} + n^2 A T^\alpha - \frac{5}{2} P n \dot{N}_t \Big(1 - \frac{N}{N_t}\Big) \frac{dT}{dN} = 0. \tag{2.28}$$

After some algebra, this becomes:

$$\frac{dT}{dN} = \frac{2}{5} \Big[\dot{N}_t \Big(1 - \frac{N}{N_t}\Big)\Big]^{-1} \Big(\frac{2kT}{P^2}\Big) \Big[\frac{3}{2}\dot{P} + n^2 A T^\alpha - \frac{5}{2} \frac{\dot{N}_t}{N_t} P\Big]. \tag{2.29}$$

At the apex, there is no temperature gradient

$$\left.\frac{dT}{dN}\right|_{T_A} = 0 \tag{2.30}$$

and we can define

$$R_A = \Big(\frac{P}{2k}\Big)^2 A T_A^{\alpha-2} \tag{2.31}$$

so that the average cooling rate is

$$< R >= -\frac{3}{2}\dot{P} + R_A. \tag{2.32}$$

Recalling that the plasma is described by

$$\frac{\dot{N}}{N} = \Omega\frac{\dot{P}}{P}. \tag{2.33}$$

we can write:

$$\frac{5}{2}\Omega\dot{P} + < R >= R_A \tag{2.34}$$

which reduces to

$$\Omega = \frac{3}{5}\Big(1 - \frac{R_A}{< R >}\Big). \tag{2.35}$$

While the upper limit for Ω is 3/5, typical values are much smaller since most of the cooling processes take place near the foot points.

Static Loops in the Solar Environment

In midlife, the flux tube is approximately static, meaning that the heating term balances the Spitzer heating and cooling terms, and the enthalpy flux vanishes. The energy conservation equation then becomes:

$$Q_{eff} - R - \frac{dF_c}{dz} = 0. \tag{2.36}$$

In the case of the strongly condensing loop, FH90 found that

$$\frac{x_d^{(\lambda-1/\Omega)}}{(1/\Omega-\lambda)} = \frac{2}{3}\frac{\Omega\hat{K}N_{max}^{\lambda}\tau_D}{P_{max}L^2} \tag{2.37}$$

while in the case of the strongly evaporating loop, we found that:

$$P_{max} = \frac{2^{2/3}\eta 2kT_A N_{max}}{L} \tag{2.38}$$

where

$$N_{max} = \frac{\zeta\kappa_0 T_A^{5/2}\tau_R}{2^{2/3}\eta 2kL}. \tag{2.39}$$

Equating the two expressions for P_{max} gives the scaling law for a magnetic flux tube in the solar environment:

$$LPT_z^{\frac{\alpha}{2}-\frac{11}{4}} = \beta_1\frac{\left[\frac{2k^2\kappa_0(\alpha+\frac{3}{2})}{A}\right]}{2-\alpha} = C \tag{2.40}$$

where C is a constant and

$$\beta_1 = B\left[\frac{11/4-\alpha/2}{2-\alpha},\frac{1}{2}\right] \tag{2.41}$$

where B(a,b) is the beta function and

$$\beta_2 = B\left[\frac{7/4-\alpha/2}{2-\alpha},\frac{1}{2}\right]. \tag{2.42}$$

For solar temperatures (i.e. near 10^5K), this reproduces the scaling law of FH90:

$$L = 0.0126\tau_R^{4/7}\tau_D^{3/7}T_A^{1/2} \tag{2.43}$$

known to be consistent with loop lengths of 10^9 cm produced in the solar environment.

Scaling Law for Flares on an AGN Accretion Disk

The model of magnetic flux tubes as a source of flares can be modified for the AGN environment to produce a scaling law similar to that found for solar and stellar flares. The term affected by the temperature change is the cooling term; thermal bremsstrahlung is the dominant cooling mechanism for plasmas in the temperature regime of solar flares, and follows a well-studied cooling law for solar abundance plasmas (Raymond, Cox, and Smith, 1976). In contrast, the temperatures expected in an AGN corona are higher, and a loop would cool by thermal bremsstrahlung, inverse Compton scattering, synchrotron radiation and, at temperatures above $10^{9.6}$ K, pair creation and annihilation processes. The following calculations result in a scaling law for magnetic flux tubes on an AGN accretion disk.

Cooling Mechanisms

From spectral analysis of Seyfert 1 and other active galaxies the main radiation processes of AGN are known to be synchrotron radiation, inverse Compton scattering, thermal bremsstrahlung, and, if the coronal temperatures are sufficiently high, pair production and annihilation (Blandford, 1990). Since the most accepted AGN model

Log Temperature (K)	log A	α
4.9-5.4	-21.2	0
5.4-5.75	-10.4	-2
5.75-6.3	-21.94	0
6.3-7.2	-17.73	-2/3

Table 2.1: Coefficients for cooling by thermal bremsstrahlung below $10^{7.2}$K

is of a cold (10^5 K) accretion disk surrounded by a hot (10^8 K) corona (Osterbrock, 1993) we begin by reviewing the density and temperature dependence of each of the significant cooling mechanisms.

Cooling by thermal bremsstrahlung is described by:

$$R_{tb} = An_e n_i T^{\alpha} \tag{2.44}$$

where A and α are coefficients determined by Rosner, Tucker, and Vaiana (1978) to the best-fit polynomial fit for the Raymond cooling curve in the pertinent temperature range (Raymond and Smith 1977). These coefficients are reproduced in Table 2.1 for temperatures from $10^{4.9}$K to $10^{7.2}$K.

Above $10^{7.2}K$, line emission is no longer present and thermal bremsstrahlung is described by the expression:

$$R_{tb} = \sqrt{\frac{2\pi kT}{3m}} \frac{2^5 \pi e^6}{3hmc^3} Z_{eff}^2 n_e n_i \bar{g}_b \tag{2.45}$$

where k is the Boltzmann constant, T is the temperature of the plasma in the flux tube, m is the electron mass, h is plank's constant, n_e and n_i are the electron and ion densities respectively, and g_b is the gaunt factor, which we assume to have a value of

1.2. Z_{eff} is the effective charge for the combined species in the plasma; it is typically assumed to have a value of 1.4 in an AGN central engine (Blandford, 1990). If the gas in the flare loop is $10^8 K$, which means that thermal bremsstrahlung will have an energy loss rate of about 6x10^{-6}erg $s^{-1}cm^{-3}$ for a plasma with density 10^9 g cm^{-3}.

The energy loss rate due to Compton upscattering is given by (Rybicki and Lightman, 1979):

$$R_{ic} = \frac{4k_B T}{mc^2} c\sigma_T n_e U_{ph} \tag{2.46}$$

where T is the temperature of the coronal plasma in Kelvin, n_e is the electron density in the plasma, U_{ph} is the incident photon energy density, and σ_T is the Thomson cross section. The photon energy density from the disk is caused by blackbody radiation, so for a disk temperature of 10^5 K, we expect an energy density of:

$$U_{ph} = \frac{4\sigma}{c} T_{disk}^4 = 7.6\text{x}10^5 ergcm^{-3}s^{-1}. \tag{2.47}$$

Our expected cooling due to Compton upscattering will then be 1.4x10^{-6} erg $s^{-1}cm^{-3}$. Thus, for the temperature range of interest we expect that losses due to thermal bremsstrahlung and Compton upscattering will be comparable, and both must be included in any calculations available to estimate the energy balance of the flare loop.

The electrons also emit synchrotron radiation. The ratio of energy loss rates of synchrotron radiation to inverse Compton scattering is given by (Zombek, 1992):

$$\frac{R_{sync}}{R_{ic}} = \frac{U_B}{U_{ph}} \tag{2.48}$$

where

$$U_B = \frac{B^2}{8\pi}. \tag{2.49}$$

In the inner accretion disk of an AGN, magnetic field strengths are typically near 10^3 G (Blandford, 1990), so that

$$\frac{R_{sync}}{R_{ic}} \approx 0.05. \tag{2.50}$$

We can write the combined contribution of synchrotron and inverse Compton losses as:

$$R_{ssc} = R_{ic} + R_{sync} = \frac{4k_BT}{mc^2} c\sigma_T n_e (U_{ph} + U_B). \tag{2.51}$$

In addition to the above, Tritz (1990) showed that nonthermal pair production and annihilation are significant to the energetic balance in AGN coronae. The many pair production mechanisms are dominated by two-photon processes due to their high cross sections and the relatively low densities of particles in the AGN disk (Begelman, Sikora, and Rees, 1987). These processes are important when the parameter

$$\Theta = \frac{kT_e}{m_e c^2} > 1 \tag{2.52}$$

or $T_e > 6\text{x}10^9$K; that is, for half a decade of the temperature range considered here. AGN in general are expected to have significant pair production when

$$l = \frac{L_{obs}\sigma_T}{4\pi(\Delta t_{obs}) m_e c^4} > 1; \tag{2.53}$$

most fall within the range $l = 10^{-3} - 10^1$ (Lightman and Zdziarski, 1987). We will later show that this condition is not satisfied for NGC 3227; therefore, we develop a scaling law which excludes the contributions of pair production for use with this source.

Static Loops on an AGN Accretion Disk

Following the method of Fisher and Hawley FH90, we approximate the loop evolution as a succession of static loops. In order to follow their method, we assume that the plasma in the loop itself is optically thin; the measured optical depth of the corona is $\tau \approx 1$. However, this is the depth of the full corona, not the loop itself. The plasma in the loop itself has windows of relatively low opacity for much of the spectral windows in the ASCA observation, which widen for temperatures above 10^6 K(Burbidge *et. al.*, 1978; Acton 1978; Saba *et. al.*, 1999, McKenzie, 2000). We further assume the loop is in hydrostatic equilibrium (i.e. has constant pressure); this is not justified ab initio, but is taken care of by considering only parts of the resulting parameter space which have loop lengths short enough to be traversed in the timescale of the flare, given the speed of sound of the material. We begin with the energy conservation equation for the plasma:

$$\frac{3}{2}\dot{P} = Q - R - \frac{5}{2}P\frac{dv}{dz} - \frac{dF_c}{dz} \tag{2.54}$$

where Q is the volumetric heating rate for the loop, R is the radiative loss rate given by:

$$R = R_{tb} + R_{ssc}. \tag{2.55}$$

Since enthalpy flux vanishes, the heating law can be written as:

$$R_{tb} + R_{ssc} + \frac{dF_c}{dz} = Q \tag{2.56}$$

The energy conservation equation for the loop then becomes:

$$R_{ssc} + R_{tb} + \frac{dF_c}{dz} = Q \tag{2.57}$$

or, since the local conductivity is given by:

$$F_c = -\kappa_0 T^{5/2}\frac{dT}{dz} \tag{2.58}$$

the loop energy balance becomes:

$$\frac{A}{k^2}P^2T^{\alpha-2} + \frac{4\sigma_T(U_{ph}+U_B)}{mc}P - \kappa_0\frac{\partial}{\partial z}(T^{5/2}\frac{dT}{dz}) = Q. \tag{2.59}$$

It is expedient to define:

$$F = \frac{AP^2}{\kappa_0 k^2}, E = \frac{Q}{\kappa_0}, G = \frac{4\sigma_T(U_{ph}+U_B)}{mc\kappa_0}P \tag{2.60}$$

so that

$$E = G + FT^{\alpha-2} - \frac{\partial}{\partial z}(T^{5/2}\partial_z T) \tag{2.61}$$

Notice that

$$T^{5/2}\partial_z T = \frac{2}{7}\partial_z T^{7/2} \tag{2.62}$$

so that, just as in the calculations for lower temperatures,

$$FT^{\alpha+1/2}\partial_z T - \frac{1}{2}\partial_z[(T^{5/2}\partial_z T)^2] = (E-G)T^{5/2}\partial_z T. \tag{2.63}$$

This can be rewritten as:

$$\frac{2F}{\alpha+3/2}\partial_z T^{\alpha+3/2} - \partial_z[(T^{5/2}\partial_z T)^2] = \frac{4}{7}(E-G)\partial_z T^{7/2} \tag{2.64}$$

At the loop apex, we have z=L, $T = T_A$, and $\partial_z T = 0$. Integrating the entire equation above over dz, we get:

$$2FT^{\alpha+1/2} = E - G \tag{2.65}$$

In a similar manner, we can integrate the general equation over dz and notice that the integrands must be equal; doing so gives:

$$\frac{2F}{\alpha+3/2}T^{\alpha+3/2} - [T^{5/2}\partial_z T]^2 = \frac{4}{7}T^{7/2}. \tag{2.66}$$

We can then make the substitutions:

$$T = xT_A, \tag{2.67}$$

Log Temperature (K)	α	β_1	β_2	λ
4.9-5.4	0	1.40032	2.17272	2
5.4-5.75	-2	0.946224	2.53544	1.27
5.75-6.3	0	1.40032	2.17272	2
6.3-7.2	-2/3	2.12564	3.014	1.68
7.2-9.6	+1/2	1.1781	2	1.17

Table 2.2: Coefficients for cooling by thermal bremsstrahlung above $10^{4.9}$K

where T_A is the apex temperature, and

$$z = Ly \tag{2.68}$$

where z is the altitude in the loop, so that we get:

$$\frac{2FL^2}{\alpha+3/2}T_A^{\alpha-2}x^{\alpha-7/2} - \frac{4L^2}{7}(E-G)x^{-3/2} = T_A^{7/2}(\frac{\partial x}{\partial y})^2 \tag{2.69}$$

Once we substitute

$$2FT^{\alpha+1/2} = E - G \tag{2.70}$$

we are doing exactly the same derivation as FH90, which yields a column density expression:

$$N = Ln_A\frac{\beta_1}{\beta_2}. \tag{2.71}$$

From numerical integration, the numerical values of each of the beta functions β_i and the parameter $\lambda = 14/(7-2\alpha)$ are tabulated for the temperature range of interest in an AGN environment. The upper limit of T=$10^{9.6}$ K is chosen because above this temperature pair processes become important.

The dynamics of strongly evaporating loops are independent of the cooling mechanism, so the physics is identical to that already examined by FH90 and summarized in Section 2.2.3. We thus proceed to find expressions for Ω and P_{max} for a strongly condensing loop on an AGN accretion disk.

Strongly Condensing Loops on an AGN Accretion Disk

Strongly condensing loops are by definition those for which the heating and conduction terms are negligible compared to the cooling. The strongly condensing loop differs from the treatment of the loop in the solar corona. First of all, The energy flow is described by:

$$\frac{3}{2}\dot{P} + R_{tb} + R_{ssc} + \frac{5}{2}\frac{dv}{dt} = 0 \tag{2.72}$$

so, if we define

$$I = \frac{2\sigma_T}{mc}(U_{ph} + U_B) \tag{2.73}$$

and let

$$BP = HP + IP. \tag{2.74}$$

The cooling law then becomes

$$\frac{3}{2}\dot{P} + n^2 A T^\alpha + BP + \frac{5}{2}\frac{d\dot{v}}{dt} = 0. \tag{2.75}$$

We then assume that the quantity $\dot{n}/\mathrm{n}$ is uniform throughout the loop in keeping without assumption that the system is in hydrodynamic equilibrium. This requires that

$$v(z) = \frac{\dot{N}_t}{N}\left[1 - \frac{N}{N_t}\right] \tag{2.76}$$

and

$$\frac{\partial v}{\partial z} = -\frac{v}{n}\frac{\partial n}{\partial z} - \frac{\dot{N}_t}{N_t} \tag{2.77}$$

so that the scaling law is

$$\frac{3}{2}\dot{P} + n^2 A T^\alpha + BP - \frac{5}{2}P\frac{\dot{N}_t}{N_t} - \frac{5}{2}P\dot{N}_t\left(1 - \frac{N}{N_t}\right)\frac{dT}{dN}. \tag{2.78}$$

Noting that

$$\frac{\partial T}{\partial z} = \frac{\partial T}{\partial N}\frac{\partial N}{\partial z} = n\frac{\partial T}{\partial N} \tag{2.79}$$

the cooling law can be rewritten as

$$\frac{5}{2}n\dot{N}_t P\left(1 - \frac{N}{N_t}\right)\frac{\partial T}{\partial N} = \frac{3}{2}\dot{P} + n^2 A T^\alpha + \left(B - \frac{5}{2}\frac{\dot{N}_t}{N_t}\right)P. \tag{2.80}$$

After some algebra, this yields:

$$\frac{dT}{dN} = \left(\frac{2kT}{P}\right)\frac{\left[\frac{5}{2}\frac{\dot{N}_t}{N_t} - B\right]P - \frac{3}{2}\dot{P} - \left(\frac{P}{2kT}\right)^2 A T^\alpha}{5k\dot{N}_t\left(\frac{1-N}{N_t}\right)}. \tag{2.81}$$

At the loop apex, the temperature is at a maximum, so the gradient vanishes; that is:

$$\left.\frac{dT}{dN}\right|_{T_A} = 0 \tag{2.82}$$

so

$$\left[\frac{5}{2}\frac{\dot{N}_t}{N_t} - B\right]P - \frac{3}{2}\dot{P} = \left(\frac{P}{2k}\right)^2 AT_A^{\alpha-2}. \tag{2.83}$$

Now recall that the rate of thermal bremsstrahlung at the apex is

$$R_{bA} = \left(\frac{P}{2k}\right)^2 AT_A^{\alpha-2} \tag{2.84}$$

so that the average cooling rate is:

$$< R >= -\frac{3}{2}\dot{P} = BP + R_{bA}. \tag{2.85}$$

At this point, it is useful to find an upper limit for Ω such that

$$\frac{\dot{N}_t}{N_t} = \Omega\frac{\dot{P}}{P}. \tag{2.86}$$

We can then rewrite the cooling equation as:

$$\left[\frac{5}{2}\Omega\frac{\dot{P}}{P} - B\right]P - \frac{3}{2}\dot{P} = R_A \tag{2.87}$$

or

$$\frac{5}{2}\Omega\dot{P} = - < R > -BP - R_A \tag{2.88}$$

so that

$$\Omega = \frac{3}{5}\left(1 - \frac{BP + R_A}{< R >}\right). \tag{2.89}$$

While this provides the same upper limit of $\frac{3}{5}$ for Ω in the limit of a strongly condensing plasma, in reality Ω will often be significantly lower because the Inverse Compton scattering rate is independent of the temperature and the ratio $\frac{BP}{<R>}$ will be closer to 1 than 0.

An approximate for Ω in a strongly condensing loop is

$$\Omega = \frac{3}{5}\Big(1 - \frac{R_{tot,A}}{< R >}\Big) \tag{2.90}$$

where $R_{tot,A}$ is the total cooling rate at the apex and, in general, $R_{tot} = R_b + R_{ssc}$. From FH90, note that

$$\frac{dT}{dN} = \Big(\frac{2kT}{P}\Big)\frac{\Big[\Big(\frac{5}{2}\frac{\dot{N}_t}{N_t} - B\Big)P - \frac{3}{2}\dot{P}\Big] - \Big(\frac{P}{2kT}\Big)^2 AT^{\alpha}}{5k\dot{N}_t\Big(1 - \frac{N}{N_t}\Big)} \tag{2.91}$$

and

$$\Big[\frac{5}{2}\frac{\dot{N}_t}{N_t} - B\Big]P - \frac{3}{2}\dot{P} = \Big(\frac{P}{2k}\Big)^2 AT_A^{\alpha-2} \tag{2.92}$$

which we can use to find the temperature dependence on column density (and thus indirectly on position in the loop). Let

$$x = \frac{N}{N_t} \tag{2.93}$$

so that

$$\frac{1}{N_t}\frac{dT}{dx} = \Big(\frac{2kT}{P}\Big)\Bigg[\frac{(\frac{P}{2k})^2[AT_A^{\alpha-2} - AT^{\alpha-2}]}{5k\dot{N}_t(1 - x)}\Bigg] \tag{2.94}$$

or

$$\frac{1}{N_t}\frac{dT}{dx} = \frac{P^2}{\dot{P}}\left(\frac{A}{2k^2}\right)\frac{T_A^{\alpha-2} - T^{\alpha-2}}{5\Omega(1-x)}. \tag{2.95}$$

We thus have an expression which depends only on the thermal bremsstrahlung contribution to the cooling. Physically, this makes sense; inverse Compton and synchrotron cooling depend only on the plasma pressure and not on its temperature, so the spatial temperature distribution in the loop is determined entirely by the thermal bremsstrahlung rate, which is temperature dependent.

At this point the physics reproduces that shown in FH90 for a plasma cooling by thermal bremsstrahlung alone. We thus use the upper limit

$$\Omega \leq \frac{12 - 6\alpha}{35} \tag{2.96}$$

which for a plasma with $T > 10^{7.2}$ K means $\alpha = 0.5$ so that the strict upper limit is

$$\Omega \leq 0.257 \tag{2.97}$$

and values for Ω for the lower temperatures are found in an analogous manner.

Scaling Law for a Loop on an AGN

The functional form of the scaling law for flux tubes on an AGN accretion disk is identical to that of a solar flux tube because the derivation of the scaling law does not depend upon the functional form of the cooling mechanism (Fisher and Hawley, 1990; Hawley *et. al.* 1995). The most prominent change in the scaling law is seen in the parameter Ω for strongly condensing loops, which is constrained to a much smaller value as discussed in Section 2.4.

When the loop is in a strongly evaporating phase, the column density was found to be related to the loop semi-length L and rise time τ_R by

$$N_{max} = \frac{\zeta\kappa_0 T_A^{5/2}\tau_R}{2^{2/3}\eta 2kL} \tag{2.98}$$

and the maximum pressure is

$$P_{max} = \frac{2^{2/3}\eta 2kT_A N_{max}}{L} \tag{2.99}$$

as per the calculations of FH90. The static loop models gave

$$\frac{3}{2}\dot{P} = Q - < R > \tag{2.100}$$

which, when combined with the average loss rate for a static loop and the definition of Ω can be shown to give (Metcalf and Fisher, 1996):

$$\frac{dx}{dt} = -\frac{\frac{2}{3}\Omega\hat{K}N_{max}^{\lambda}}{P_{max}L^2}x^{\lambda+1-\frac{1}{\Omega}} \tag{2.101}$$

where

$$x = \frac{N(t)}{N_{max}}. \tag{2.102}$$

Log Temperature (K)	a	s	p	q
4.9-5.4	95.98	0.75	0.5	0.5
5.4-5.75	9.3x10^7	0.2143	0.7857	
5.75-6.3	0.38	0.75	0.5	0.5
6.3-7.2	2.07x10^{11}	0.417	0.4048	0.5952
7.2-9.6	6.79	1	0.5714	0.4286

Table 2.3: Coefficients for AGN scaling law over five decades of temperature

This expression can be integrated to give:

$$\frac{x^{\frac{1}{\Omega}-\lambda}}{\frac{1}{\Omega}-\lambda} = \frac{-\frac{2}{3}\Omega \hat{K} N_{max}^{\lambda} \tau_D}{P_{max} L^2}. \tag{2.103}$$

Since the pressure should have the same maximal value at the end of the evaporating phase as it does at the beginning of the condensing phase, we can substitute the values for N_{max} and P_{max} found for the evaporating phase into the above expression and solve for the loop semi-length L. This gives scaling law for high-temperature flares in the form:

$$L = \frac{1}{2^{4/3}\eta k}\left[\frac{\frac{2}{3}\hat{K}\Omega\tau_D(\xi\kappa_0 T_A^{5/2}\tau_A)^{\lambda-1}(\frac{1}{\Omega}-\lambda)}{T_A(1-x_d^{(\frac{1}{\Omega}-\lambda)})}\right]^{1/\lambda} \tag{2.104}$$

where k=1.38x10^{-16} cgs is the Boltzmann constant, $\kappa_0 = 10^{-6}$ is the Spitzer heating constant, and all other parameters depend upon the values of A and α from the thermal bremsstrahlung rate at that temperature. In each case, the scaling law can then be expressed as a function of the apex temperature T_A and the flare rise and decay times:

$$L = aT_A^s \tau_R^p \tau_D^q. \tag{2.105}$$

The values of these parameters are as shown in Table 2.3.

Observation of Flares in NGC 3227

NGC 3227 has long been known to exhibit rapid X-ray variability; the first HEAO1 observation showed a 140% increase over 5 hours (Tennant and Muschotzky, 1983). The identification of a broadline region (Salamanca *et. àl.*, 1994) classified the source NGC 3227 as a Seyfert 1.5 galaxy. NGC 3227 weakly interacts with its neighbor, NGC 3226, causing the existence of both central compact and extended H I emission regions (Mundell *et. al.*,1995), as well as extended Hα and O [III] emission regions related to the bar of the SA galaxy (Gonzàlez Delgado and Pérez, 1997). ROSAT PSPC observations indicated that the highly variable source exhibited little spectral variability, but strong evidence for dust in the warm absorber (Komossa and Fink, 1997). The 1993 and 1995 ASCA observations of this source showed varying hardness ratios but no direct spectral changes (George *et. al.*, 1998). The overall flux of the 1993 ASCA observation exhibited two flare-like events. This source was thus chosen as a test case for the application of scaling laws similar to those already derived for solar and stellar flares to flares on the inner accretion disk of an active galactic nucleus (AGN).

The light curve of an archival ASCA observation of NGC 3227, a Seyfert 1.5 galaxy showed two strong events which had the same characteristics as do solar and stellar flares: both had linear increases with timescale τ_R and exponential decays with timescale τ_D. This observation of NGC 3227 was performed using ASCA in 1993. The entire observation was performed in faint mode, which was subsequently converted to bright2 mode for analysis. In screening the data, a cutoff rigidity of 6 GeV/c^2

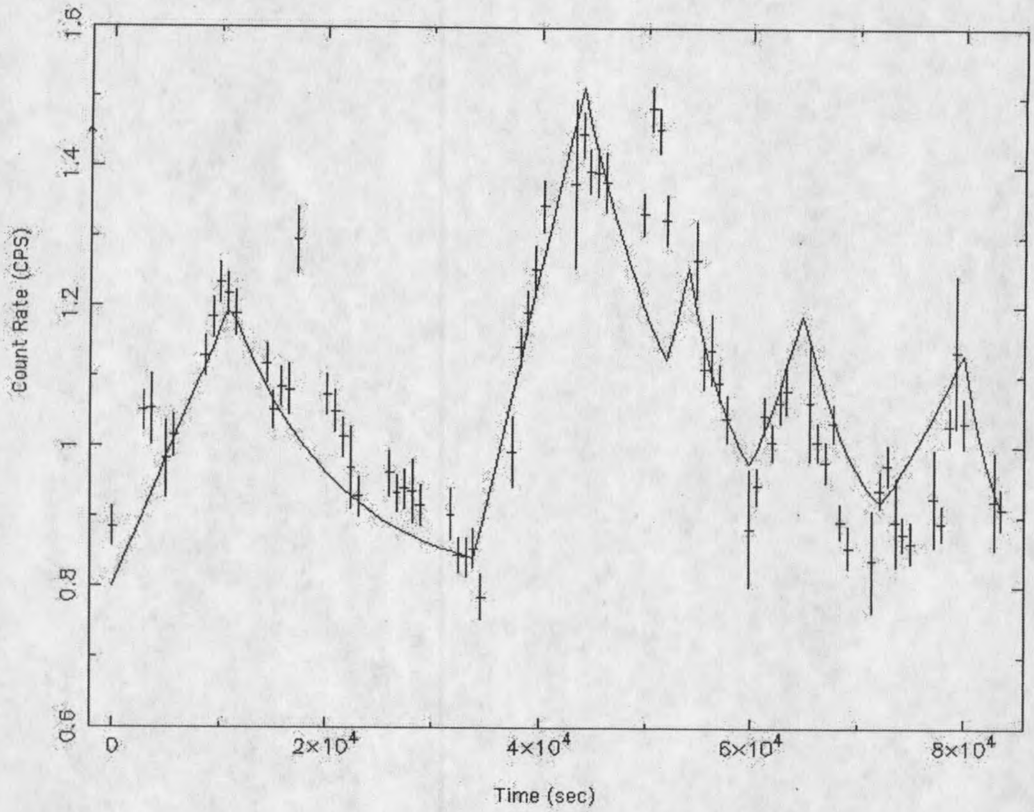

Figure 2.2: Light Curve of NGC 3227

$$I(t) = I_0 + I_1 t; \qquad t_s < t < t_m$$
$$I(t) = I_0 + I_1 t_m e^{-t/t_D}; \qquad t > t_m$$

was used, and data acquired during passage through the south atlantic anomaly were excluded. The following analysis is intended to provide models of the light curve, which is shown in Figure 2.2.

The variability of NGC 3227 was modeled to a constant plus several distinct bursts, modeled by: where t_m is the time at which the maximum of the flare occurred, the rise time $t_R = t_m - t_s$, the burst height $I_1 t_m$ is the maximum amplitude of the burst,

flare	τ_R (s)	τ_D (s)	I_{max} (Counts/s)	t_{max} (s)
1	6,590	12,085	0.701	42,232
2	13,761	7,762	0.400	10,741
3	3,000	1,443	0.200	55,000
4	4,000	3,607		79,000
5	1,122	1,559	0.2161	16,425

Table 2.4: Burst model is fit to the light curve of NGC 3227. Each of the five flares is characterized by a rise time τ_R from the beginning to the maximum of the flare, a decay time τ_D at which the flare has decayed to 25% its original amplitude, a flare amplitude I_{max}, and the time at which the maximum of the flare occurred t_{max}

and the decay time t_D is defined to be the time taken for the burst to decay to one fourth of its maximum value.

Since this source comes from a region of the X-ray sky with average background of roughly 0.1 CPS in the spectral region of interest, no background subtraction has been performed The light curve of NGC 3227 was fit to five flares using the software package XRONOS, indicated by the solid line in Figure 2.2. The parameters of each of the flares are shown in Table 2.4.

The shortest timescale of variation is on the order of 1000 seconds for this source; its average observed luminosity in the 0.1–10 keV band is 10^{42}erg/s (George *et. al.*, 1998). This gives l=0.07, verifying that pair processes are not substantial in this source as per the discussion of Section 2.3.1.

We can now find an approximate relation between apex temperature and the expected loop length for the temperature range $T=10^{4.9-9.6}$. Loop lengths for each of the five flares are shown as a function of apex temperature in Figure 2.3. The disjoint nature of the curve results from the approximate treatment of thermal bremsstrahlung discussed earlier; the results near the boundaries between segments of the curve are

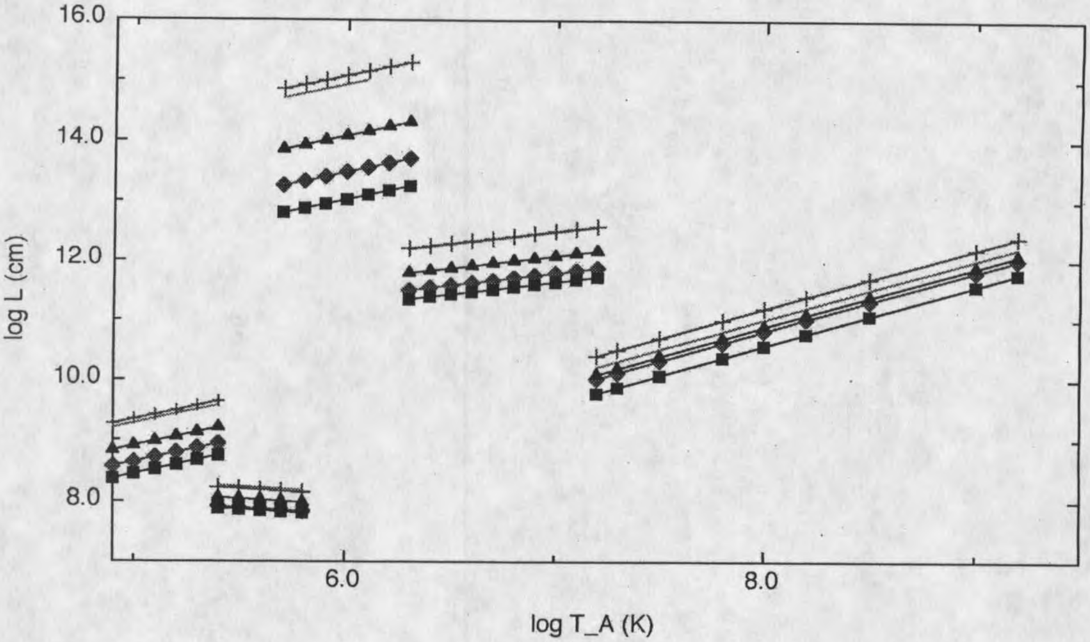

Figure 2.3: Loop length as a function of apex temperature for the five flares in the observation of NGC 3227. The solid line represents flare 1, the crosses flare 2, the diamonds flare 3, the triangles flare 4, and the boxes flare 5.

not robust.

As we have performed the above calculation with the upper limit of the parameter Ω, we might ask what affect a smaller value would have on the projected loop length. The question is particularly important for AGN since the expected contributions of combined inverse Compton and synchrotron processes are comparable to that of thermal bremsstrahlung. We expect the plasma to cool faster than if by thermal bremsstrahlung alone, thus we expect a smaller value of Ω. As an extreme case, consider the limit as Ω approaches 0; the loop length then becomes:

$$L(\Omega = 0) = \frac{1}{2^{4/3}\eta k}\left[\frac{2}{3}\hat{K}(\xi\kappa_0)^{\lambda-1}\right]^{\frac{1}{\lambda}} T_A^s \tau_R^p \tau_D^q \qquad (2.106)$$

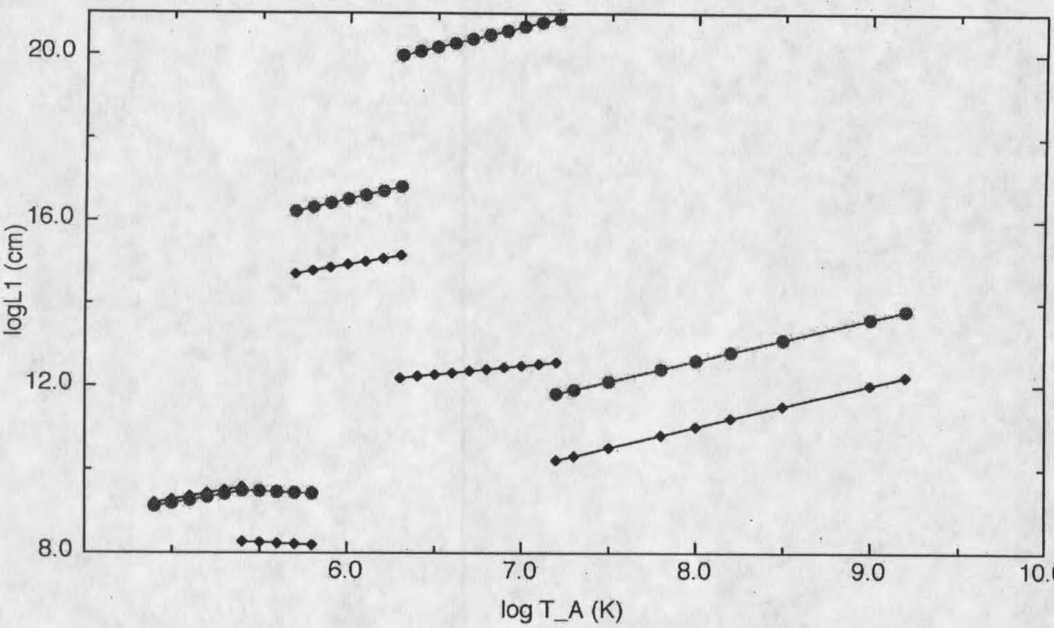

Figure 2.4: Loop length as a function of apex temperature for the first flare in the observation of NGC 3227. Diamonds represent the upper limit on Ω, circles the case Ω=0.

where s,p,q are as defined previously. The projected loop lengths for the first loop will be longer for most temperature regimes, as shown in Figure 2.4.

Physical Constants of AGN Flares

While we can predict a length of the flux tube associated with each temperature window of thermal bremsstrahlung emission, such loop lengths must pass certain criteria to be physically plausible. One assumption of the scaling law is that the plasma within the loop is in hydrostatic equilibrium. In order to accomplish this, the loop must be short enough that sound waves can cross the length of the tube on timescales much shorter than those of the observed flares. Another is that the loop length must be longer than the pressure scale height of the inner accretion disk in order to be meaningfully anchored in the accretion disk. Still another is that the thermal energy in the flare plasma must be at least as great as the energy radiated by the flare.

The speed of sound c_s in an accretion disk is given by:

$$c_s = \frac{\omega h}{\sqrt{3}} \tag{2.107}$$

where h is the half-thickness of the disk and Ω its angular velocity (Shakura and Sunyaev, 1976). For a typical disk, $h \approx 0.1R$, so using a Keplerian orbit around a Schwarzschild black hole,

$$c_s = \frac{0.1}{\sqrt{3}}\sqrt{\frac{GMc^2}{R}} \tag{2.108}$$

or, for the innermost stable orbit of a Schwarzschild black hole at $6R_s$, $c_s = 10^{10}$ cm/s. We thus require

$$L < \tau_R c_s. \tag{2.109}$$

For the longest decay time in Table 2.4 (for which we have also calculated a loop length), this gives

$$L < 10^{13}\mathrm{cm} \tag{2.110}$$

which is achieved by most of the temperature regimes of interest.

The flux tube must also be longer than the pressure scale height of the disk to which it is anchored; in particular, we require

$$L > 0.1R_s = h \tag{2.111}$$

where R_s is the Schwarzschild radius of the black hole (Shakura and Sunyaev, 1973). Recent work by DiMatteo (1998) suggests that a flare height of 0.8 R_s is appropriate for flares on AGN disks. Seyfert 1 galaxies are usually associated with spiral galaxies, and as such are thought to have central black holes of mass near $10^{6-7} M_{sun}$ (Rees, 1996). The associated Schwarzschild radius is then $3\text{x}10^{11-12}$ cm, so our flux tube must have L> 10^{10-11} cm.

In order to produce enough radiated power to explain the 10^{42} erg/s amplitude of the $\approx 10^{3-4}$ s flares, the thermal energy stored in the flare loop must be greater than the energy released during a flare event. The thermal energy stored in a flare is given by:

$$U = 2n_e VkT \tag{2.112}$$

where n_e is the electron density, V is the volume of the flux tube, and T is the temperature (assumed to be the same for electrons and ions). If the loop minor radius is a tenth of its length, this leads to the requirement that:

$$L^3 > 6\text{x}10^{57} n^{-1} T^{-1} \tag{2.113}$$

to produce the 10^{42} erg/s for the largest two flares in NGC 3227. The disk density is thought to be near $10^{16} cm^{-3}$ (Di Matteo, 1998), and the density of the plasma in the flux tube probably considerably lower.

These physical requirements are summarized in Figure 2.5, which shows regions in the L-T_A parameter space for which flux tubes are allowed on an AGN accretion

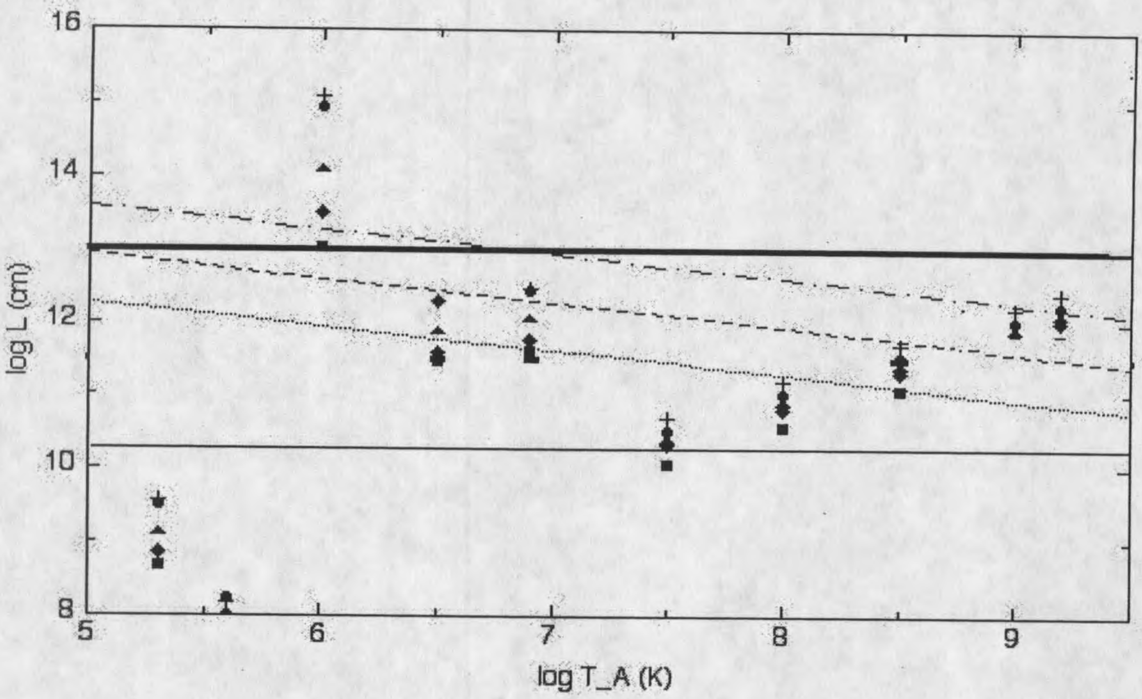

Figure 2.5: Below 10^{10} cm, loops cannot exist because they are smaller than the pressure scale height of the disk, while above 10^{13} a sound wave cannot cross the disk on timescales shorter than those of the flare event. The dotted line indicates the temperature at which the loop can emit 10^{42} erg/s for a density of $10^{16}\mathrm{cm}^{-3}$, the dashed line that for a density of $10^{14}\mathrm{cm}^{-3}$ and the chain dashed line that for $10^{12}\mathrm{cm}^{-3}$. Also shown are projected loop lengths for the five observed flare in NGC 3227; circles represent flare 1, crosses flare 2, diamonds flare 3, triangles flare 4, and boxes flare 5.

disk. The white area indicates the parameter space available after application of the first two constraints; the energy constraint for a plasma with density $10^{12-16}cm^{-3}$ overlaps this area for the loop lengths and temperatures allowed by the other two constraints. Figure 2.5 demonstrated that the calculated loop lengths of the flares observed in the ASCA observation of NGC 3227 are consistent with the constraints on sound speed, pressure scale height, and energy for apex temperature in the range $10^{6.5-7.2}$K or above $10^{8.5}$K. At present, there is no easy way to distinguish in which of these two temperature regimes these flares lie; either range is consistent with expected densities.

Considering again that the calculated loop lengths assume the upper limit of Ω, we note that the loop lengths for the upper temperature regime remain plausible for values of Ω throughout its plausible range, while plasma in the temperature range $10^{6.5-7.2}$K is much more sensitive to the value of Ω. In the presence of strong inverse Compton radiation (or synchrotron radiation, although the second is relatively small, as per Section 2.3.1), the plasma cools faster than if by thermal bremsstrahlung alone. Ω will thus be smaller, in general, than suggested by this treatment, and will mean increased loop lengths for all temperature regimes above $10^{5.4}$K. This would correspond to longer lengths for loops in the $10^{6.3-7.2}$K range, possibly (but not necessarily) above the limit imposed by the sound transit time of the loop. However, faster cooling (and hence longer) loops in the $10^{7.2-9.6}$K range would mean that loops exceeded the pressure scale height of the disk at lower temperatures, making it more likely that loops with plasma above $10^{7.2}$K were responsible for flares such as those observed in NGC 3227.

Conclusion

We find that the loop lengths predicted for a flare event observed in the Seyfert 1 galaxy NGC 3227 are consistent with the expected form of a scaling law for a coronal loop. One length which meets the physical requirements for the energy emitted by the flare, sound transit time of the loop, and pressure scale height of the AGN accretion disk corresponds to apex temperatures in the range $10^{6.5-7.2}$K. This is reasonable not only because it is within an order of magnitude of the coronal temperature predicted by the classic disk-corona model of AGN (10^8K) but also because it suggests a value for T_A which is more than ten times the expected disk temperature of 10^5K, as observed in cooler solar flares. In addition, a $10^{7.2}$K plasma is two orders of magnitude below the regime where pair processes are important components of the energetics, thus justifying our neglect of them in this work. The hotter flares ($T_A > 10^{8.5}$K) are also plausible in terms of expected coronal temperatures, and above 10^9K, an inefficient emission process can be accommodated even for low densities. In addition, flares above $10^{7.2}$K are still viable for values of Ω smaller than the upper limit, making it most likely that this temperature range corresponds to the flare temperature in this source.

Thermal bremsstrahlung is clearly not the dominant emission mechanism for Seyfert galaxies. However, when we consider the dependence of each of the mechanisms on pressure, we find that synchrotron radiation and compton upscattering are both linearly related to the plasma density. This means that, although they are larger than thermal bremsstrahlung, their effect will be to change the effective heating rate of the plasma rather than changing the functional form of the scaling law. This would not be the case for pair processes; other Seyfert galaxies and AGN which are in the regime where pair processes are more important will need a more sophisticated treatment which incorporates the losses due to these mechanisms.

CHAPTER 3

ANALYSIS TECHNIQUES

Two roads diverged in the woods

So I took the path less travelled by

and that has made all the difference.

-Robert Frost (1963)

Introduction

Seyfert 1 galaxies emit light with significant luminosity across the electromagnetic spectrum from infrared to high-energy γ rays. The low-energy region of a Seyfert 1 (Sy1) is dominated by a power law spectrum which is superimposed by a blackbody spectrum in the UV, which is often referred to as the "Big Blue Bump". The powerlaw spectrum from the IR to the UV has the functional form (Ferland 1996):

$$f_\nu = \nu^\alpha exp(-h\nu/kT_{BB})exp(-kT_{IR}/h\nu) + a\nu^\alpha. \quad (3.1)$$

where f_ν is the radiative flux at frequency ν; α is the power law coefficient for the continuum, and is related to the photon index by:

$$\Gamma = \alpha + 1, \tag{3.2}$$

T_{BB} is the temperature of the blackbody emission which causes the big blue bump, T_{IR} the temperature of the blackbody causing emission in the IR, and a is an empirically determined constant relating the relative strength of the powerlaw to the blackbody continua.

The spectrum of the X-ray region is dominated by the powerlaw continuum, but also includes neutral hydrogen absorption, an iron Kα emission line theorized to originate from the accretion disk orbiting the central black hole, and oxygen absorption postulated to originate from the warm absorber. Observation of the X-ray window thus provides clues to the structure and variation of the innermost regions of the galaxy.

This chapter is essentially a methods and materials description for the data analysis portion of this thesis. Section 3.2 describes the design of ASCA and summarizes those technical details which directly affect the analysis described later in this work. Spectral fittings are all performed with the software package XSPEC and other data reduction with the software package XANADU; both were developed by NASA for analysis of X-ray observations. A specific procedure for consistently modelling spectra and minimizing unphysical effects of the fitting algorithm are described. This procedure was developed by the author, and is described in Section 3.3. Readers unfamiliar with the models available in XSPEC, or with the standard statistics used to evaluate their goodness of fit, will find a summary in Appendix A. Section 3.4 describes techniques used in this work for timing analysis of Seyfert 1 Galaxies. Section 3.5 describes techniques to group bins from light curves in which the galaxy is in different dynamical states; in addition to reviewing standard techniques, two new selection methods developed by the author are described.

Optical Design of the X-ray Telescope ASCA

The observations described in this work are data from the Japanese satellite ASCA, which consists of four separate detectors- two SIS (Solid State Imaging Spectrometer) and two GIS (Gas Imaging Spectrometer) detectors. One improvement of ASCA over ROSAT and GINGA is that its spectral window, spanning from 0.5 to 10 keV, covers the soft X-ray region of the warm absorber as well as the harder X-ray powerlaw continuum and Fe Kα emission features. ASCA's energy resolution of $\frac{\Delta E}{E} = 2\%$ for the SIS detectors is also of high scientific importance because it allowed the first resolution of the two oxygen absorption edges just below 1 keV; these edges constitute what is known as the "warm absorber" in AGN. ASCA was the first X-ray telescope with high enough spectral resolution to determine the emission line parameters between 0.5 and 10 keV. In particular, the iron Kα line was found to exhibit a redshifted lobe which was consistent with a disk orbiting a Kerr black hole (Iwasawa *et. al.* 1996).

Each of the four detectors on the satellite ASCA has its own optical assembly; all lie within the same plane at the back of the satellite. The focussing optic for each detector consists of a mirror made of 120 nested concentric aluminum foils coated with 10–20 nm of acrylic and 60 nm gold, which enhances the reflectivity. The light reflects off each at grazing incidence. The focal length of the mirror is 3.5 m. ASCA has four imaging spectroscopic detectors; two are the GIS (Gas Imaging Spectrometer) detectors with a circular, 50" field of view, and provide adequate operating characteristics for an energy range from 0.7–10 keV. Their energy resolution is 8% at 5.9 keV, and their effective area is 1300 cm^2 at 1 keV and 600 cm^2 at 7 keV. ASCA's other two detectors are solid state imaging spectrometers (SIS), each consisting of 4 charge coupled devices (CCD); ASCA was the first X-ray satellite to use CCD's as a photon detector. The SIS detectors have the same effective area as do the GIS detectors, but their field of view is 22"x22" square (if all 4 CCD's are used; observations taken in 1- or 2-CCD mode, such as those described here, have a smaller field of view). They have better response in the soft X-ray region, and provide acceptable response over the 0.4–10 keV energy range; the energy resolution at 5.9 keV is 2%.

While both sets of detectors were slowly undergoing radiation damage the two SIS detectors were particularly susceptible to damage, and became unusable in more recent observations. High energy particles from cosmic rays and the solar wind cause color center formation and other forms of lattice damage in the CCD's; this increases the number of hot and flickering pixels and increases the dark current[1] (Dotani *et. al.*

[1]Single photon detectors typically require that the incident photon liberate electrons from the detector material, causing current to flow. No such detector is perfect- occasionally an electron will be emitted, causing a current, when no photon is incident. This is referred to as "Dark Current" or "Non X-ray Background", and is a standard specification given with any photon counting device.

1997).This has several effects on observation with ASCA; first, the increased number of hot and flickering pixels makes it nearly impossible to perform 4-CCD observations with the SIS detectors as was sometimes done early in ASCA's lifetime. Secondly, the detector response function changes over time, so the available calibration files become less reliable. In addition, the validity of the background files created by NASA during the performance verification (PV) phase just after ASCA's launch is lessened due to the changes in dark current and detector response function. This suggests that a nearsky background is particularly appropriate for SIS data. In more recent observations, the SIS detectors are only considered valid above 0.7 keV.

Techniques of Spectral Analysis

A typical ASCA Seyfert 1 spectrum is shown in Figure 3.1. The spectrum consists of a number of features; first, the electrons from the corona produce a powerlaw continuum with $\Gamma \approx 2$. This can be seen most clearly between 2 and 10 keV. Below 2 keV, the powerlaw continuum is absorbed by the interstellar medium (ISM)[2], causing an obvious deficit in the count rate expected from the source. One other continuum feature can be seen in some sources; above 9 keV, a small X-ray excess is visible. This is the low energy end of the "reflection hump" first discovered by GINGA observations, and thought to be caused by Compton reflection of the continuum.

A number of absorption and emission features are also present in Figure 3.1; all are redshifted due to the recession of the galaxy. An iron absorption feature can be

[2]The Interstellar Medium consists of rarified gas within our Galaxy, the host galaxy, and (to a much smaller extend) intergalactic space; the equivalent column depends on the angular location of the extragalactic source.

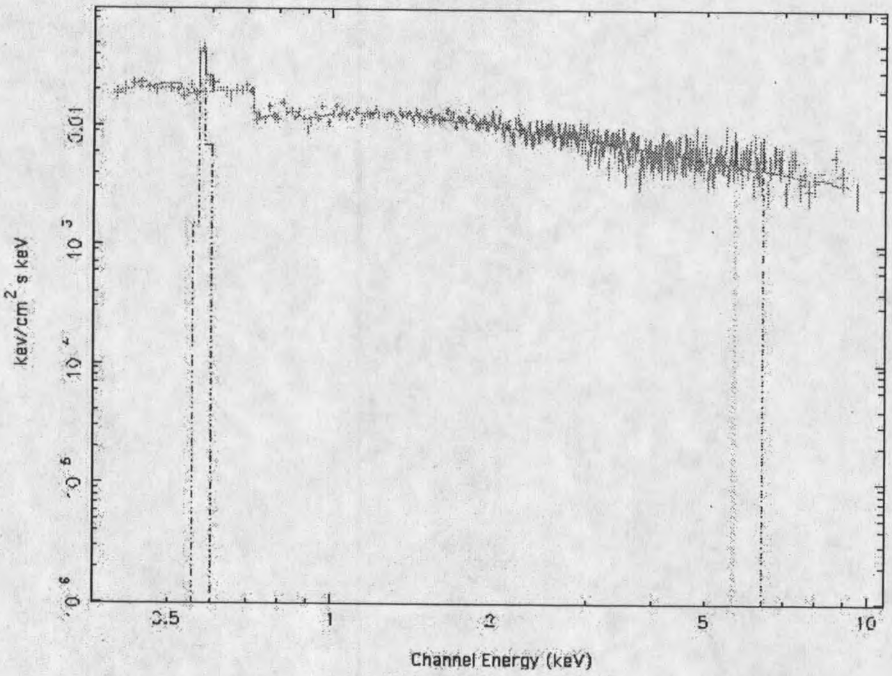

Figure 3.1: Typical X-ray spectrum of an AGN.

seen above 7 keV; if the iron is neutral, this feature occurs at 7.1 keV, if ionized the absorption feature is between 7.6 and 7.9 keV. At slightly lower energies near 6.4 keV, we see a line profile due to iron Kα emission. The next prominent continuum features occur at the softer end of the spectrum, in the same region as broadband absorption by the ISM; two ionized oxygen edges occur below 1 keV. One of these is due to O VIII near 0.871 keV, and another is due to O VII near 0.721 keV. Below 0.6 keV the effective area of ASCA decreases sharply, making spectral features difficult to detect and analyze. The narrow emission line near 0.58 keV is a feature of damage to the SIS detectors, and has no physical significance.

Background Subtraction

In addition to dark current and other sources of X-rays from within the detector, the night sky itself has an X-ray background. The X-ray background originates from several sources; about half the counts from 0.5–10 keV are emissions from unresolved quasars (Fabian and Barcons, 1992). The X-ray background of the night sky is not spatially uniform (Schafer, 1993); and is shown in Figure 3.2, which, with the five sources analyzed or shown as examples within this work are labelled. NGC 5548 and MCG-6-30-15 (C and D respectively on the image) are located in areas of the sky with high X-ray background, while the NGC 3227, Arkarian 120, and NGC 4593 are located in areas with average or low background counts. The location of the source in the X-ray sky determines the optimal method of background subtraction for the SIS detectors; sources from regions of the sky with low X-ray background

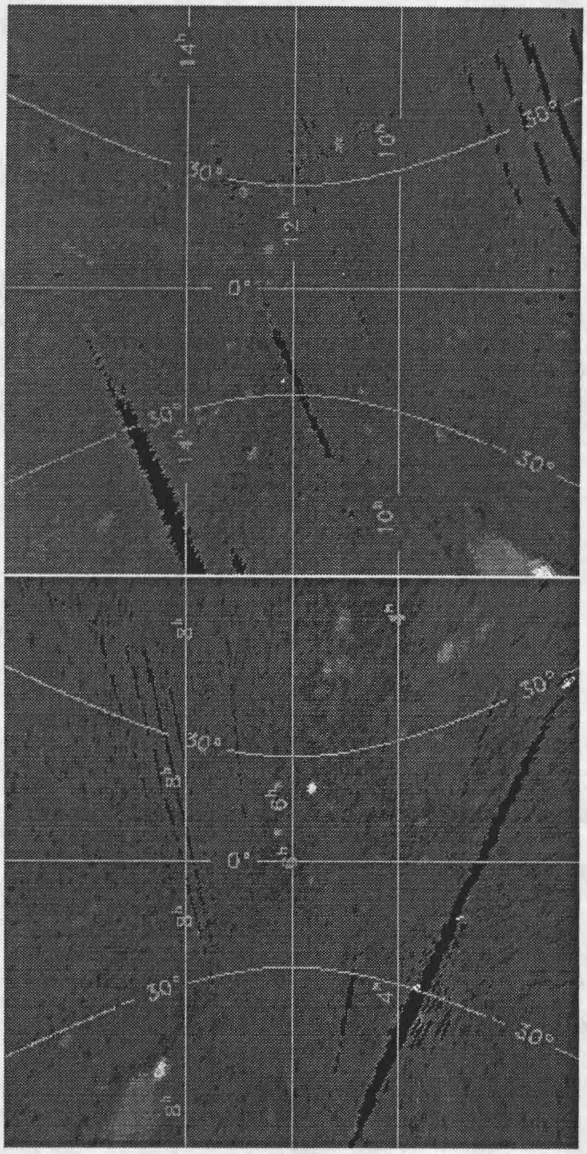

Figure 3.2: Partial images of the X-ray sky at 1.5 keV; dark blue areas indicate low count rates, while yellow areas indicate very high count rates. Images are gnomic plots covering 180 degrees on each axis of the sky from the RASS 1.5 keV survey (Snowden *et. al*, 1995.) The sources labelled here are: A)NGC 4593 B) NGC 3227 C) NGC 5548 D) MCG-6-30-15, and E) Akn 120.

Source	Source CR	Nearsky CR	Blanksky I CR	Blanksky II CR
Arkarian 120	1.301	0.025	0.018	0.008
MCG-6-30-15	1.47	0.023	0.009	0.003

Table 3.1: SIS0 X-ray count rates for the sources considered in this work; each count rate is in units of counts/keV/cm^2/s, and represents an average rate for the entire observation. The Source CR is the average count rate for the source itself, the nearsky count rate is that of a non-source region on the SIS0 chip, the Blanksky I CR is the count rate of the blanksky observation from a region identical to that of the source, and the Blanksky II CR is the count rate of the blanksky observation from a region identical to that of the nearsky.

should use a blanksky background subtraction, while sources from areas of high X-ray background should use a nearsky region for SIS background subtraction. The background count rates for each of the sources in this work are shown in Table 3.1, and were measured by the author. These sources indicate the variation in the X-ray background; Arkarian 120 originates from a low background region of the sky, and the blanksky background is used for the SIS subtraction, while MCG-6-30-15 originates from a high background region of the sky, so a nearsky subtraction is used for the SIS background. In contrast, the GIS detectors experience substantial vignetting, which precludes the use of nearsky regions for background subtraction. Within this work, we thus use the average X-ray background obtained for 15 different blanksky pointing positions. (Ikebe *et. al.*, 1995). In each case the blanksky background region filter was identical to the source region.

Procedure for Empirical Models

Since Seyfert 1 galaxies have relatively complicated spectra in the ASCA window, XSPEC's fitting algorithms will frequently have model parameters which interact with one another to produce values which are unphysical. The author therefore determined which model parameters affect one another and developed a sequence for fitting spectral data which minimizes the affects of these conflicts.

Continuum models for ASCA observations are fit to the harder X-rays due to the interference from Galactic hydrogen absorption at lower energies. The models are in each case fit to a 2-10 keV window with the iron line region for the source excluded. The lower energy cutoff of 2 keV is not arbitrary, it was determined by examining a graph of the best-fit photon index as a function of energy. The solid circles in Figure 3.3 shows how a simple powerlaw model, described in the next section, varies when fit simultaneously with neutral hydrogen; above 3 keV the line remains almost constant as a function of energy. Within the 3–10 keV region we expect to find an iron absorption edge near 7.1 keV and an iron Kα emission line near 6.4 keV. Thus, the continuum spectra is determined by excluding a region of approximately 5-7.5 keV in which these features exist for the purpose of fitting the powerlaw continuum. The exact limits of the excluded region are determined from a double-gaussian fit to the iron Kα line simultaneously with the continuum each case; the limits of the excluded region for each source are determined by the energy at which the iron line is less than 10% of its maximum.

The photon index is fit to the 2–10 keV GIS data, excluding the iron emission region. The soft energies are excluded from this fit because the Galactic hydrogen absorption which manifests itself below 3 keV has the strong potential to increase both itself and the photon index simultaneously, as shown by the simultaneous contour plot

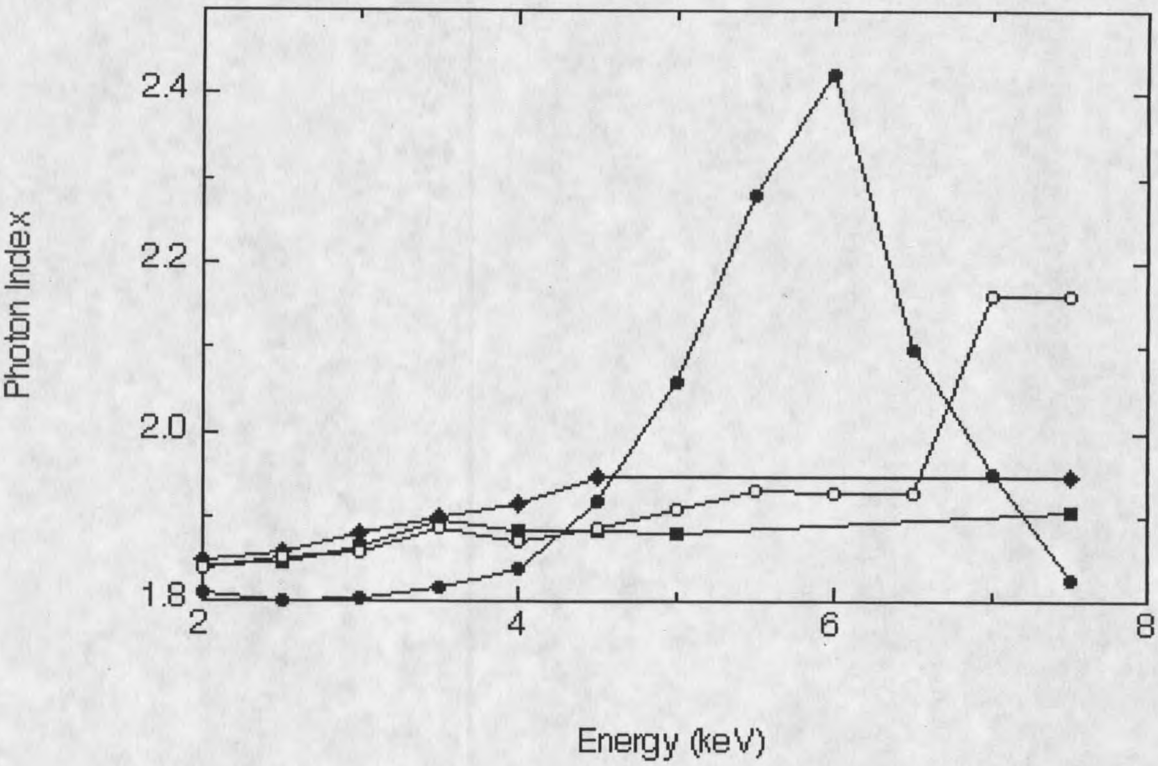

Figure 3.3: Photon index when fit to a spectral window from n keV to 10 keV where n is the energy indicated by the horizontal axis. Filled circles represent a simple powerlaw fit, diamonds are a simple powerlaw with the iron line region ignored, squares are a powerlaw with a double-gaussian fit of the iron line, and the open circles are a powerlaw with a Schwarzschild diskline model. This set of measurements was made using an archival ASCA observation of MCG-6-30-15.

Method	Γ	χ^2/dof
A	1.80 ± 0.03	1.090
B	$1.87^{+0.05}_{-0.04}$	0.8819
C	1.89 ± 0.05	0.9457
D	1.84 ± 0.04	0.9382

Table 3.2: Four methods of fitting the photon index are shown; a) a powerlaw spectrum with no modification for iron absorption or emission features, b) a powerlaw spectrum with the 5–7.5 keV region excluded, c) a model with a powerlaw continuum, double-gaussian fit for the iron line, and edge model for the iron absorption edge, and d)a model with a powerlaw continuum, Schwarzschild profile fit to the iron emission line, and edge model for the iron absorption edge.

of the two parameters in Figure 3.4.

The validity of this approach was tested for the full observation spectrum of the 1993 observation of MCG-6-30-15. First, the powerlaw was fit to the entire spectrum, including the iron line, for an energy interval from 2-10 keV, 2.5-10 keV . . . 7.5-10 keV. Then the 5-7.5 keV region was excluded, and the powerlaw fit to spectral windows from 2-10 keV up to 4.5-5 keV. Then two models of the Fe Kα emission line were fit simultaneously and the powerlaw compared across various spectral windows. The results of these four fits are shown in Table 3.2; all have been fit for a spectral region of 3-10 keV.

The powerlaw fit to the complete spectrum with no treatment of the iron line gives a lower photon index than any of the other methods. Thus, fitting the powerlaw from 3 keV to 10 keV with the iron line excluded is a valid means of measuring the photon index provided the iron line does not have a red wing extending below 5 keV. Since the fitting algorithm takes significantly less computation time, we adopt the approach of fitting the powerlaw continuum to a continuum model and excluding the iron line

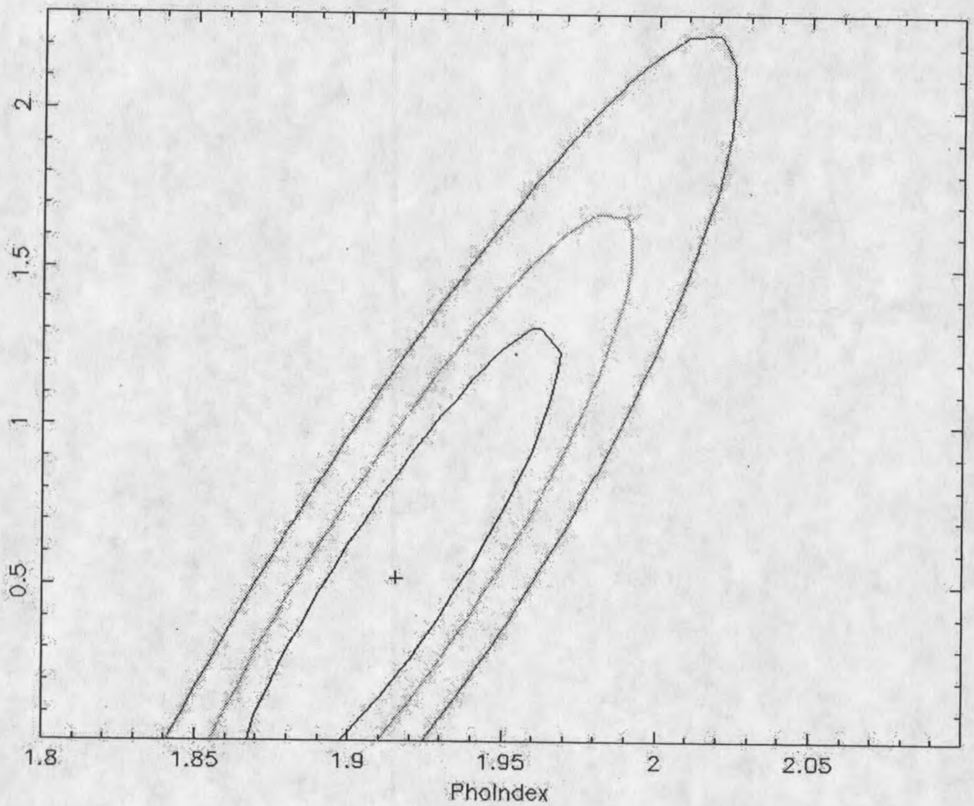

Figure 3.4: Confidence contours for the photon index and neutral hydrogen column. The fact that the contours are a tilted ellipse indicates that the parameters have a tendency to increase each other when fit simultaneously. This contour plot was made using an archival observation of MCG-6-30-15; the interdependence of these parameters is characteristic of the models used and ASCA data, and is the same for all sources described within this work.

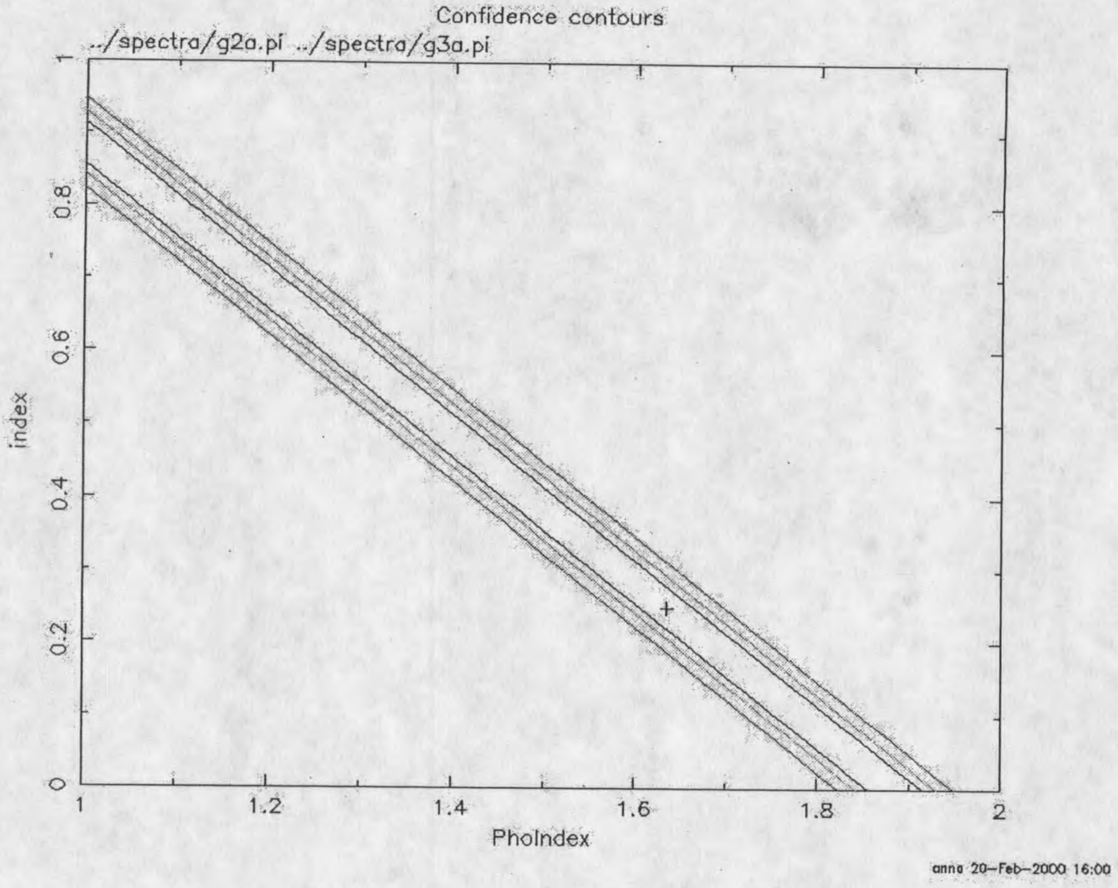

Figure 3.5: This measurement was taken from the archival ASCA observation of Arkarian 120.

for all subsequent analyses.

The two partial absorption models (by gas and by dust) are relatively straightforward. In the case of partial absorption by dust, the absorption term multiplies the photon index and is:

$$M(E) = Ae^{-\alpha} \tag{3.3}$$

Since A is redundant with the powerlaw normalization n, it is frozen to 1 for fitting; α interacts with the photon index Γ, as shown in Figure 3.5. parameters when fit

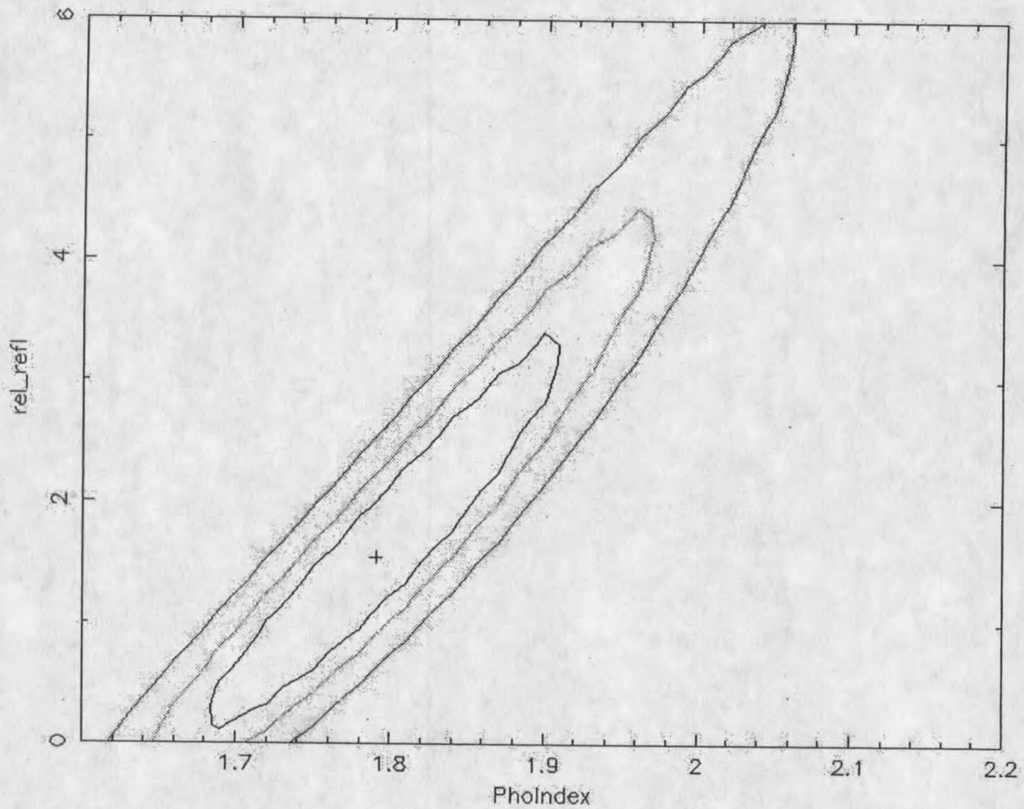

Figure 3.6: Confidence contours for photon index and relative reflection This measurements was taken from segment 3 of the newest ASCA observation of NGC 5548.

simultaneously, as a larger dust index α is naturally fit to a smaller photon index. For older ASCA observations, the difference can be rectified by noting whether the lowest energy bins (below 0.6 keV) are consistent with the powerlaw, as the correct photon index will coincide with both these bins and those above 2 keV without other fit parameters interfering.

Figures 3.6 and 3.7 show that the relative reflection and the photon index interact with one another; when one increases, XSPEC's fitting algorithms will cause the other to increase, so that high values of either parameter should be interpreted very

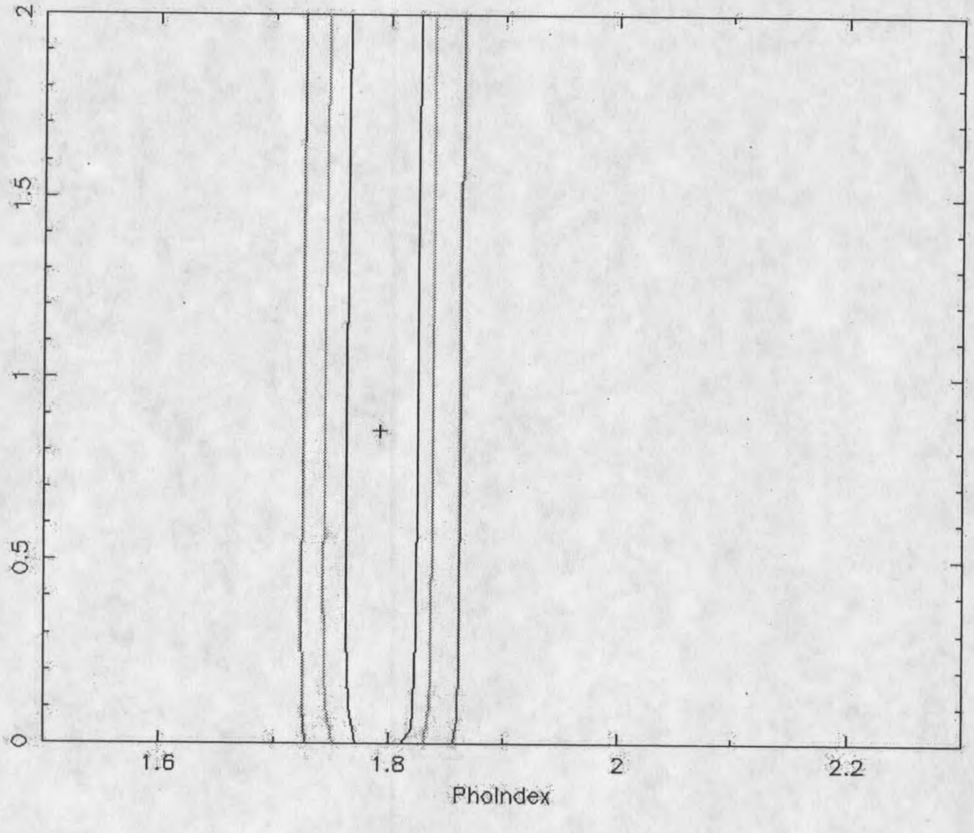

Figure 3.7: Confidence contours for photon index and ionization parameter. This measurements was taken from segment 3 of the newest ASCA observation of NGC 5548.

cautiously. In contrast, there appears to be minimal correlation between the photon index and the ionization parameter, so the two may be fit concurrently without precautions. Since there is no independent means of interpreting the relative reflection with ASCA data, the procedure used was to fit it to a small value and allow the other parameters to fit. A second fitting was then done with the photon index frozen to determine a plausible value for the relative reflection. Since the only difference between the pexriv and pexrav models is the inclusion of the ionization parameter, which does not interact with the photon index, the same procedure is used to fit both the ionized and neutral reflection models.

The neutral hydrogen of an AGN must fall within two constraints; first, it must be no smaller than the Galactic hydrogen measured by the 21 cm radio measure and second, it must be no larger than any existing measurement of neutral hydrogen made by ROSAT. The 21 cm radio line includes only neutral hydrogen in our own Galaxy; as neutral hydrogen can potentially exist in the host galaxy and, in small quantities, in intergalactic space, the measurement of the extinction in X-rays can potentially be larger. ROSAT has much lower energy resolution than does ASCA, and so cannot resolve the two oxygen edges described below. As the oxygen edges are absorptive features, their presence reduces the total number of counts, which would cause low-resolution data to fit a larger neutral hydrogen column than is actually present.

The oxygen edges are extremely sensitive to the column density of the ISM; as such, the neutral hydrogen density must be determined and frozen before the oxygen

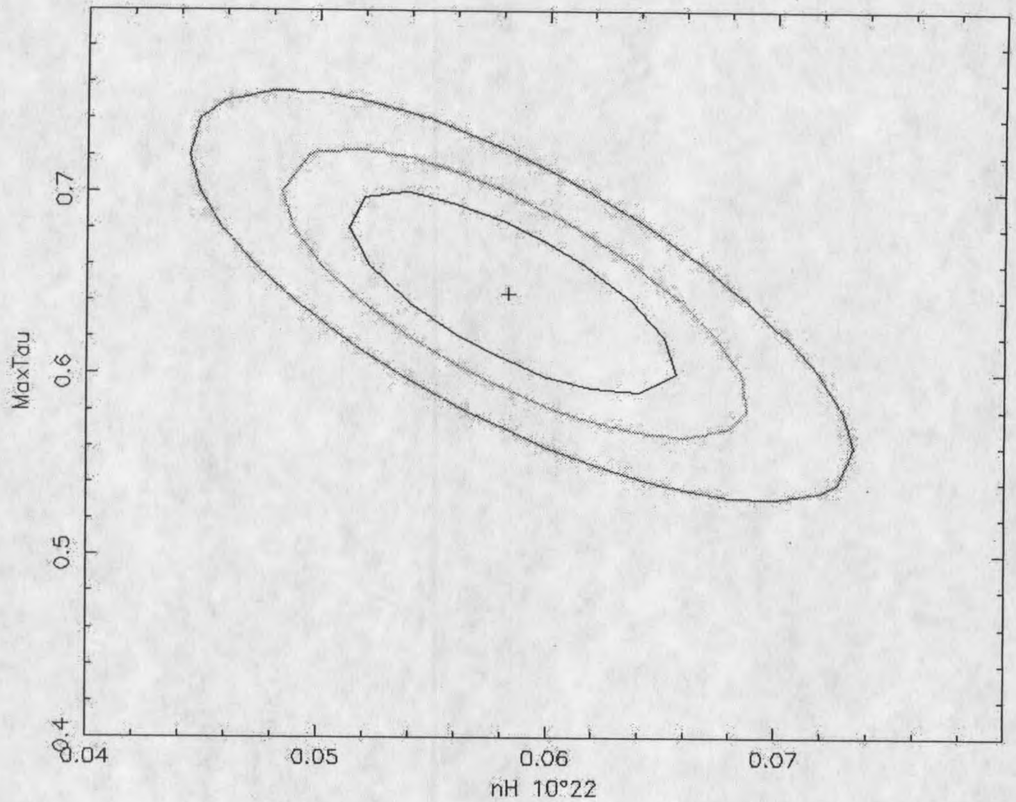

Figure 3.8: Contour plot of optical depth of O VII shows ellipses with a major axis tilted from the horizontal. This indicates that increasing the neutral hydrogen will decrease the O VII edge depth if all other parameters remain constant. This particular set of contours was made for MCG-6-30-15 but the interdependence of the parameters is present in all models.

edges are fit. The interdependence of these parameters is shown in Figures 3.8 and 3.9, in which we can see that increasing the neutral hydrogen column substantially decreases the edge depth of both O VII and O VIII.

The 21 cm line measurements of the neutral hydrogen in each case are given in Table 3.3. The two oxygen edge depths also affect one another, particularly when the edge energies are not well fit, as illustrated in Figure 3.10. XSPEC's fitting algorithm

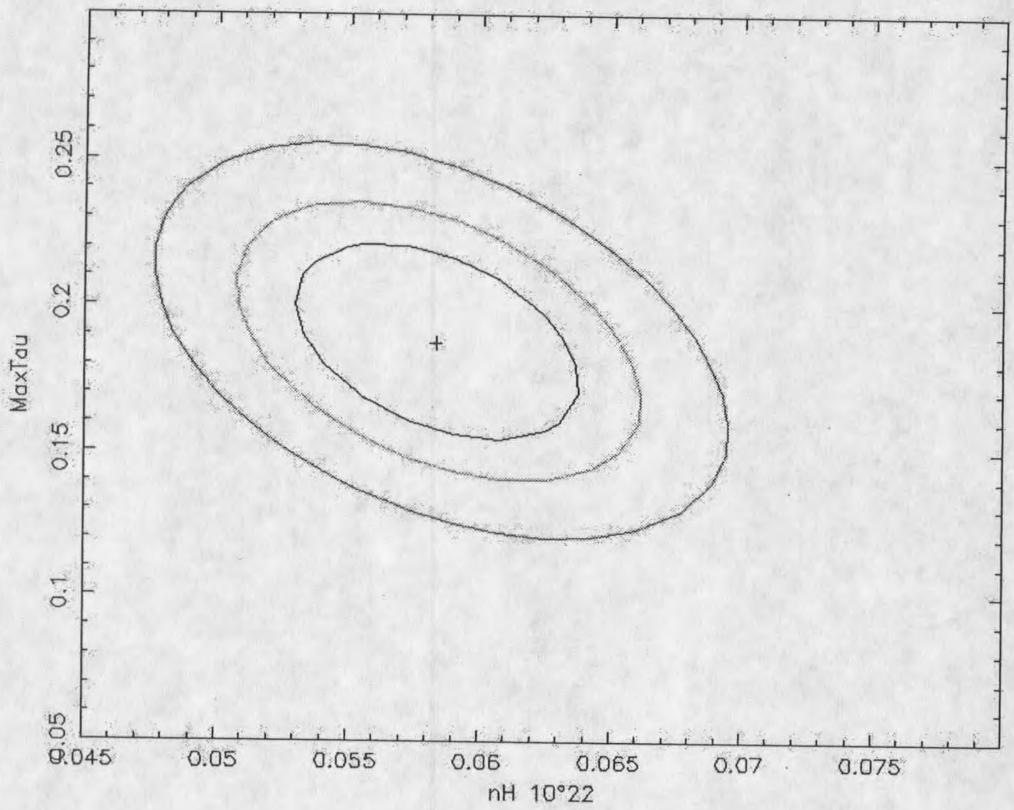

Figure 3.9: Contour plot of optical depth of O VIII also shows ellipses with major axis at a 45 degree angle to the horizontal. This indicates that increasing the neutral hydrogen will decrease O VIII if all other parameters remain constant. This particular set of contours was made for MCG-6-30-15 but the interdependence of the parameters is present in all models.

Object	RA	Declog $N_h(cm^{-2})$	
Akn 120	05 16 9.7	-00 09 47.3	21.09
MCG-6-30-15	13 33 01.8	-34 02 27	20.63
NGC 3227	10 23 10.9	19 49 35.9	20.34

Table 3.3: Neutral Hydrogen Column Densities measured by radio techniques for each of the galaxies analyzed in this work. Values from Dickey and Lockman (1990).

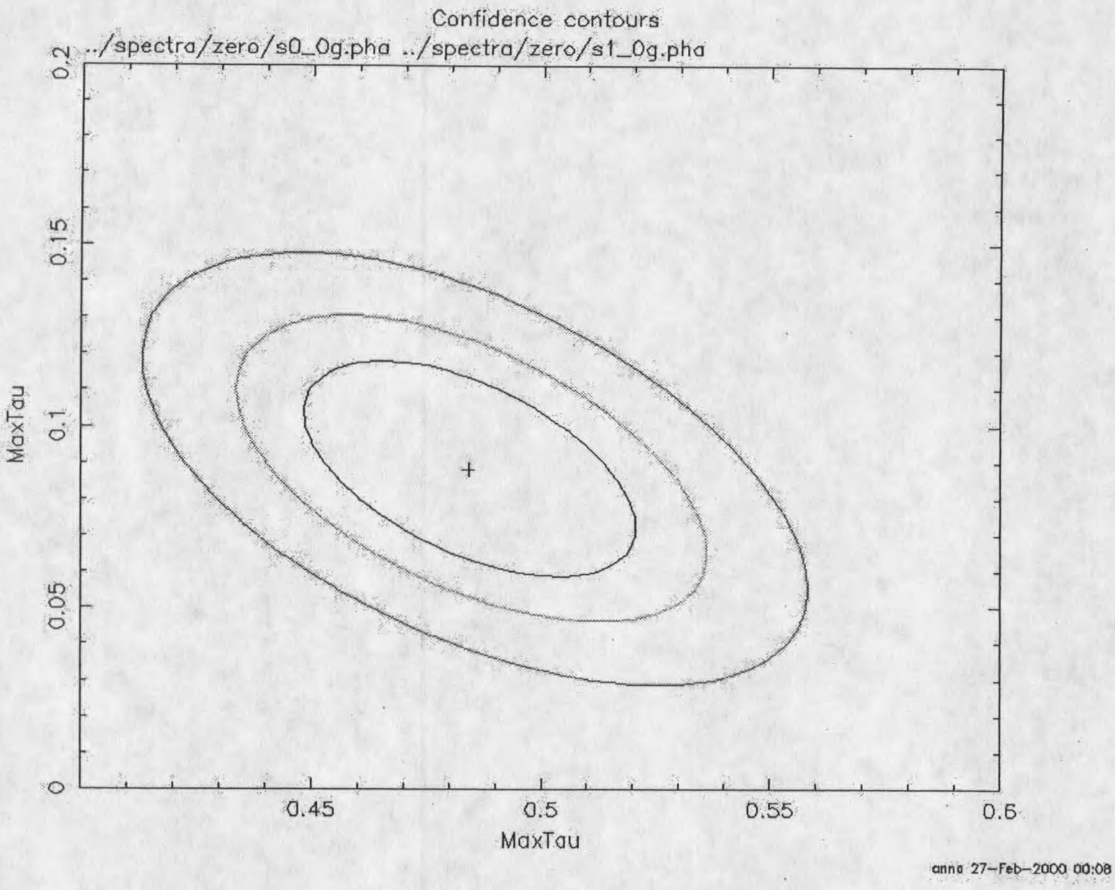

Figure 3.10: Contour plots of optical depth of O VII vs O VIII show ellipses with major axis at a 45 degree angle to the horizontal. This figure was made from an archival ASCA observation of NGC 5548.

tends to decrease one oxygen edge when the other is increased. This effect can be minimized in two ways: first, by ensuring that the edge energies are well fit, which can be done by examining the residual before and after the oxygen edges are fit to the model, and second, by freezing the edge energies during the fit of the edge depth.

In summary, our procedure for fitting soft X-ray features is as follows. The photon index is frozen to the value previously obtained by fitting the GIS detectors from 3–10 keV with the iron features removed. Then the full spectrum, down to 0.7 keV is fit with the neutral hydrogen frozen at the value given by the 21 cm measurement; the oxygen edge energies are frozen to a value chosen heuristically by examining residuals before and after their inclusion in the model.

Photoionization Models

In general, the function of photoionization codes is to use models of incident powerlaw radiation on a broadline cloud to predict the relative intensities and line width of spectral lines and the optical depth of absorption edges as discussed above. The two "industry-standard" photoionization codes are ION, developed by Hagai Netzer and Ian George, and CLOUDY developed by G. Ferland and his collaborators. Both operate on more or less the same premises: the central engine is assumed to produce a continuum spectrum which is provided by the user; this creates a spectrum $F(\varepsilon)$. This spectrum is then incident upon an ionized gas where the incident photons are scattered and absorbed. The ionization state of the gas is described by (Krolik and Kriss, 1995):

$$\xi = \frac{\int F(\varepsilon) d\varepsilon}{4\pi r^2 n_H c} \tag{3.4}$$

where r is the distance between the central engine and the ionizing medium. The gas is also assumed to have an equivalent column density n_h which is the amount of hydrogen the continuum spectrum would encounter if the ionized gas had solar abundance. Many models also have a covering factor parameter ϵ, which indicates the fraction of the volume within the cloud of ionized gas which contains ionizing material. A third exemplary photoionization code also exists, MAPPINGS (Dopita 1995, Dopita and Sutherland 1995, Dopita and Sutherland 1996), which is designed to include spectral signatures of fast and slow shocks. Unfortunately, the energy resolution of ASCA is not adequate to measure the differences in line profiles necessary to take advantage of MAPPINGS' sophistication, so it is not used in this work.

The tabulated results of the photoionization code ION were provided to our group by their creator, Dr. Hagai Netzer.The main difference between ION and CLOUDY is that ION contains a more complete treatment of reflection of the continuum spectrum off the ionized gas. ION is valid for densities from 10 to $10^{14} cm^{-3}$, which encompasses the expected density of the warm absorber ($10^9 - 10^{12} cm^{-3}$). ION is designed only for X-ray analysis and does not extend down to the optical or up to the γ–ray region of the spectrum.

ION is arranged in tables with fixed photon index and covering factor, each of which has variable ionization parameter and equivalent column density. The ionization parameter used by ION is not the same as that used for other codes; instead, it is defined by (Netzer 1993):

$$U_x = \int_{0.1keV}^{10kev} \frac{\frac{L_\nu}{h\nu}}{4\pi r^2 n_H c} d\nu \tag{3.5}$$

and, for the typical Seyfert 1 spectrum, is related to the other standard X-ray ionizations by (Netzer, 1996):

$$U = 141 U_x \tag{3.6}$$

and

$$\xi = 4.9 \times 10^3 U_x. \qquad (3.7)$$

The reason for the modified ionization parameter is that the other, broader-band, ionization parameters are dominated by the flux in the ultraviolet bump, which is not well correlated with X-ray ionization.

Techniques of Timing Analysis

X-ray light curves of AGN vary considerably in their complexity; most vary by factors of 100% , sometimes over timescales as short as hours (Kunieda *et. al.*, 1990). In addition, some spectral variability is seen in the different bands of the light curve (Netzer *et. al.* 1994). Although not as dramatic as the variability of Galactic black holes (Poutanen and Fabian, 1999), variations of the different bands still give insight into the structure and dynamics of the galaxy-sized black hole and accretion disk thought to be at the center of AGN, and the warm absorber thought to be within the BLR (BroadLine Region).

Hardness Ratios

To best separate the behavior of the physical features from the overall luminosity, we follow the example of Netzer *et. al.* (1994) and define four hardness ratios:

$$R_1 = \frac{(\text{Counts}3 - 5keV)}{(\text{Counts}0.4 - 0.6keV)} \qquad (3.8)$$

$$R_2 = \frac{(\text{Counts}3 - 5keV)}{(\text{Counts}0.6 - 1.3keV)} \qquad (3.9)$$

$$R_3 = \frac{(\text{Counts}7.5 - 10keV)}{(\text{Counts}3 - 5keV)} \tag{3.10}$$

$$R_4 = \frac{(\text{Counts}5 - 7.5keV)}{(\text{Counts}3 - 5keV)} \tag{3.11}$$

within the ASCA energy bandpass. R_1 is the ratio of two spectral regions which are dominated by the powerlaw continuum and were initially thought to have few other significantly observable features; extreme caution must be taken in the interpretation of data from this region due to the well-documented radiation damage of the SIS detectors. R_2 is the ratio of the 3–5 keV region, which contains minimal spectral information other than the photon index, and the 0.6–1.3 keV region, which typically exhibits neutral hydrogen absorption by the ISM and our Galaxy as well as two oxygen absorption edges which correspond to O VII and O VIII. Variation of R_2, which typically has the best signal-to-noise ratio of any of the hardness ratios, gives information about the variation of the warm absorber. R_3 is at first glance the ratio of two regions which are entirely dominated by the powerlaw; however, close examination of the spectral shape often shows the low-energy end of the cold reflection hump which peaks near 12 keV. Thus, variations in R_3, which are naively interpreted as variation in the photon index, are more likely to correspond to variations in the cold reflection hump. Finally, the hardness ratio R_4, which divides the 5–7.5 keV region typically dominated by iron Kα absorption and emission features by the 3–5 keV region which contains powerlaw information alone, can yield information about the variation of the iron emission line. However, the typical iron line normalization for a Seyfert 1 galaxy is two orders of magnitude smaller than the normalization of the continuum radiation; this means that extreme care should be taken in interpreting the changes in R_4 as variation in the iron absorption and emission features.

Phenomenological Classification of Timing Data

When presented with the light curve and hardness ratios from a long observation, or of several short observations, the question of how to group states with similar morphology together arises. Studies of spectral features cannot be done of individual bins on a light curve, since counting statistics on this timescale are inadequate. Instead, light curve bins must be added together in a self-consistent manner to create a statistically viable spectrum.

Standard Techniques

When an observation of a galaxy is long enough that more than one spectrum with statistically valid features may be extracted, observers use two standard filters to observe them. The first is to divide the light curve into the sequential time bins- that is, the first 20 ksec of an observation, the second 20 ksec of the observation, and so forth, as shown in Figure 3.11. The spectra extracted in this manner then represent averages over the time bin from which they originate. This technique has been used extensively by previous researchers; for example, Otani *et. al.* (1995) used temporal filters to analyze the warm absorber in MCG-6-30-15 and found that O VIII changed depending on the luminosity of the source.

For rapidly varying sources which do not stay at one luminosity long enough to obtain a valid spectrum, it is often convenient to group together non-sequential

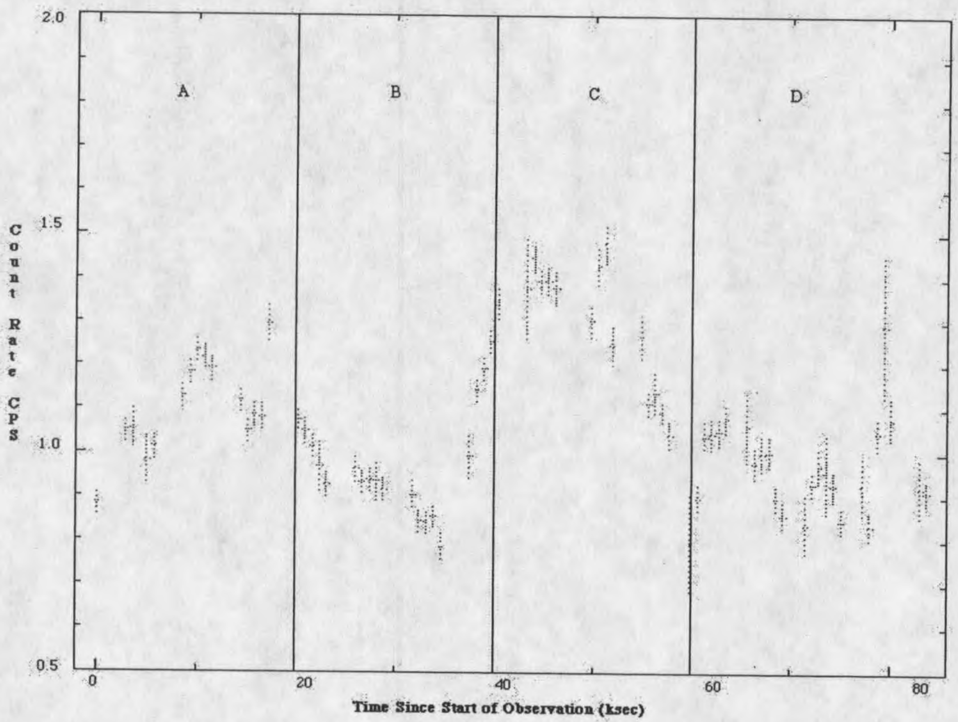

Figure 3.11: Temporal filters for the light curve of NGC 3227. These particular filters were made from an archival ASCA observation of NGC 3227.

points of the same luminosity to see whether extremely high luminosity points differ significantly from extremely low luminosity points. This method has been used by a number of observers, including Iwasawa *et. al.* (1996), who used it to show that high luminosity states from MCG-6-30-15 have different iron line profiles than do low luminosity states.

Each of these selection methods has drawbacks. If the timescale of variation of a source is longer than the bin used for temporal filters, some details of the spectral variation within the bin may be lost. Luminosity filters also have the disadvantage that not all points of the same luminosity are necessarily associated with the same spectrum. For instance, luminosity filters will group together points where the source's luminosity is increasing and decreasing. Galactic black holes have been observed to have spectra which vary throughout a flare cycle, showing five different spectral states (Di Matteo, Celotti, and Fabian, 1998). At least one source (Kellen, 1997) has exhibited spectral differences between increasing and decreasing states.

The Kunieda Method

In order to address some of these concerns, Kunieda *et. al* (1987) developed a method of sorting states according to their phenomenology and hardness ratio. The observation in question was of NGC 6814, which exhibited quiescent behavior with distinct flare states interspersed throughout the observation; the flare states had a notably different higher hardness ratio R_2 than did the other epochs of the observation. They showed that the flare states, of which there were three, had spectra that were more closely related to each other than to the temporally closer quiescent states with lower hardness ratio; thus, there is reason to believe that selecting by either phenomenology or hardness is superior to selection by time during the observation or by luminosity alone.

Unfortunately, a cataclysmic variable was discovered in the field of view of NGC 6814 (Leighly 1992), invalidating the conclusions previously drawn from the observation. While the conclusions may not be valid for AGN, the techniques developed are, and our object here is to explore them in further detail. For MCG-6-30-15, Kunieda's method leaves unanswered the fundamental question: if luminosity and hardness ratio are not directly related to the phenomenology of such a rapidly varying source, what is the preferred method of spectral selection?

Two New Methods of Classification

Some AGN, such as NGC 3227, can easily be modelled by a simple linear increase and exponential decrease characteristic of flares caused by magnetic reconnection. Most AGN do not have such distinct flares, but rather exhibit a number of small flares which overlap one another to create rapid variability. In the latter case, classifying the individual bins of the light curve according to their instantaneous state may be appropriate. For such instances, the author developed the classification scheme shown in Figure 3.12.

Those timing bins which were within 1σ error of both adjoining timing bins were sorted into the *constant* classification. For all other timing bins, a right-hand and

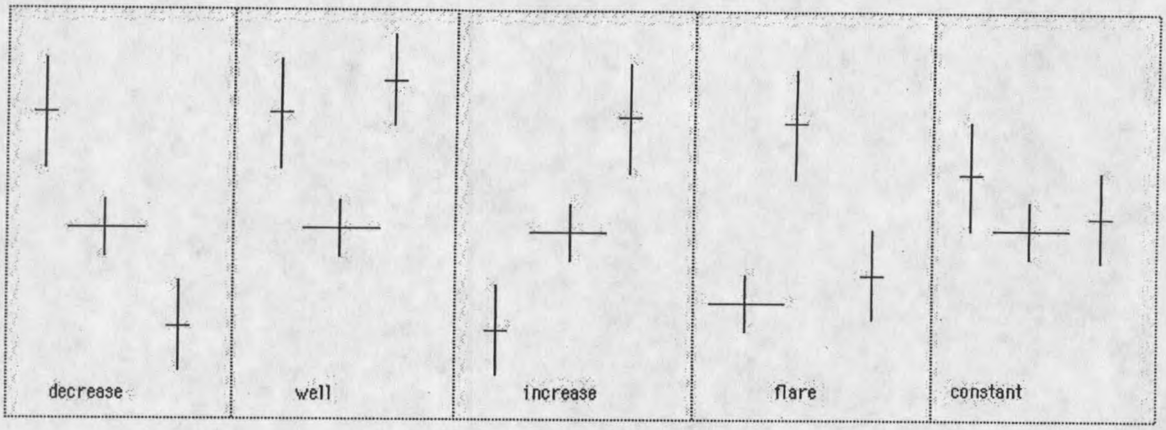

Figure 3.12: The four state classifications are shown: flare and well states are just local maxima and minima, respectively, and increasing and decreasing states are shown-all classifications are applied to the middle point.

left-hand derivatives were calculated using the formulae:

$$\frac{(dL)}{(dt)_{left}} = \frac{(L_i - L_{i-1})}{(t_i - t_{i-1})} \tag{3.12}$$

and

$$\frac{(dL)}{(dt)_{right}} = \frac{(L_{i+1} - L_i)}{(t_{i+1} - t_i)} \tag{3.13}$$

where L_i denotes the intensity of the i^{th} point in the light curve and t_i denotes the time at the beginning of the i^{th} point in the light curve. This can be roughly illustrated by a diagram: Figure 3.12 shows the four states for which the data points differ by amounts larger than their error bars. The state *well* consisted of those points for which the left derivative was negative and the right derivative positive and both had absolute values larger than α. Thus, as suggested by its name, local minima for which the variation was larger than a minimal value lie mostly within the *well* state. The *flare* state is essentially opposite of the *well* state; those events associated with a positive left derivative and a negative right derivative, both with absolute value above the cutoff α were classified as *flare*; thus, this state consists of the largest local maxima of the light curve. The *increasing* state consists of all points having both left and right derivatives positive and greater than α; these states then correspond to times for which the luminosity is very rigorously increasing. The *decreasing* state consists of all points with left and right derivatives both negative and having absolute value larger than α; these points are epochs in the light curve during which the luminosity is rapidly decreasing.

Another means of classifying points in an observation arises when one notices that the correlation between some of the hardness ratios and the luminosity is not 1:1; that is, two portions of the observation with the same luminosity have different hardness ratios. An example of this is shown in Figure 3.13, which shows that the Seyfert 1 galaxy NGC 5548 has multiple values of hardness ratio R_3 for the same luminosity. Physically, this suggests that the photon index is varying independently from the luminosity of the galaxy, so sorting points in the light curve independently by the two variables may yield insight into the dynamics of the inner accretion disk and corona. This trait is not characteristic of all Seyfert 1 galaxies; MCG-6-30-15, for instance, exhibits little variation of R_3 while the luminosity varies rapidly. This is discussed in detail in Chapter 5. In summary, the interdependence of the hardness ratios must be considered separately for each source, and a suitable filter defined which will yield physically interesting data.

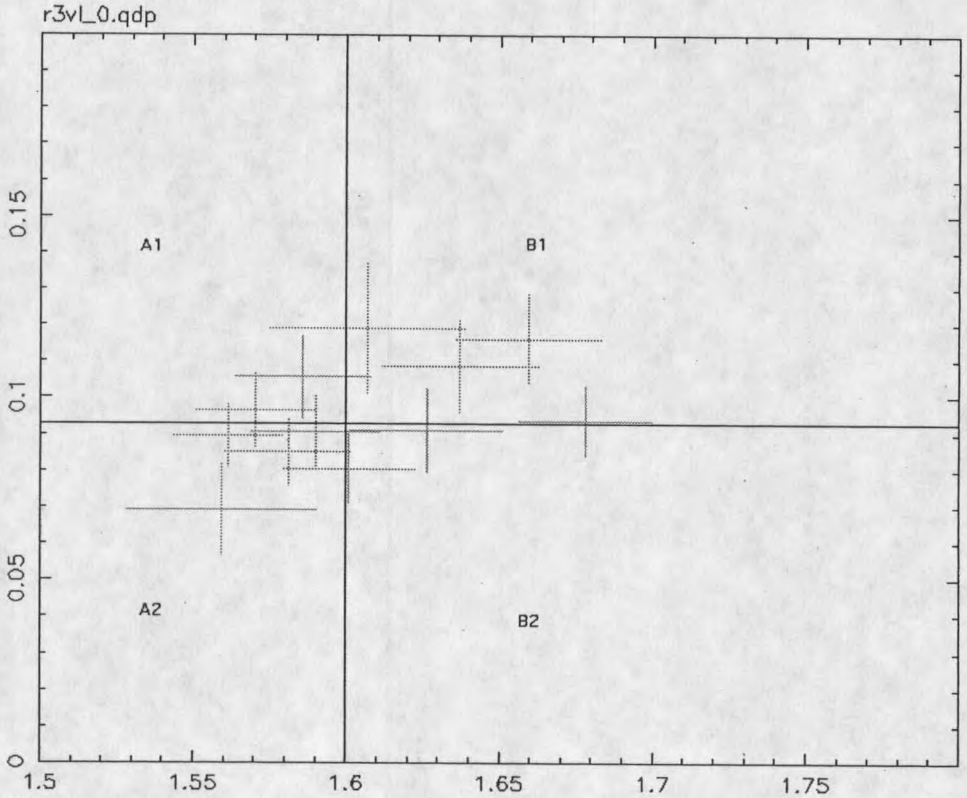

Figure 3.13: Some Seyfert 1 galaxies have multiple values for a hardness ratio when at the same luminosity. This particular plot was made from the 1997 ASCA observation of NGC 5548(now archival);in this case, the data points are classified in four bins chosen by hardness and luminosity.

CHAPTER 4

X-RAY ANALYSIS OF ARKARIAN 120

La nuit parfois ravive une plante singulière dont la lueur décompose les chambres meublées en massifs d'ombre.[1]

(Francois Ponge, "La Bougie" **Le Partie Pris des Choses**)

Introduction

Located approximately 131 Mpc from Earth, Arkarian 120 is one of the most distant well-studied Seyfert 1 galaxy. Arkarian 120 was discovered in the optical by Osterbrock at Lick Observatory in 1975, and subsequently identified as a Seyfert 1 galaxy. The first X-ray detection of the object was made by the X-ray satellite UHURU in 1978. The soft X-ray spectrum of Arkarian 120 was proven by ROSAT (Brandt *et. al.*, 1993) to be consistent with the galactic hydrogen absorption of $9.75 \pm 1.61 \times 10^{20} cm^{-2}$ (Stark *et. al.*, 1992). The cosmological redshift, measured by studies of the optical lines of the galaxy, is z=0.033 (Ostriker *et. al* 1991).

Earlier analyses of this source have produced a range of values for the continuum

[1]Translation: The night sometimes revives a singular plant whose light decomposes furnished rooms into massive shadows.

power law, depending on detector and model. Analysis of the EXOSAT observation produced a 2–10 keV power law of $\Gamma = 2.19^{+0.08}_{-0.11}$ (Turner and Pounds, 1989), while the GINGA observation showed Compton reflection and produced a modified power law of $\Gamma = 1.95^{+0.15}_{-0.09}$ when the reflection feature was satisfactorily fit (Nandra, 1991). A ROSAT observation of this source fixed the primary photon index to the value obtained by Nandra (1991) and found that a second continuum component (bremsstrahlung, blackbody, or a second power law) was needed to adequately explain the 0.1–2.0 keV continuum.

One of many recent optical studies of this source showed that its optical continuum and emission line variability have the same amplitude over shorter (less than 2 month) and longer (greater than 4 month) timescales. This suggests a broad line region (BLR) of 40 light days (Winge, 1998). Arkarian 120 (Akn 120) was observed by EXOSAT (Turner and Pounds, 1989), and as part of the EXOSAT spectral survey of AGN. This was the first indication that Akn 120 has a significantly steeper slope than most other Seyfert 1 galaxies, with $\Gamma = 2.10^{+0.06}_{-0.11}$. An excess emission in the soft X-rays was also suggested by the data. A subsequent GINGA observation of the source showed a cold reflection hump above 10 keV and a correspondingly shallower photon index (Nandra, 1991).

A 1991 ROSAT observation of Arkarian 120 allowed detailed fitting of the soft X-ray component of the source (Brandt *et. al.*, 1993). The source did not vary more than 25% over the course of the observation. Brandt *et. al.* found that a simple power law model corrected for galactic hydrogen absorption did not adequately fit the data, but three models with secondary continuum components did: double power law, bremsstrahlung, and blackbody models all provided fits with roughly equivalent goodness of fit. In contrast, models with oxygen emission and absorption fit the data substantially less well.

In this chapter, the 1994 ASCA observation of Arkarian 120 is analyzed and compared to standard models of Seyfert 1 Galaxies. Section 4.2 describes the data extraction and image analysis techniques used. Section 4.3 contains timing analysis of this observation. Section 4.4 contains the results of spectral analysis of the source. Section 4.5 contains a discussion of the analyses in light of the previous observations discussed above.

Data Extraction

Arkarian 120 was observed September 29–30 1994 for 100 ks; the principal investigator was Dr. Hideyo Kunieda. The data was extracted using XSELECT v.1.4, which was installed by the author on a SUN workstation and tested against the existing versions at NASA's Goddard Space Flight Center via remote connection. A cutoff rigidity of 6 GeV c^{-2} was used and passage during the South Atlantic Anomaly (SAA) was excluded from the data set.

Dec= -00 deg 09′47.3”

The source counts for Arkarian 120 were extracted from a circular region 5 arcminutes in diameter centered at RA= 05 16 9.7, Dec= -00 09 47.3. Spectra extracted from the available source-free area on the detector had no counts, thus, a blank sky background subtraction was used. When a spectrum was subtracted from the source

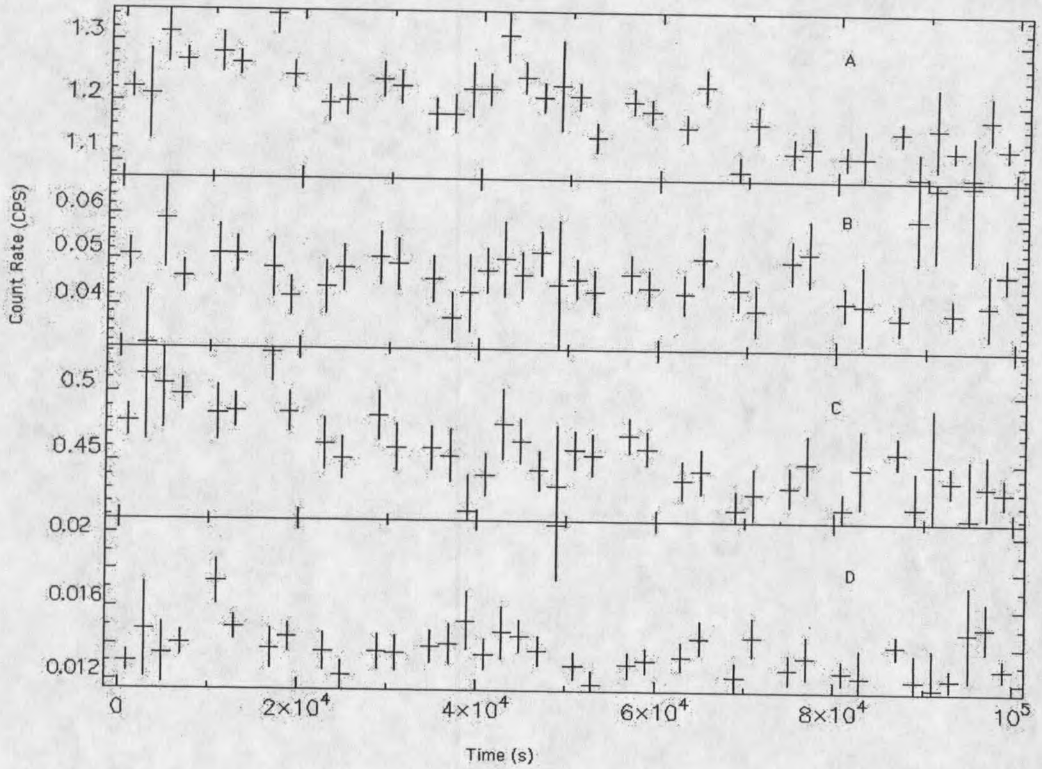

Figure 4.1: Count Rate vs. time for ASCA Observation of Arkarian 120 using SIS detectors. A) is the total count rate; B) is for 0.4–0.6 keV, C) 0.6–1.3 keV, and D) 3–5 keV. These data were extracted from the archival ASCA observation.

region on an average background image of the X-ray sky, it corresponded to a count rate of 0.018 CPS. Thus, in this case, a blank sky background was used for the SIS as well as GIS spectra.

Timing Analysis

The SIS light curve of Arkarian 120 is shown by Figure 4.1 which includes the total count rate and the count rates of the ultrasoft (0.4–0.6 keV), soft (0.6–1.3 keV) and medium (3–5 keV) spectral windows. Figure 4.1 shows variation in the total light curve of about 20% , which is consistent with the previous ROSAT observation of this source (Brandt *et. al.*, 1993). With the exception of three points near the end of the observation, the ultrasoft (0.4–0.6 keV) band seems well correlated with the total count rate. The soft (0.6–1.3 keV) band seems even better correlated with the total count rate, although the better correlation could easily be due to the fact that the SIS detectors have better response above 0.6 keV. In contrast, the medium (3–5 keV) band does not appear well-correlated to the total count rate which suggests possible variation of the photon index.

During this observation the GIS detectors had a slightly longer exposure (44.3 ks) than did the SIS detectors (40.2 ks), so the light curves must be analyzed separately. The GIS light curve for the observation is as shown in Figure 4.2. The amplitude of the variation of the total GIS count rate is approximately 20% , as one would expect from the SIS count rate. The medium energy band (3–5 keV) shows little variation, some of which appears to be correlated to the variations to the total count rate and some of which does not. The iron line (5–7.5 keV) and hard (7.5–10 keV) bands show similar trends, indicating possible variation in the continuum shape.

The primary statistics associated with the two light curves and hardness ratios are shown in Table 4.1. While the light curve has a small probability of being consistent with a constant for both the GIS and SIS light curves, the likelihood is small. In contrast, the hardness ratios are all statistically inconsistant with variation. To explore the possibility that the photon index is varying, we examine hardness ratio R_3 in terms of the two components; if the counts from 3–5 keV are plotted against

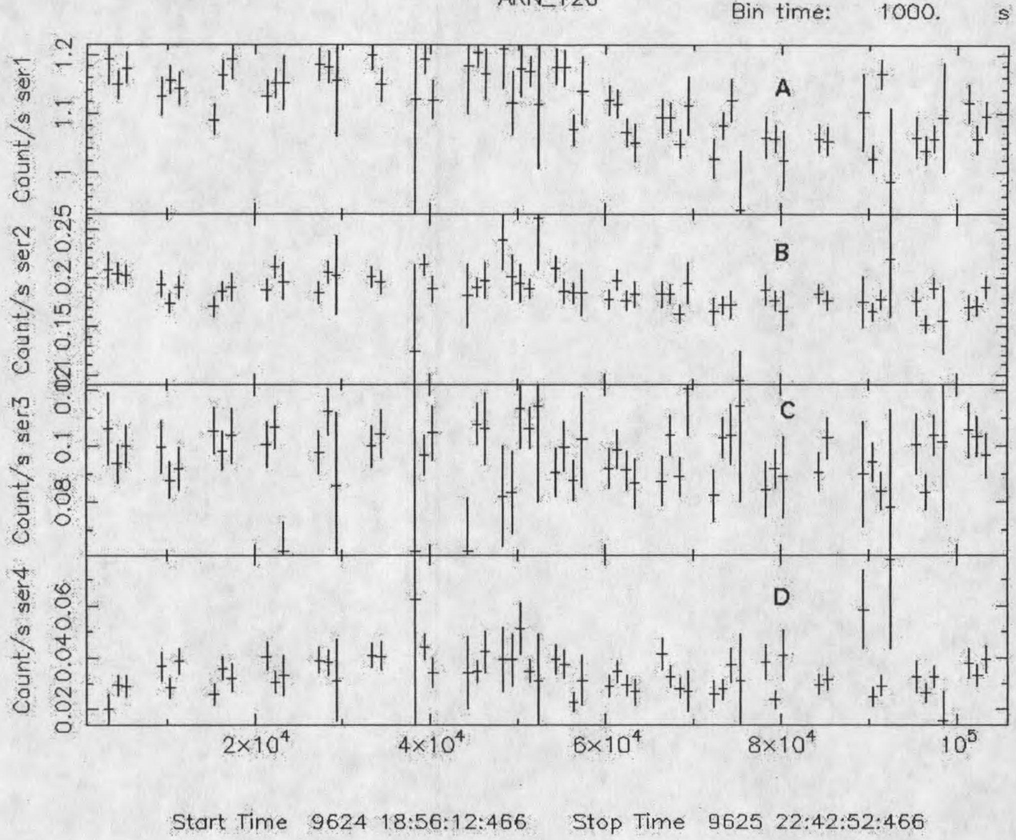

Figure 4.2: Count Rate vs. time for ASCA Observation of Arkarian 120 using GIS detectors.

	GIS	SIS	R_1	R_2	R_3	R_4
Ave.	1.12	1.19	1.28	0.122	0.079	0.229
σ	0.08	0.08	1.693	0.151	0.104	0.277
Min	0.937	0.969	0	0	0	0
Max	1.59	1.44	10	0.48	0.50	1.22
χ^2Prob. Const.	0.066	0.059	0	0	0	0
KS Prob. Const.	1.1x10^{-28}	2.56x10^{-26}	0	0	0	0

Table 4.1: The average, standard deviation, minimum, maximum, and the χ^2 and Kolmogorov-Smirnov probabilities that each curve is constant are shown. The hardness ratios R_1 and R_2 are taken with SIS data alone, while R_3 and R_4 are taken with GIS data alone. The definitions of the hardness ratios are given in Chapter 3.

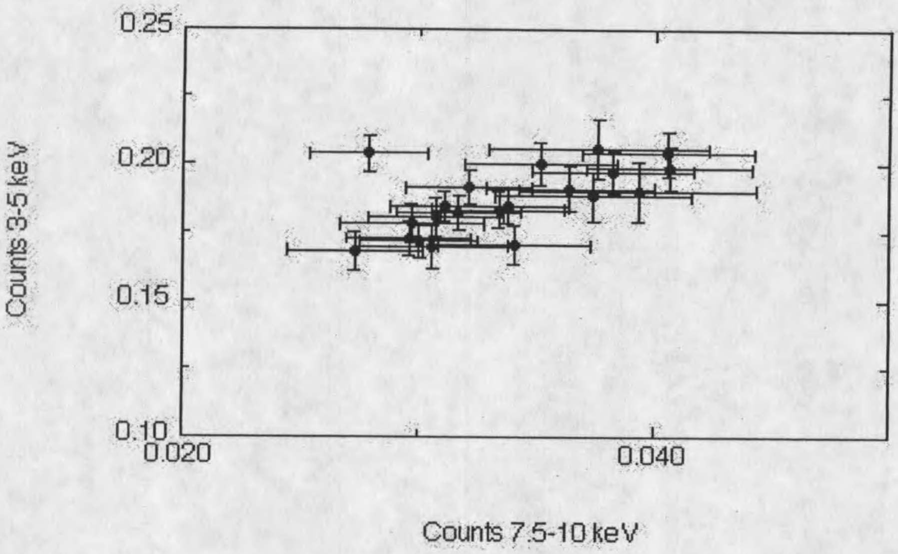

Figure 4.3: Counts 7.5–10 keV vs. 3–5 keV. Each point represents a 5 ks time interval of the observation.

the counts from 7.5–10 keV, a straight line with slope R_3 would indicate that the photon index is constant over the course of the observation. This plot is as shown in Figure 4.3. The linearity of the plot suggests a constant hardness ratio during the observation; this, in turn, suggests that the photon index does not vary over the course of the observation. A single data point is inconsistent with this linear trend; one point with low hard counts has extremely high medium counts. This suggests that a single 5 ks interval within the light curve may have a different photon index from the rest.

Next, we examine the possibility that the iron line spectral band varies during the observation, as the statistics of the hardness ratio R_4 suggest. Figures 4.4 and 4.5 show the hardness ratio R_4 plotted against count rate and against the hardness ratio R_3. At low luminosities, there is some indication that R_4 may be anticorrelated

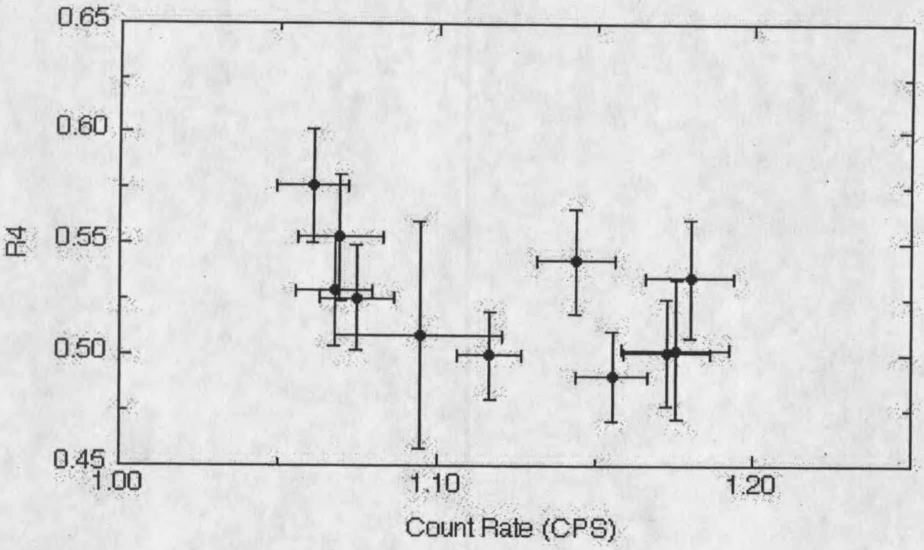

Figure 4.4: R_4 plotted against the total GIS count rate. All counts are taken from the combined GIS detectors.

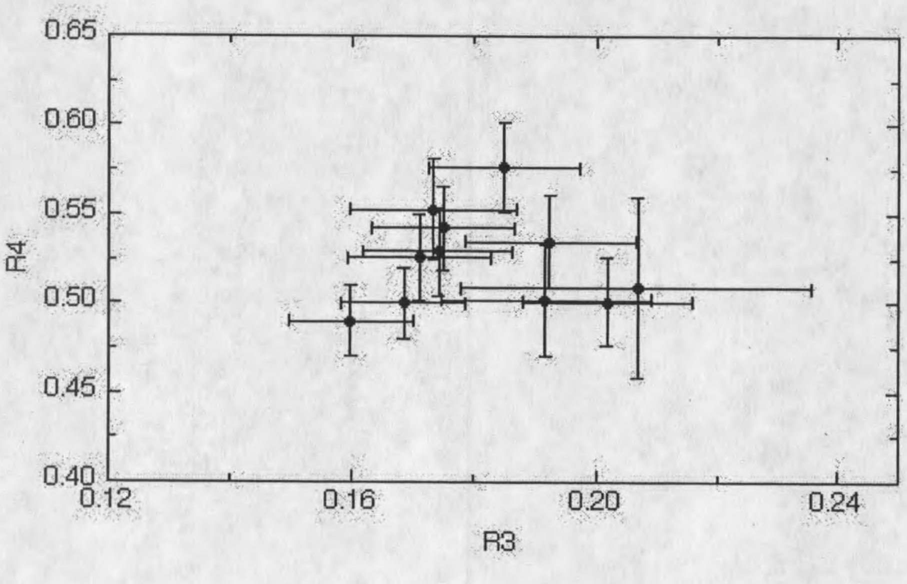

Figure 4.5: R_4 plotted against R_3. All counts are taken from the combined GIS detectors.

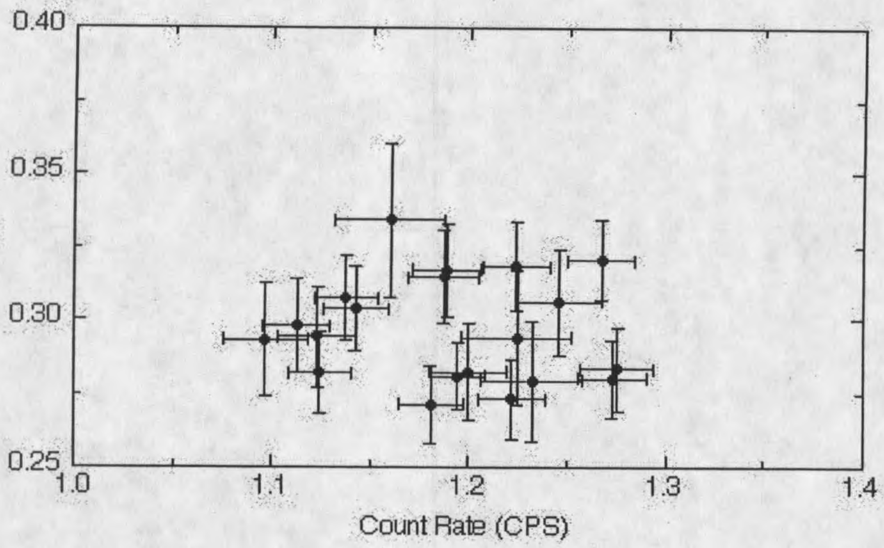

Figure 4.6: R_2 plotted against the total SIS count rate. All counts are taken from the combined SIS detectors.

with count rate, but there appears to be no such correlation for higher count rates. A longer observation would be needed to confirm whether any such correlation exists for ASCA data. No correlation between R_3 and R_4 is apparent; this might mean that the iron line varies while the photon index does not, but care must be taken in interpreting the data in this manner since the iron line represents a very small percentage of the total count rate even in the 5.0–7.5 keV band.

In the case of Arkarian 120, the hardness ratios R_1 and R_2 may have the physical significance of continuum changes rather than indicating possible changes in warm absorption. In sources with strong warm absorption, R_2 corresponds to changes in the column depth of ionized oxygen. To explore whether R_2 is correlated with either count rate or continuum hardness, we plot it against each as shown in Figures 4.6 4.7.

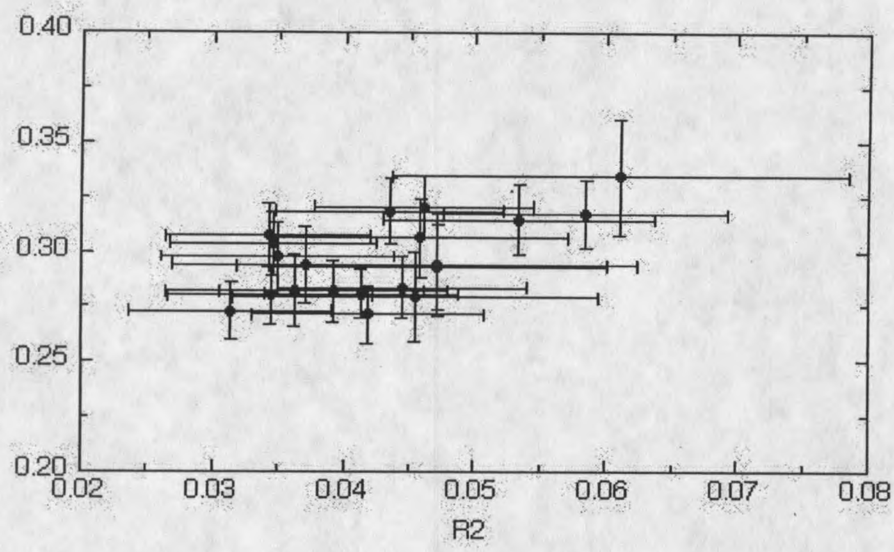

Figure 4.7: R_2 plotted against R_3. All counts are taken from the combined SIS detectors.

No correlation exists between R_2 and R_3, suggesting that R_2 might vary during the course of the observation since R_3 does not. There is some indication that R_2 is correlated with luminosity during the low count-rate portion of the observation, but no correlation at all when the count rate is high. Arkarian 120 is not particularly well-fit to the oxygen edges which characterize warm absorption in this region (as discussed in the next section), so the possible variation in R_2 probably corresponds to changes in the low-energy continuum component.

Spectral Analysis

Following the recent standard, the spectrum of this observation was grouped by a minimum of 20 counts to ensure the validity of the χ^2 coefficient (George *et. al.* 1998). This does have the undesirable effect of reducing at least some of the absorption edge depths (Kellen, 1997); for this reason, the edge depth is verified by measurement

Model	Parameters	χ^2	d.o.f.
Simple Power law	$\Gamma = 1.88^{+0.04}_{-0.03}$	262	261
Absorption by Dust	$\Gamma = 1.64^{+0.03}_{-0.03}$ $\alpha = 0.25^{+0.03}_{-0.03}$	262.4	260
Absorption by Gas	$\Gamma = 1.88^{+0.03}_{-0.03}$ $n_H = 0.0^{+15} \times 10^{20}$	262.4536	260
Reflection off Neutral Gas	$\Gamma = 1.86^{+0.03}_{-0.03}$ $\epsilon = 0.15^{+0.42}_{-0.15}$	262.5	260
Reflection off Ionized Gas	$\Gamma = 1.95^{+0.03}_{-0.03}$ $\epsilon = 0.65^{+0.19}_{-0.18}$ $\xi = 996.1$	263.8893	271

Table 4.2: Best-fit parameters of continuum models to the 2-10 keV window of Arkarian 120, with iron line region excluded. Γ is the photon index, n is the normalization of the model in units of photons $keV^{-1}cm^{-2}sec^{-1}$ at 1 keV. For the absorption models, α is the index for dust, while n_H is the equivalent neutral hydrogen column of gas. For reflection models, ϵ is the fraction of the continuum which is reflected and ξ is the ionization parameter (defined in Chapter 3). The reflection models have an inclination of 30 degrees, in agreement with the optically measured inclination of this galaxy. The value of χ^2 is the fitting statistic for the model, and d.o.f. is the number of degrees of freedom of the model. Errors shown are 1σ confidence regions.

on the ungrouped light curve as well when, as for this source, standard grouping combines a significant number of channels in the energy band of the edge in question.

Hard X-ray Continuum

Before fitting the continuum, the spectral window with significant emission from the iron Kα fluorescence line must be excluded. In Figure 4.8, the iron line is seen to fall below 5% of its maximum at 5.5 keV on the low end; the iron absorption edge is below 7.1 keV, so the ignored region was chosen as 5.5–7.2 keV. The best-fit parameters for a simple power law are as shown in Table 4.2.

Of the continuum fits, only three are viable options: the simple power law, absorption by dust, and reflection off an ionized medium. To differentiate between the

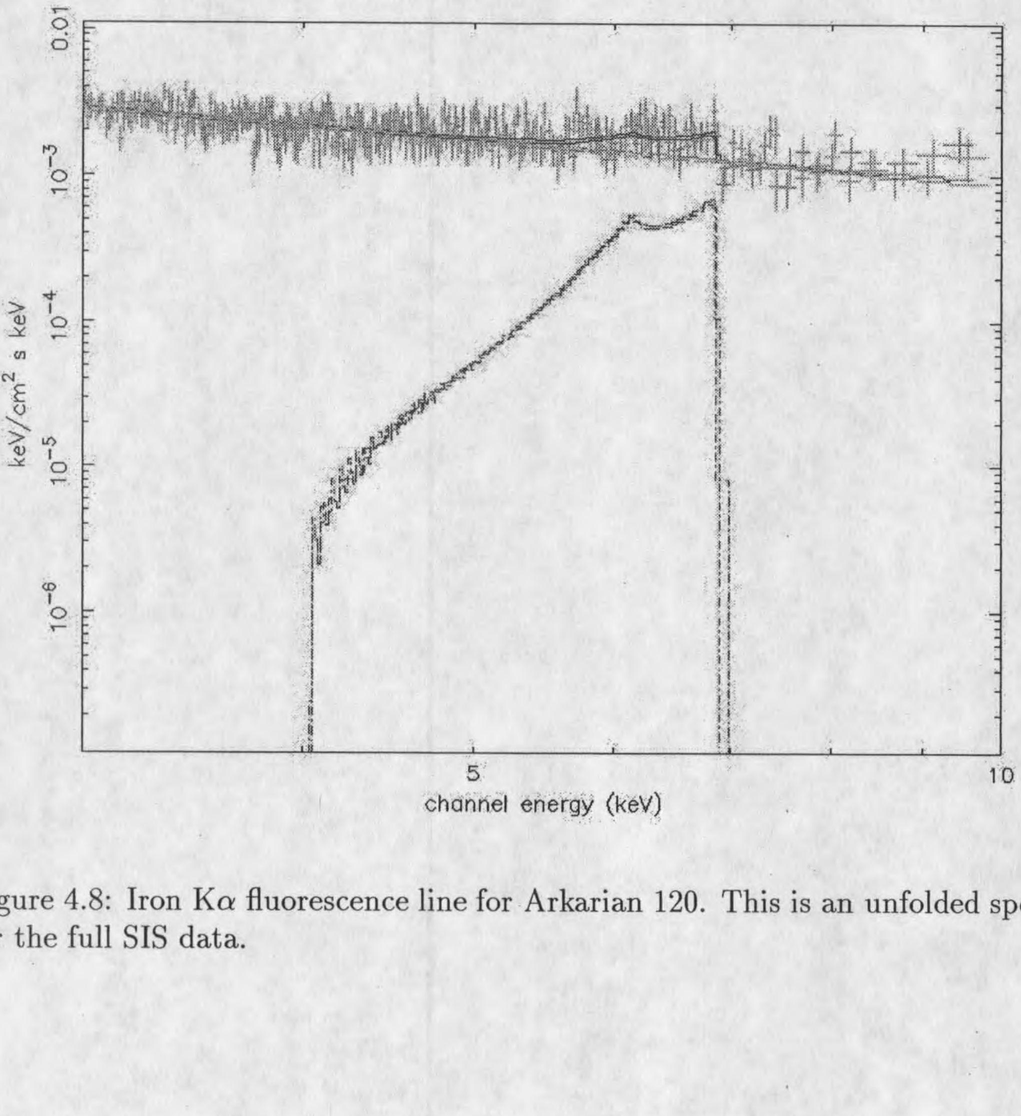

Figure 4.8: Iron Kα fluorescence line for Arkarian 120. This is an unfolded spectrum for the full SIS data.

three, we can examine the few lowest energy bins of the SIS spectrum. Below the O VII absorption edge, the absorption by the ISM is minimal, so that a correctly fit power law will match the lowest energy bins without any absorption corrections.

Soft Energy Spectrum

The most prominent continuum feature below 2 keV is the absorption by neutral hydrogen. Since the Galactic value of neutral hydrogen absorption must be a lower limit for N_h and the ROSAT value an upper limit, we constrain the value of the neutral hydrogen to the range of uncertainty obtained by Brandt *et. al.* (1993). The full spectrum was fit to a simple power law and neutral hydrogen absorption model, with results shown in Figure 4.9. The most striking difference is the strong soft energy excess indicated by the large negative value for the signed χ^2 statistic at the low energy end of the spectrum. The features are well correlated between the two detectors, and there is also the possibility of absorption and emission features below 1 keV.

We thus attempt to fit the soft X-ray data to several continuum models which fit the ROSAT data, as well as more complicated emission/absorption models in keeping with ASCA's superior spectral resolution. The results of the fits are summarized in Table 4.3.

The soft X-ray components of a simple blackbody (Blackbody I), thermal bremsstrahlung, and disk emission fit the data best, but their fitting statistics are not compelling. However, these three models fit the data significantly better than do the single power

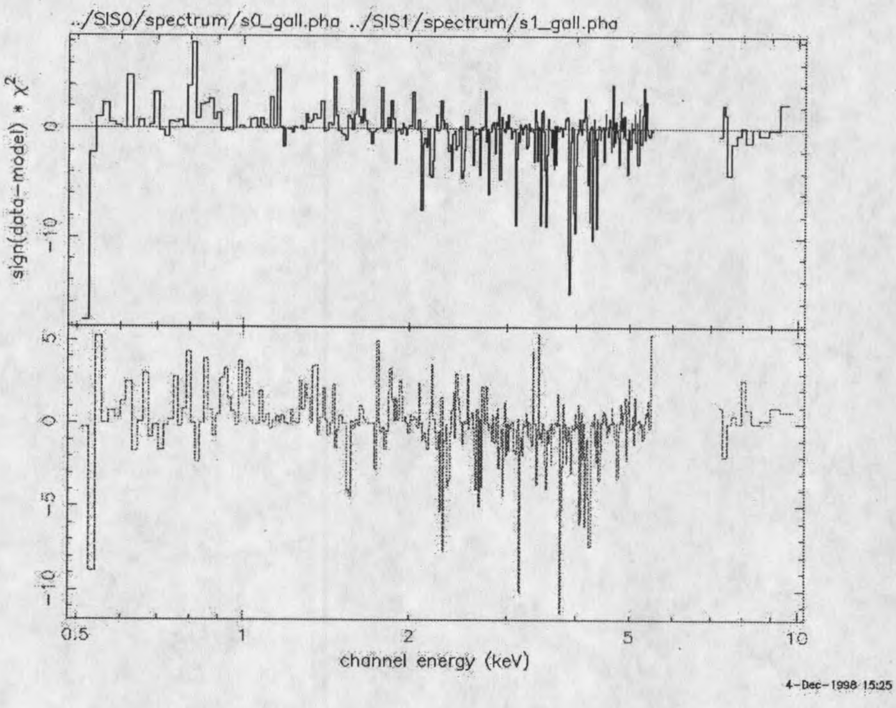

Figure 4.9: χ^2 deviation of soft X-rays from Simple Power law Model. This plot was made using the SIS detectors.

Model	n_1	Other Parameters	χ^2	d.o.f.
Power Law & Blackbody I	8.26×10^{-3}	kT=$0.329^{+0.028}_{-0.021}$	687.7	608
		$n_2 = 2.44^{+0.32}_{-0.51} \times 10^{-5}$		
Power Law & Brems.	8.04×10^{-3}	kT=$1.07^{+0.20}_{-0.15}$	692.8	607
		$n_2 = 3.11^{+0.70}_{-0.58} \times 10^{-3}$		
Double Power Law	8.5×10^{-3}	$\Gamma = 2.383^{+0.178}_{-0.004}$	768.5	608
		$n_2 = 4.70^{+1.47}_{-1.15} \times 10^{-4}$		
Power Law & Blackbody II	8.26×10^{-3}	kT=$0.328^{+0.013}_{-0.014}$	686.7	607
		$n_2 = 15.8^{+2.8}_{-2.8}$		
Power Law & Blackbody III	8.06×10^{-3}	kT=$0.57^{+0.03}_{-0.03}$	693.0	608
		$n_2 = 1.39$		
Power Law & Blackbody IV	8.03×10^{-3}	$\dot{m} = 0.11^{+0.05}_{-0.03}$	710.4	608
		$\alpha = 6.63$		
		$n_2 = 2.39 \times 10^{-3}$		
Power Law & Blackbody V	8.97×10^{-3}	$\dot{m} = 10$	806.2	608
		$\alpha = 6.63$		
		$n_2 = 0$		
Power Law & Disk	8.06×10^{-3}	$\dot{m} = 5.5^{+3.0}_{-2.1} \times 10^{-2}$	694.1	608
		$n_2 = 3.39 \times 10^{-3}$		

Table 4.3: Soft X-ray Continuum Models for Ark. 120. n_1 is the normalization of the first powerlaw continuum; n_2 the normalization of the other components of the model.

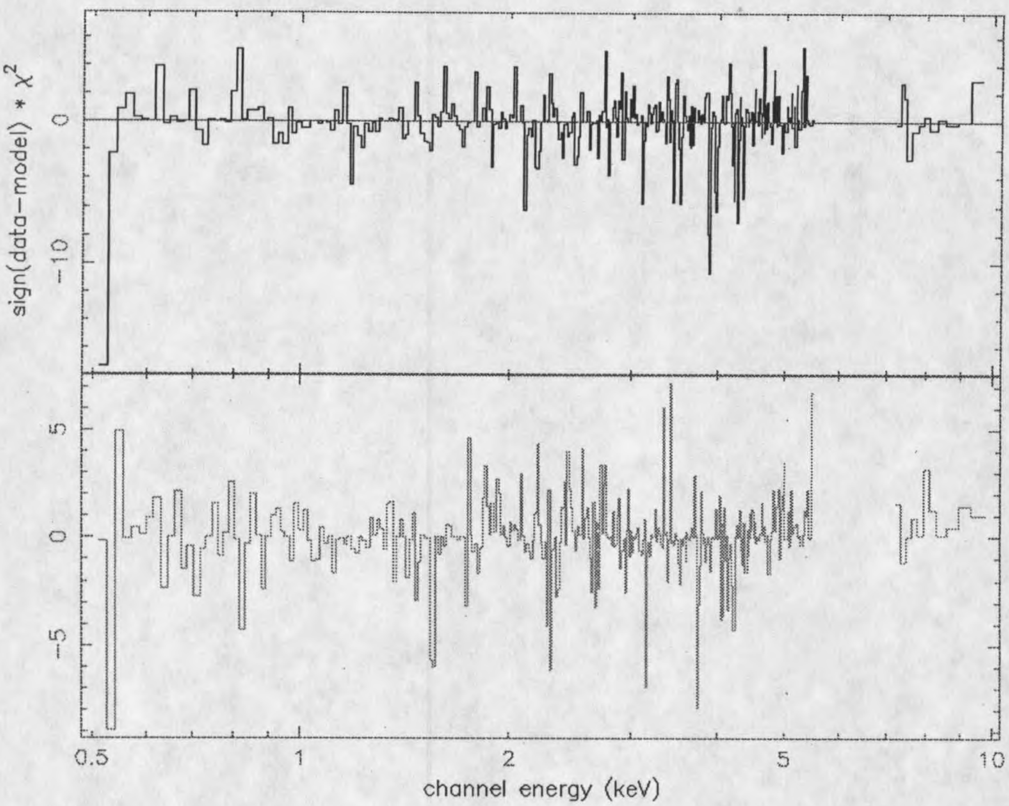

Figure 4.10: χ^2 deviation of soft X-rays from Power law and Blackbody I Model

law, double power law, and more complicated blackbody models. All of the χ^2 spectra show several common features: a soft energy excess at 0.5 keV, a reflection hump beginning just below 10 keV, a narrow excess (most likely an emission line) just above 0.6 keV, and two absorption features near 0.71 keV and 0.86 keV. These features are typified in Figure 4.10, which shows the χ^2 deviation of the data from the model for the Power Law & Blackbody I continuum model.

In order to best fit the soft energy data, we adopt the three best-fitting soft energy continuum models and the best-fitting high-energy continuum model (XSPEC

Model Component	Value
Power law	$A_1 = 8.34^{+0.09}_{-0.09} \times 10^{-3}$
Blackbody	$A_2 = 3.31^{+0.33}_{-0.33} \times 10^{-5}$
Blackbody	$kT = 0.28$
Edge 1	$\tau = 0^{+0.11}$
Edge 2	$\tau = 0.33^{+0.20}_{-0.18}$
Gaussian	$\varepsilon = 0.596$
Gaussian	$\sigma = 0.02 \pm 0.02$
Gaussian	n=$1.56^{+0.75}_{-0.75} \times 10^{-4}$
	$\chi^2 = 677.2$
	d.o.f. =608

Table 4.4: A_1 and A_2 are the normalizations of the primary power law and blackbody, respectively. kT represents the temperature of the blackbody in keV. Edge 1 is an absorption edge with energy corresponding to O VII absorption; Edge 2 is an absorption edge with energy corresponding to O VIII. The edge energies were constrained to prevent overlap with the gaussian near 0.6 keV, so the energies are not presented. The Gaussian is a gaussian line profile, which corresponds to emission from ionized oxygen.

model pexrav) to fit the low-energy end of the reflection hump. We also fit the three spectral features of interest, which, if present, will correspond to oxygen emission and absorption.

The parameters of the best fit to the composite power law-blackbody model are shown in Table 4.4 This model shows the presence of O VIII to 90% confidence, which would suggest that Arkarian 120 has a warm absorber in addition to a low energy continuum component. The fitting statistic is not ideal, but from Figure 4.10 it is clear that much of the discrepancy comes from the reflection hump above 8 keV, which has not been accurately fit in this model. The large deviations between 2 and 5 keV are not well correlated between the SIS0 and SIS1 detectors, suggesting that counting statistics, rather than the physics of the object, are responsible. The

Model Component	Value
Power law	$A_1 = 7.83 \times 10^{-3}$
Blackbody	$A_2 = 3.13 \times 10^{-5}$
Blackbody	$kT = 0.28$
Edge 1	$\tau = 0^{+0.11}$
Edge 2	$\tau = 0^{+0.04}$
Gaussian	$\varepsilon = 0.628$
Gaussian	$\sigma = 0.02$
Gaussian	n=5.01 $\times 10^{-5}$
$\chi^2 = 753.2$ d.o.f.=604	

Table 4.5: A_1 and A_2 are the normalizations of the primary power law and bremsstrahlung components, respectively. kT represents the temperature of the bremsstrahlung electrons in keV. Edge 1 is an absorption edge with energy corresponding to O VII absorption; Edge 2 is an absorption edge with energy corresponding to O VIII. The edge energies were constrained to prevent overlap with the gaussian near 0.6 keV, so the energies are not presented. The Gaussian is a gaussian line profile, which corresponds to emission from ionized oxygen.

fitting statistic is considerably improved from its value without the warm absorbing components, further indicating the likelihood of its presence.

The parameters from the composite bremsstrahlung and power law model with a warm absorber are shown in Table 4.5. There can be little argument that the bremsstrahlung plus power law model does not have as compelling a fitting statistic as does the bremsstrahlung plus blackbody model, and is actually a worse fit than a model with bremsstrahlung alone. If bremsstrahlung is responsible for the soft energy excess, the warm absorber (if present) does not contain nearly as much material as if the soft energy excess is caused by blackbody emission.

Conclusion

While Arkarian 120 does not vary dramatically, its light curve is not inconsistent with variable luminosity. Moreover, several of the primary hardness ratios show a high probability of variation which is not simply correlated to the source luminosity. This short observation is not adequate to extract separate spectra according to the luminosity and hardness parameters, but a longer ASCA observation or an RXTE observation would be extremely interesting in that light.

The hard X-ray continuum includes the low energy end of a Compton Reflection hump previously seen in the GINGA observation of this source (Nandra, 1991). A simple power law model fits the data adequately, and produces a slope statistically consistent with those of Nandra, but the most likely continuum model is reflection from an ionized medium.

The soft X-ray portion of the spectrum shows strong evidence of a second continuum component, as previously found in ROSAT observations of the source (Brandt *et. al*, 1993). The fitting statistics allow us to rule out the double power law as a feasible continuum model, but we cannot distinguish between a simple blackbody, a disk model, and thermal bremsstrahlung as secondary models of the continuum. If we accept a blackbody component as part of the soft energy continuum, there is substantial evidence of a warm absorber in Arkarian 120. The warm absorption was not measured in the previous ROSAT observation because ROSAT's lower spectral resolution was unable to distinguish the blackbody component from the embedded warm absorber..

The ASCA observation of Arkarian 120 thus presents an improved picture of its structure: this galaxy has a central engine consisting of a cold disk orbiting a black hole of indeterminate spin parameters. The cold disk is surrounded by a hot corona, evident from the compton reflection of the corona off the disk, as well as the presence of Kα fluorescence. In addition, the galaxy has a blackbody component with a temperature near 10^6 K, which almost certainly comes from the disk itself. The disk is likely surrounded by a warm absorber, as indicated by the presence of O VIII absorption and an emission line near 0.6 keV.

CHAPTER 5

X-RAY ANALYSIS OF MCG-6-30-15

Un coup de des n'oblitera le hasard.

Stéphane Mallarmé, **Un Coup de Des** [1]

Introduction

X-rays from the galaxy MCG-6-30-15 were first discovered by Pineda in 1978 using the SAS 3 X-ray observatory, and was later identified as a Seyfert 1 galaxy from optical observations (Pineda, 1980). EXOSAT observations of this source first showed the presence of an iron Kα emission line and a cold reflection hump above 10 keV thought to be from reflection from the inner accretion disk. This was confirmed in a subsequent GINGA observation (Nandra, Pounds, and Stewart, 1989; Matsuoka *et. al.* 1990); also, evidence of an ionized absorber was inferred by the shape of the iron Kα line. The galaxy was also analyzed by ROSAT's Positional Sensitive Proportional Counter (PSPC) in 1992 (Nandra and Pounds, 1992); the analysis of this observation first revealed evidence for an absorption edge near 0.8 keV; which

[1]trans: A toss of the dice does not eliminate chance. Stéphane Mallarmé, A Roll of the Dice

is consistent with a low-resolution spectrum of O VII and O VIII K-shell absorption edges.

This object has been studied over many wavelengths; a recent study by Reynolds *et. al.* (1997) included analysis of Hubble observation, which demonstrated that the galaxy was of class S0, analysis by the Anglo Australian Telescope, which showed strong extinction due to interstellar dust, and by the International Ultraviolet Explorer (IUE), which showed an extremely high flux ratio of CIV/Hβ. This was explained as the result of scattering from the same material which causes the extinction observed at lower wavelengths, and is consistent with a scattering fraction of 1-5% . In addition, previous observations by the Infrared Astronomy Satellite (IRAS) showed that the shape of the IR bump is consistent with thermal emission from a dusty warm absorber only if the composition of the gas is not solar.

The source was observed twice during the performance verification (PV) phase by ASCA in 1993; these observations were the first to resolve the O VII and O VIII K-shell edges, and also the first to detect a skewed line shape for the Fe Kα emission line (Fabian *et. al.*, 1994). In addition, the optical depth of the O VIII K-shell absorption edge varied between the two observations; the first observation, performed July 8–9 1993, had τ_{OVIII} = 0.19$\pm$0.03, while the second observation, performed July 31–August 1 1993 had τ_{OVIII} = 0.44$\pm$0.04 (Reynolds *et. al.*, 1995).

A long ASCA observation of MCG-6-30-15 in 1994 provided data for a series of dramatic findings. At that time, the observation provided the highest quality data for the iron Kα line; the initial analysis showed that the line was similar to that expected from a Schwarzschild black hole, but not entirely consistent (Tanaka *et. al.* 1995) and the second analysis that the iron line was completely consistent with Kerr and varied over the course of the observation (Iwasawa *et. al.* 1996). The 1994 observation also provided material for extensive studies of the warm absorber. The first analysis showed variation in the warm absorber; Otani *et. al.* (1995) found that the O VIII changed significantly over the course of the observation but that the O VII did not, and concluded that the two must be located in spatially distinct regions of the AGN. Similar methods were used in another analysis (Reynolds 1996), in which some O VII variation was found. Since then, another long ASCA observation has been performed, but the radiation damage to the SIS detectors precluded using it to further study the warm absorber.

In this chapter, the 1994 observation of MCG-6-30-15 is reanalyzed by sorting the light curve into spectra in two different manners: first, by dynamical state and second using both hardness and luminosity as filters. We do not extend this analysis to include the more recent ASCA observation of MCG-6-30-15 because of the increased effects of the Residual Dark Distribution (RDD) due to radiation damage (see, e.g. Chiang *et. al.* 2000); these make ASCA observations after 1996 unreliable below 1 keV. Thus, such observations cannot be used alone to make predictions about the warm absorber region. In section 5.2, criteria for data analysis are summarized. Section 5.3 presents timing analysis of this observation. Section 5.4 describes the selection methods as applied to this particular source; it is supplemented by the material in Appendix E. Spectral analysis of the full and newly selected data are presented in Section 5.5, and concluding remarks exist in Section 5.6. The analyses presented in Sections 5.2–5.5 are supplemented by Appendix B; the fitting parameters for luminosity and temporal filters (published elsewhere) are shown in Appendices C and D respectively.

Data Extraction and Image Analysis

In 1994, MCG-6-30-15 was observed by ASCA from July 23 to July 27; the principal investigator was Dr. Hajime Inoue. Data was obtained at HIGH, MEDIUM, and LOW telemetry rates; the entire 1 CCD mode observation was performed in FAINT mode and subsequently converted to BRIGHT2 mode. The data were extracted using XSELECT version. 1.3 with a cutoff rigidity of 6 GeV/c^2; data obtained during passage through the South Atlantic Anomaly (SAA) were excluded. The field of view of ASCA contains no other X-ray sources, although an F star located in our own galaxy contributes in other wavelength regimes (Pineda, 1980). The SIS data were extracted from a region 4.3 arc minutes in diameter and, because the source is in a relatively high background region of the sky, a near sky background subtraction with radius 1.7 minutes of arc was made. Due to vignetting, the GIS detectors use a blank sky background; the source region was 8 arc minutes. The interested reader may refer to Appendix B for more details.

Timing Analysis

The light curve of this source was first analyzed in the manner described in Chapter 3; the light curve is shown in Figure 5.1. The interested reader may find plots of each of the hardness ratios against time in Appendix B. This observation of MCG-

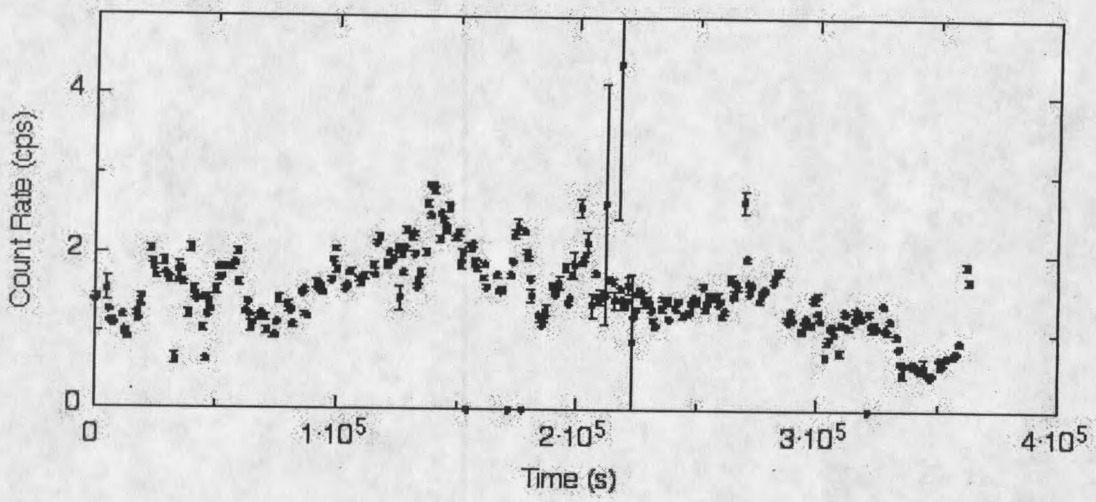

Figure 5.1: The total count rate of MCG-6-30-15 from all four detectors over the 365 ks observation.

6-30-15 varies extremely rapidly; the peaks are overlapping and not easily resolved into individual flares. Two prominent features occur in the 360 ks observation; a bright flare near the middle of the observation and a deep minimum near the end of the observation. Near the bright flare the luminosity varies rapidly, but during the deep minimum the low luminosity remains almost constant and varies very little. The primary statistics of the total light curve (Table 5.1) show that the variation is statistically significant. Variation in the hardness ratios is also apparent; R_2 in particular varies rapidly, except during the deep well at the end of the observation, as shown in Figure 5.2. During the deep well, R_2 does not vary as much as elsewhere in the observation, but has a value substantially higher than earlier epochs, suggesting an increased column density for the warm absorber.

A plot of the counts from 3–5 keV plotted against the counts from 7.5–10 keV

	CPS	R_2
Average	1.468	0.488
Standard Deviation	0.520	0.205
Minimum	0	0.111
Maximum	4.4	0.328
χ^2 probability of constancy	0	0
KS probability of constancy	0	0

Table 5.1: Statistical properties of the light curve of MCG-6-30-15. The values of both the χ^2 and Kolmogorov-Smirnov (KS) tests indicate probabilities of constancy of less than 10^{-38}. Count rates are in units of counts per second (CPS); hardness ratios are dimensionless.

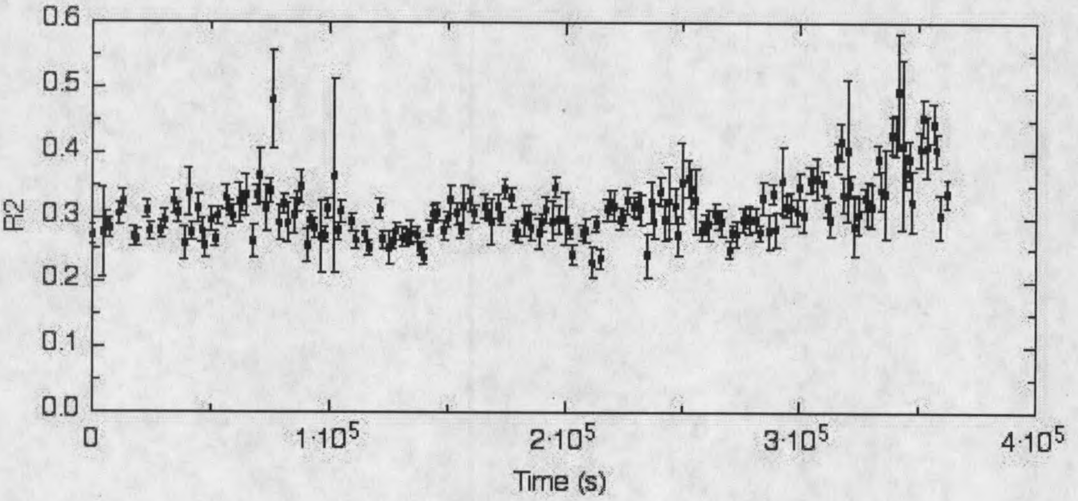

Figure 5.2: Hardness ratio R_2 versus time. This particular graph is made using only counts from the two SIS detectors; the interested reader may find the corresponding plot for the GIS detectors in Appendix B.

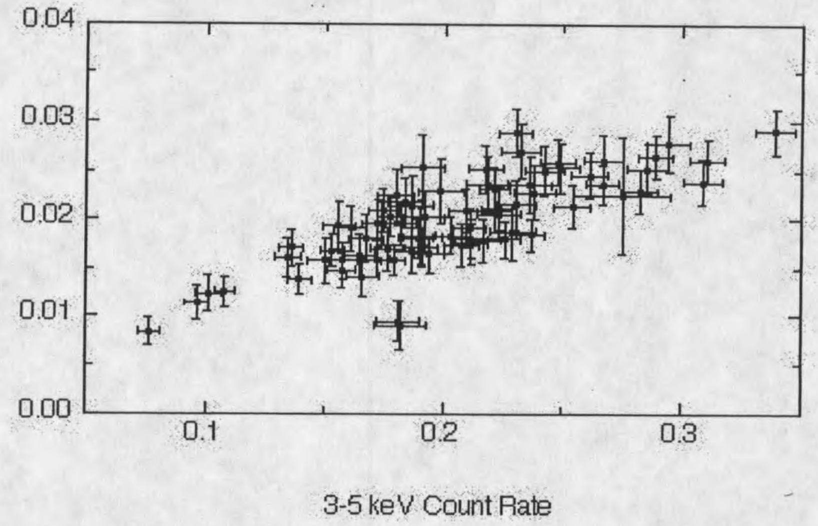

Figure 5.3: Counts 3–5 keV plotted against Counts 7.5–10 keV. The deviations from constant slope suggests that the photon index changes for low luminosities.

gives a qualitative estimate of the photon index. The bins in Figure 5.3 are nearly linear, although several hard count rates are associated with more than one medium count rate. While this indicates that more than one photon index may exist for the observation, the proximity to linearity of the points also suggests that the variation in photon index will not be great.

A plot of the hardness ratio R_2 vs. R_3 is even farther from linear; many values of R_2 exist for a single value of R_3 as shown in Figure 5.5. A rough relationship between the hardness ratios certainly exists; higher R_3 (softer power law) is associated with a slightly higher R_2 (less absorption by the warm absorber). However, a wide scatter of values of R_2 exists for any value of R_3. Part of this variation is associated with the deep minimum at the end of the observation, but earlier variation is not well-correlated with either time or luminosity. Spectral selection using only time and

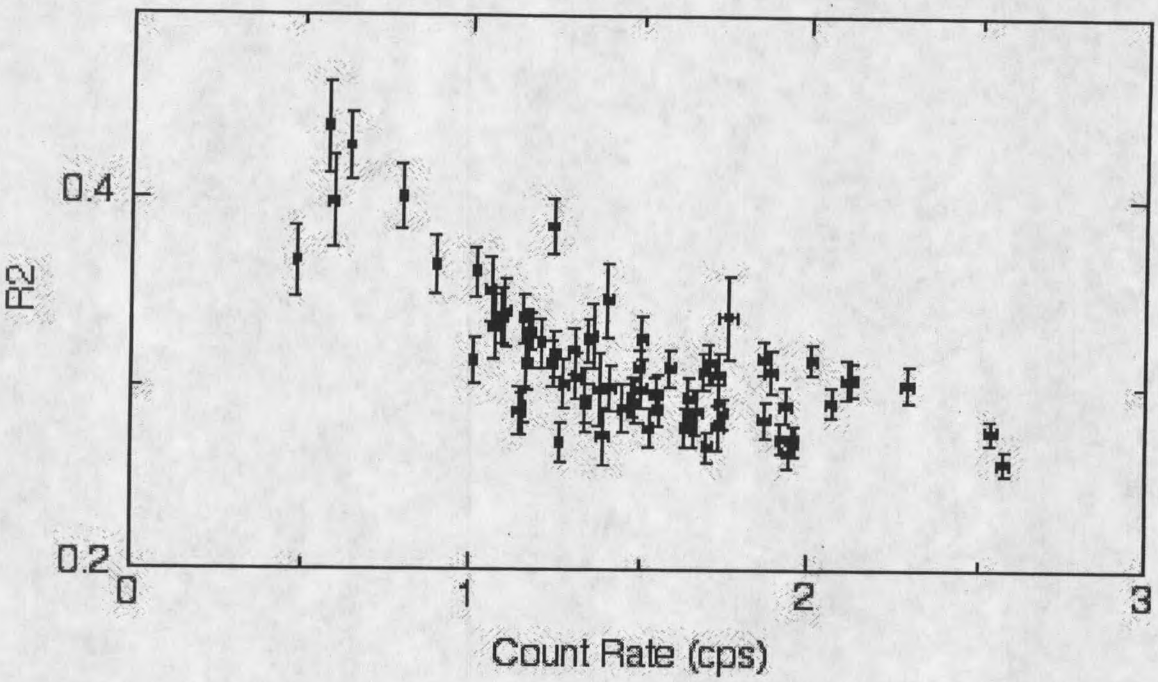

Figure 5.4: Hardness ratio R_2 plotted against Count Rate for 5 ks bins of the light curve.

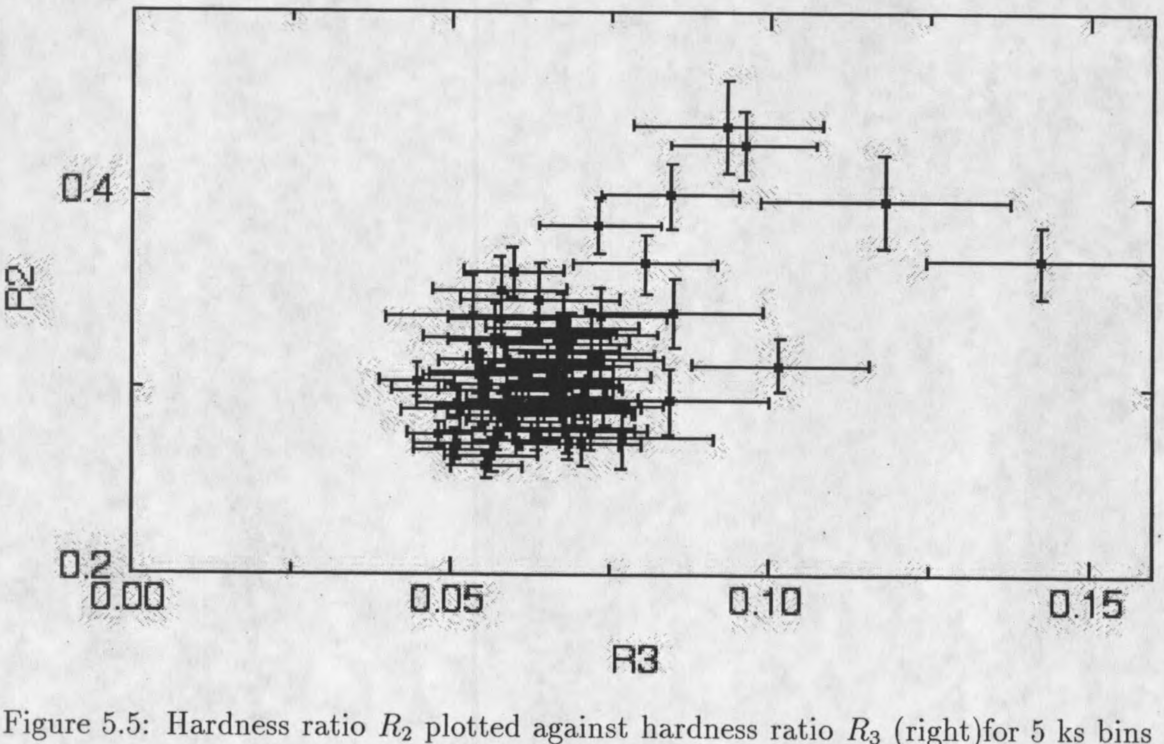

Figure 5.5: Hardness ratio R_2 plotted against hardness ratio R_3 (right)for 5 ks bins of the light curve.

luminosity filters thus has the potential to miss variation in the warm absorber.

Selection of Data Sets

This observation has already been analyzed by several other researchers, including Otani *et. al.* (1994), Reynolds *et. al.*(1995) and Iwasawa *et. al.* (1996). There are two main differences between this work and others: first, we use slightly more conservative techniques of spectral fitting, and second, we use new selection criteria to group points of the light curve with similar physics into spectra. To demonstrate that the results presented here are the result of the selection criteria, and not of the fitting technique, the analysis of the spectrum of the full 1994 observation is presented in this chapter, and analyses of spectra selected with temporal and luminosity filters are presented in Appendices C and D respectively. Selection with temporal filters is hereafter called Method A, while selection with luminosity filters is designated as Method B, to quickly distinguish them from the new selection methods presented here.

Selection by Luminosity Derivative

The long exposure of this observation allows subdivision of the luminosity derivative states into more classes than were described in Chapter 3. The state *Constant* still describes points which are within error of the two adjacent bins of the light curve, but other bins within the light curve are subdivided according to whether the change exceeds a threshold value α. The remaining nine states are illustrated in Figure 5.6. This spectral selection technique will hereafter be referred to as Method C. The

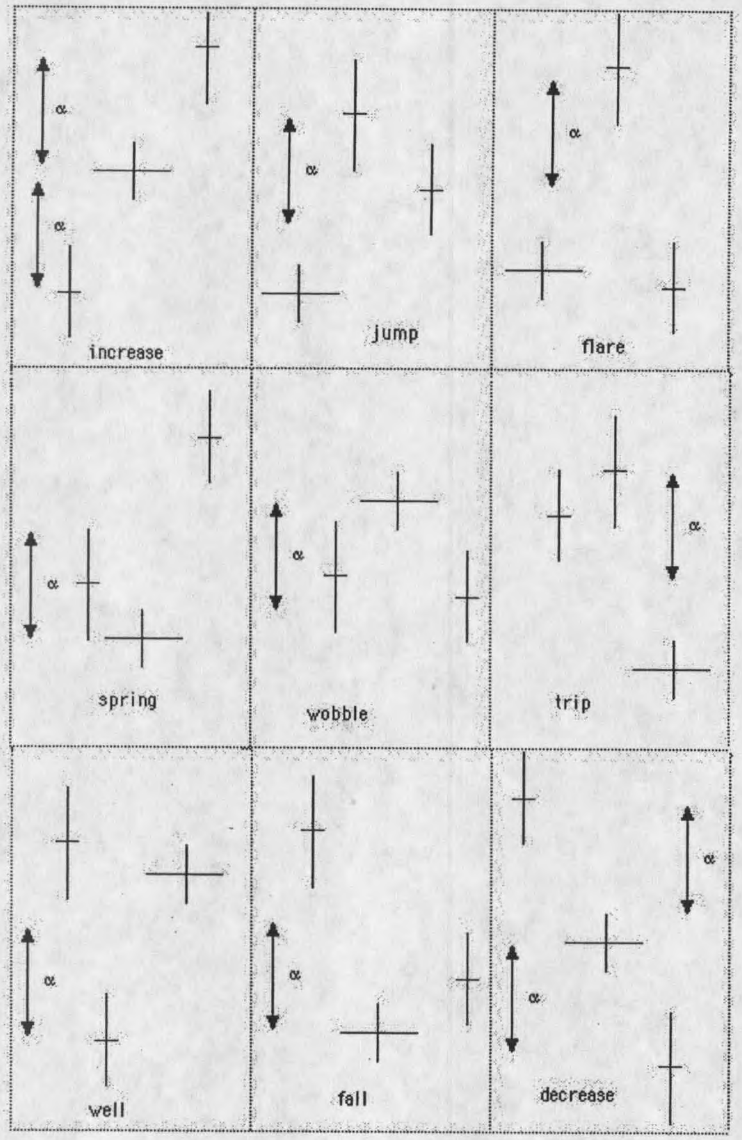

Figure 5.6: The classification by second derivative is expanded from four to nine subsets for the long exposure observation of MCG-6-30-15.

Data Set	Exposure(sec)	SIS0 counts	Count rate
Constant	16,353	31,214	1.91
Increase	16,353	31,214	2.14
Decrease	17,261	37,041	2.15
Flare	17,074	36,745	2.68
Well	13,580	28,512	2.10
Jump	16,692	34,927	2.09
Fall	15,891	32,237	2.03
Spring	16,053	33,603	2.09
Trip	14,467	28,602	1.98
Wobble	9,323	14,696	1.61

Table 5.2: Characteristics of Spectra Chosen by 3-point Derivative for MCG-6-30-15.

states *Flare*, *Well*, *Increase*, and *Decrease* are as described in Chapter 3 with the additional requirement that the difference in luminosities of adjacent points exceed the parameter α; the others are self-explanatory from Figure 5.6. Several values of α were used, and basic analysis performed on the resultant spectra, until a value of α which produced a roughly equitable distribution across states was obtained. The characteristics of the final spectra are summarized in Table 5.2. One striking point from the data sets themselves is that points classified as constant and wobble, rather than points described as wells, have the lowest count rates. This reflects the fact that during the deep minimum at the end of the observation, only the very beginning and end of the epoch have rapid variation, and the very low luminosity points in between these changes show little variation.

Selection by R_2 and Luminosity

In section 5.2, the timing analysis for these data showed that count rate and R_2 vary significantly and independently, while the other hardness ratios have less variation

A	C> 1.73 cps	1	$R_2 > 0.5$
B	$1.73cps > C > 1.47$cps	2	$0.5 > R_2 > 0.44$
C	$1.47cps > C > 1.21$cps	3	$0.44 > R_2 < 0.4$
D	C< 1.27cps	4	$, R_2 < 0.4$

Table 5.3: Cutoff values for Count Rate and R_2 for classification of MCG-6-30-15.

and are not independent of the continuum. This is suggestive of the variation with state seen in galactic black holes (DiMatteo *et. al.*, 1998), which show different hardness ratios at the same luminosity, depending upon which state they are in (e.g. decreasing or increasing). Thus, we use the hardness ratio R_2 as a second dimension to sort the data into spectra. Each bin in the light curve classified both by luminosity and by hardness ratio R_2, as shown in Table 5.3. This method of spectral selection will hereafter be referred to as Method D.

Thus, each point was associated with both a luminosity and a hardness ratio classification, so that a point with luminosity more than one standard deviation above the mean and a hardness ratio less than one standard deviation below the mean would receive the classification *A3*, where the letter represents the luminosity classification and the number the hardness classification. This created 16 separate classes of points within the observation; of these, 14 spectra were created, as classifications *A1* and *B1* were combined, and *D3* and *D4* combined; to ensure that each spectrum had a minimum of 8500 total counts. The characteristics of these spectra are described in Table 5.4. The cutoff for the count rate and hardness ratio are based on the light curve statistics; in each case, the mean and 0.5σ deviations were used as cutoff points.

Across luminosity classifications A-C, there is not a significant variation in the

Data Set	Exposure	SIS0 Counts	Count Rate
AB1	3,583	8,999	2.51
A2	11,132	31,855	2.86
A3	15,545	44,535	2.86
A4	11,876	34,697	2.92
B2	10,148	23,094	2.28
B3	13,242	29,388	2.22
B4	9,796	22,027	2.25
C1	5,189	10,030	1.93
C2	14,301	27,603	1.93
C3	10,670	20,739	1.94
C4	4,486	8,648	1.93
D1	22,124	26,997	1.22
D2	9,330	14,001	1.50
D34	10,087	15,074	1.49

Table 5.4: Here the characteristics of spectra selected by combined luminosity and hardness, are shown.

count rate of the spectra with the same luminosity classification. In contrast, the count rate for data set D1 (which contains most points from the deep minimum) has significantly lower luminosity than D2 and D34, which correspond roughly to local minima in earlier parts of the observation. The spectra selected by luminosity and hardness had no *a priori* association with particular phenomenologies of the dynamics.

Table 5.5 shows the rough correlation between these data sets and phenomenology; the interested reader can refer to Appendix E, which shows each bin in the light curve with its classification using both methods developed as part of this work. As one might expect, most local maxima have high luminosity and most local minima have low luminosity. The deep minimum at the end of the observation hosts far more high hardness, low luminosity (D1) states than elsewhere in the observation. The rest of the extremely low luminosity states occur earlier in the observation; states

Data Set	Phenomenology
AB1	peaks of small-amplitude flares after 160 ks
A2	high luminosity, relatively stable points
A3	before bright flare, some peaks of large-amplitude flares
A4	before bright flare, other peaks of large-amplitude flares
B2	relatively stable bins
B3	before bright flare, some peaks of low-amplitude flares before 160 ks
B4	before bright flare, other peaks of low-amplitude flare before 160 ks
C1	surrounding/peaks of small flares after 160 ks
C2	decreases after small-amplitude flares
C3	relatively stable bins
C4	low amplitude quiescent states
D1	deep minimum, small-amplitude local minima
D2	small-amplitude local minima
D34	first 20 ks of observation, large-amplitude local minima

Table 5.5: Primary Phenomenologies Associated with each new state.

classified as *D2* are located throughout the observation, with 66 percent of the counts occurring before 300 ks. Only about 10 percent of the low hardness, extremely low luminosity bins are located in the deep minimum; bins classified as *D34* are associated mostly with the first 20 ks of the observation and local minima occurring prior to the deep minimum. Some high luminosity states are also correlated to phenomenology; of the local maxima in the observation, 54 percent are classified as *A4* or *B4*, and another 23 percent are classified as *A3* or *B3*. Thus high luminosity, low hardness states are associated with the peaks of the flares during the observation; the strong exception is that the remainder of the *A2* and *A3* states are associated with the bright flare between 120 and 140 ks. However, if we classified this region as one of rapidly overlapping, strong flares, the phenomenology would still be consistent. The somewhat dimmer low hardness *B3* and *B4* states are concentrated just prior to the very bright flare at 140 ks, just prior to the flare near 200 ks, in regions associated

Model	Photon Index	Other Parameter(s)	χ^2	d.o.f.
Single Power law	$\Gamma = 1.86 \pm 0.04$		607.0	663
Broken Power law	$\Gamma_1 = 1.78^{+0.06}_{-0.08}$ $\Gamma_2 = 2.28 \pm 0.04$	$\varepsilon_{break} = 5.44^{+1.43}_{-0.87}$	586.8	661
Absorption by Dust	$\Gamma = 1.68 \pm 0.04$	$\alpha_{dust} = 0.14^{+0.12}_{-0.13}$	607.0	662
Partial Absorption by Gas	$\Gamma = 1.86 \pm 0.04$	$N_h = 0.5$	698	662
Neutral Reflection	$\Gamma = 2.28 \pm 0.04$	$\epsilon = 6.2 \pm 0.7$	582	662
Ionized Reflection	$\Gamma = 2.13 \pm 0.04$	$\xi = 0.014^{+0.012}_{-0.014}$ $\epsilon = 3.4^{+0.5}_{-0.5}$	586	661

Table 5.6: Best-fit parameters for six possible continuum shapes. Reflection models are fit with $\theta = 30$. Confidence limits given are 3σ.

with smaller flares between 210 and 240 ks, and just prior to the flare at 270 ks. These states are then precursors to large flares and peaks of small ones in the more luminous portions of the observation. The interested reader may find an illustration of how each point in the light curve is classified in Appendix E.

Spectral Analysis

Hard Continuum

The iron line for MCG-6-30-15 is unusually broad (Iwasawa *et. al.*, 1998) and must be excluded from continuum models which do not include ionized reflection. Figure 5.7 shows the iron line, roughly fit to a double gaussian profile. From this line shape, it is evident that most of the iron line can be eliminated if the 4.5–7.2 keV window is excluded from the analysis. With this window excluded, the available power law models were fit to spectra of the full observation with results as shown in Table 5.6.

The results for the single power law are in good agreement with previous analyses of this observation (e.g. Iwasawa *et. al*, 1996). The broken power law fits well,

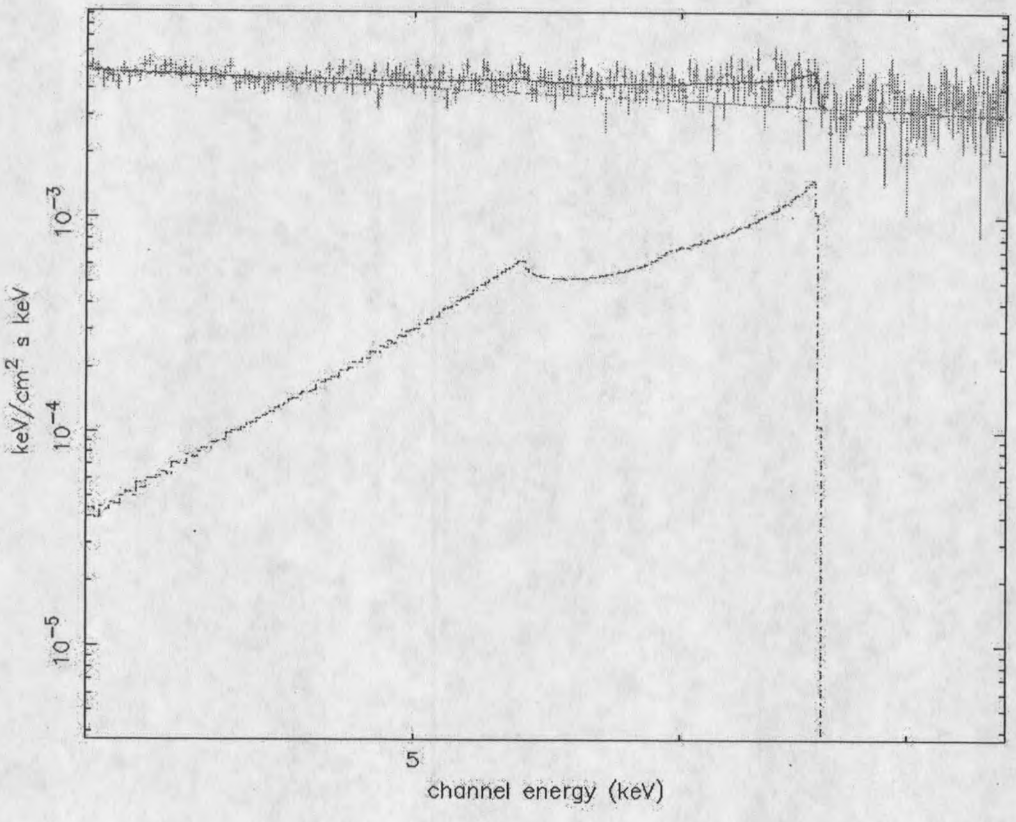

Figure 5.7: Fe Kα fluorescence line in MCG-6-30-15, in this case fit to a double gaussian profile. This particular graph illustrates that the broad iron line has significant counts from about 4.5 keV to the iron absorption edge near 7.2 keV.

but the break energy is almost exactly centered on the Fe Kα emission line energy, suggesting that it may be an artifact of excluding the iron line region. Physically, the only parameter of interest is the lower limit on the absorption by dust, which indicates a small amount of dust may or may not be present. The fitting statistics from the reflection models is better, but no more so than the broken power law; this suggests that a reflected component is probably present. The increase in photon index, though, suggests that the relative reflection is overestimated due to its interaction with the photon index, which is significantly higher for these data than for the simple power law model. All models except absorption by gas fit the data acceptably. Nonetheless, the fitting statistics and increased relative reflection of the ionized and neutral reflection models suggest that this, rather than absorption by gas or dust, is the most likely physical process in the continuum of this source.

Table 5.7 shows the best-fit photon indices of the data sets selected using Method C (luminosity derivatives). All are within statistical error of the average photon index of Γ=1.87. Only one data set has unacceptable fitting statistics- despite having adequate counting statistics the data sets *spring* and *trip* do not have adequate fitting statistics.

The best-fit parameters for the simple power law model for the data set selected by combined luminosity and hardness criteria (Method D) are shown in Table 5.8. The photon index does not change significantly from one data set to another; all data sets are consistent with the photon index of the entire observation.

All data sets in Table 5.8 are consistent with a photon index of 1.87 to within

Data Set	Photon Index	χ^2	d.o.f.
con	$2.03^{+0.17}_{-0.15}$	210.0	219
decrease	$1.91^{+0.16}_{-0.15}$	183.2	231
fall	$2.08^{+0.18}_{-0.16}$	190.2	212
flare	$2.09^{+0.17}_{-0.15}$	225.6	217
increase	$1.95^{+0.16}_{-0.15}$	200.6	214
jump	$1.97^{+0.15}_{-0.14}$	241.3	242
spring	$2.02^{+0.18}_{-0.17}$	186.0	184
trip	$1.91^{+0.21}_{-0.19}$	182.2	140
well	$2.05^{+0.21}_{-0.19}$	153.6	153
wobble	$1.94^{+0.25}_{-0.23}$	102.7	116

Table 5.7: The best-fit parameters from the simple power law model are shown for the spectra selected using luminosity derivatives. Errors shown are 3σ.

Data Set	Γ	χ^2	d.o.f.
ab1	$2.07^{+0.25}_{-0.22}$	117.3	119
a2	$2.13^{+0.19}_{-0.17}$	155.9	204
a3	$2.03^{+0.18}_{-0.16}$	233.5	233
a4	$2.15^{+0.24}_{-0.22}$	159.0	154
b2	$1.82^{+0.21}_{-0.19}$	168.0	163
b3	$1.94^{+0.22}_{-0.19}$	162.7	165
b4	$1.78^{+0.29}_{-0.26}$	87.57	117
c1	$2.09^{+0.32}_{-0.27}$	84.91	99
c2	$1.94^{+0.24}_{-0.21}$	94.78	146
c3	$2.11^{+0.31}_{-0.27}$	124.8	121
c4	$1.90^{+0.62}_{-0.46}$	26.78	77
d1	$1.83^{+0.17}_{-0.16}$	208.6	206
d1a	$1.75^{+0.24}_{-0.21}$	103.4	119
d1b	$1.80^{+0.30}_{-0.26}$	116.3	101
d2	$2.01^{+0.34}_{-0.29}$	100.1	94
d34	$1.90^{+0.35}_{-0.29}$	105.5	88

Table 5.8: Simple powerlaw fits to Method D datasets

statistical error. However, three data sets (d1b, d2, and d34) have slightly less compelling fitting statistics than the others. The fits of the other continuum models show a similar lack of variation across data sets selected by either method, and, as with the continuum for the full observation, the reflection models fit the data better. The interested reader can find these data in Appendix B; to summarize, the fitting statistics for each of the models vary minimally. The broken power law model consistently has the best fitting statistics for those data sets which have $\chi^2/dof > 1$ and is usually one of the two worst-fitting models for other data sets; from this, one can conclude that a broken power law is probably may not be the best representation of the data sets overall. As this is the only model with no basis in a model of the AGN environment, this finding is reassuring. Between 22% and 80% of the data sets within any particular grouping method show evidence for absorption by dust, as does the average spectrum of the observation.

The Warm Absorber

Before analyzing the warm absorber of the complete observation, a value for the neutral hydrogen column is needed. A lower limit on the amount of neutral hydrogen is obtained from the 21 cm observations of Galactic hydrogen (Elvis, Lockman, and Wilkes, 1989) which obtained a value of 4.1x$10^{20} cm^2$. The multiwavelength analysis of Reynolds *et. al.* (1997) also places a constraint on this value; if the ratio of cold gas to dust is the same as for our own galaxy, the neutral hydrogen column should be in the range 2.6–4.4 x$10^{21} cm^{-2}$. Previous observations have either fixed the value at $4.1x10^{20} cm^2$ (Iwasawa *et. al.* 1996, Tanaka *et. al.* 1995) or allowed the value to vary provided that it remains above this value (Otani *et. al.* 1995, Reynolds *et. al.* 1997, Reynolds 1996). We choose the first approach because it allows us to analyze variations of the warm absorber on timescales shorter than the light-crossing time for a photon travelling from the central engine to the closest conceivable neutral hydrogen, and note that this timescale is far longer than the 20 ks data sets used by previous observers.

With the photon index fixed to 1.88 in accordance with the hard X-ray analysis and the neutral hydrogen column fixed at $4.1x10^{20} cm^2$, the two oxygen edges were fit. The results are as shown in Table 5.9. These energies of these lines are in excellent agreement with previous analyses (Otani *et. al.* 1994; Reynolds 1995), as is the optical depth of O VIII. This method of analysis does, however, give a different value of τ_{O7} than previous analyses; the reason for this is that this analysis results from fixed values of neutral hydrogen and photon index. The value is significantly higher than that of Reynolds (1995), who found $\tau_{O7} = 0.64 \pm 0.02$ for $\Gamma = 1.90^{+0.01}_{-0.02}$ and $N_h = 5.3 \pm 0.3x10^{20} cm^2$, and much higher than that of Otani *et. al.* (1994) who found $\tau_{O7} = 0.58 \pm 0.04$ for $\Gamma = 1.84 \pm 0.01$ and N_h=$4.1x10^{20} cm^2$. The difference from Reynolds value is small, and is due to the different method of fitting neutral hydrogen. The difference from Otani's value is larger because his method of fitting the photon index involves simultaneously fitting the photon index, neutral hydrogen, and oxygen edges to the SIS detectors with all counts above 2 keV excluded and no background subtraction. Our statistical fit is superior to either that of Reynolds

Parameter	Value
O VIII	$\varepsilon = 0.880^{+0.014}_{-0.022}$
	$\tau = 0.178 \pm 0.020$
O VII	$\varepsilon = 0.717^{+0.003}_{-0.004}$
	$\tau = 0.723 \pm 0.026$
$\chi^2/d.o.f.$	1.326

Table 5.9: Average Values of the Oxygen Edges of the Entire Observation; confidence regions shown are 3σ limits.

($\chi^2/d.o.f. = 1601/1008$) or Otani ($\chi^2/d.o.f. = 994.6/513$) for the same model; their results were easily reproduced when their methods were used.

Next we explore the possibility that the properties of the warm absorber change with dynamical state by analyzing the data obtained using the derivate sorting method. Figure 5.8 shows the variation in the O VIII edge depth plotted against the variation in the O VII edge depth. The physical significance of this variation is that the *well* state has significantly lower optical depths for O VII and O VIII than two other states (*constant,trip*). Examination of the point-by-point classification in Appendix E shows that few of the timing bins classified as *well* are located in the deep minimum at the end of the observation; rather, they are located throughout the rest of the observation, and generally correspond to local minima, as one would expect. As with previous analyses, these data sets show no significant variation in the energy of the two oxygen edges, and the goodness-of-fit of the data sets is acceptable.

We can further confirm the strongest variation, between the *well* and *constant* states, by taking a ratio of the two spectra using the recently developed ftool mathpha.

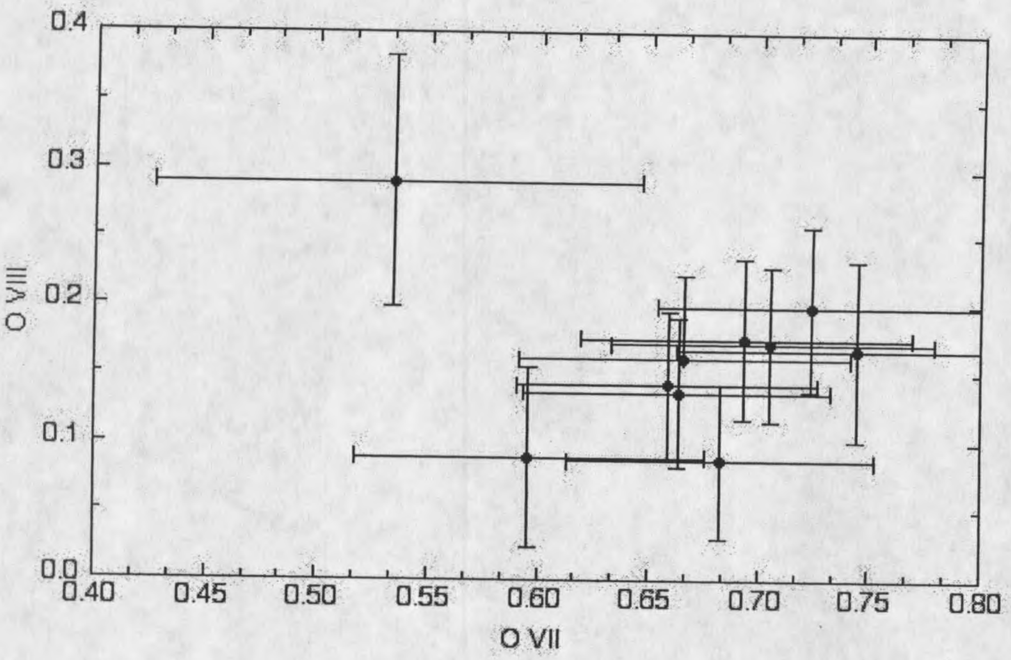

Figure 5.8: O VIII Optical Depth as measured for Method C spectra. Error bars represent 3σ confidence limits.

The ratio of the two spectra is defined by:

$$r_{AB}(\varepsilon_i) = \frac{A(\varepsilon_i)}{B(\varepsilon_i)} \tag{5.1}$$

where $A(\varepsilon)$ is the first spectrum of interest and $A(\varepsilon)$ is the second. The most interesting example from this spectral set is shown in Figure 5.9, in which we see a dramatic inverted edge profile near 0.7 keV and a clear (but slightly less dramatic) inverted edge profile near 0.86 keV. These differences strongly suggest that the denominator spectrum, constant, should have much larger optical depths for both O VII and O VIII, which is entirely consistent with the results shown in Figure 5.8.

Next we analyze the data selected by hardness and luminosity. The edge energies

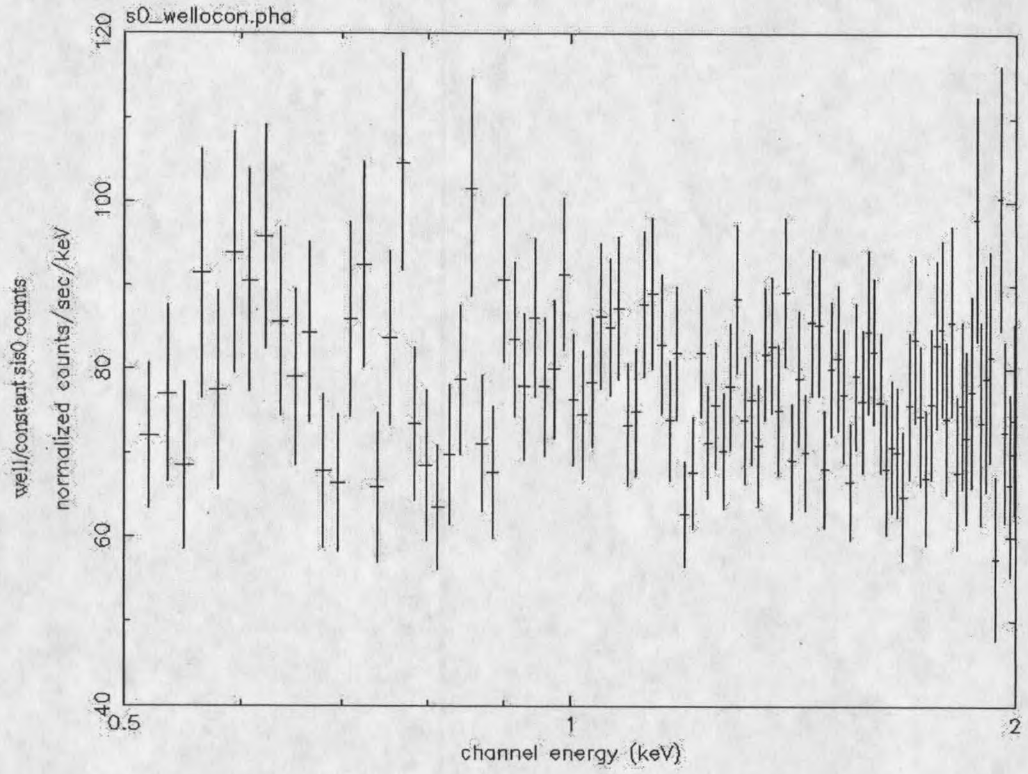

Figure 5.9: Ratio of Well to Constant Spectra

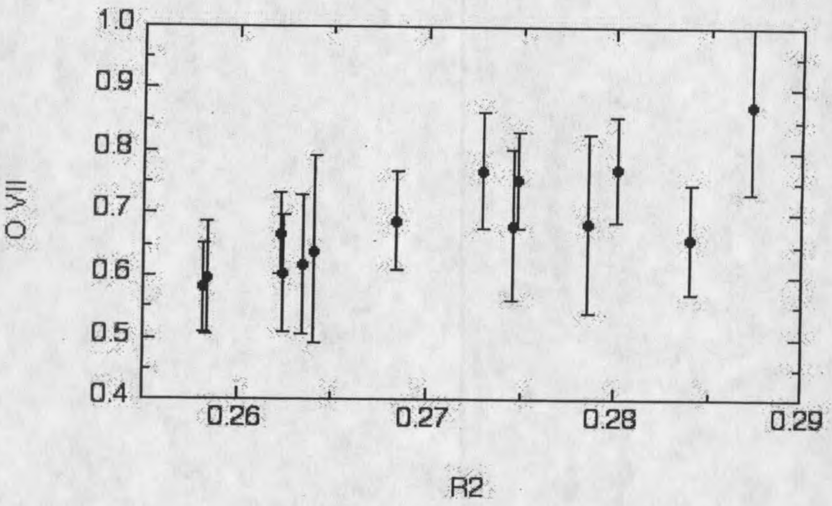

Figure 5.10: Variation of O VIII with R_2; horizontal axis is the value of R_2 for the spectrum, vertical axis is the measured optical depth of O VIII. Error bars shown are 3σ.

remain constant to within measurement error for this data set; the goodness-of-fit are comparable to those of Otani *et. al* (1995);the interested reader can find them in Appendix B. The optical depths of the edges, however, vary according to the hardness of the spectrum; the variation of O VII is shown in Figure 5.10. Not only does *d1*, which corresponds to the deep minimum near the end of the observation, have a substantially lower depth than any other region, *d34*, which corresponds mostly to minima in the observation, also has an O VII edge depth which is smaller than several other regions to 3σ significance. This strongly suggests that the O VII optical depth varies during the course of the observation.

Variation in O VIII is also evident, as shown in Figure 5.11, where the optical depth appears to be correlated with the hardness ration R_2. However, data set *c1* has the highest hardness ratio of this selection method, and does not differ significantly

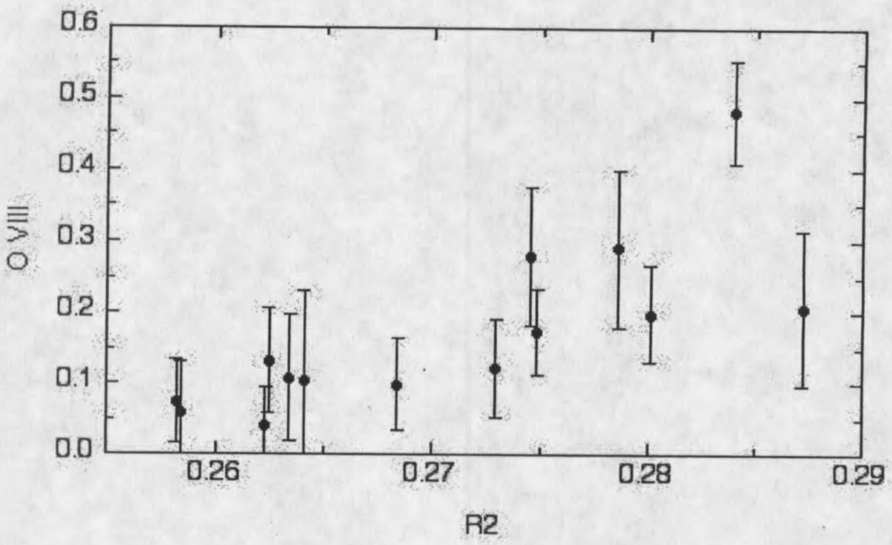

Figure 5.11: Variation of O VIII with R_2; horizontal axis is the value of R_2 for the spectrum and vertical axis is the measured value of O VIII. Error bars shown are 3σ.

Covering Factor	$\Gamma = 1.7$	$\Gamma = 1.8$	$\Gamma = 1.9$	$\Gamma = 2.0$
1.0	$N_h = 21.001$	21.331	$21.549^{+0.008}_{-0.011}$	$21.652^{+0.020}_{-0.014}$
	$\xi = -1.57$	-1.50	$\xi = -1.32 \pm 0.03$	$-1.33^{+0.06}_{-0.05}$
	$\chi^2 = 6502$	4915	$\chi^2 = 4263$	$\chi^2 = 4540$
0.5	$N_h = 21.25$		$N_h = 21.4975$	
	$\xi = 0.60$		$\xi = 0.44$	
	$\chi^2 = 6967$		$\chi^2 = 4241$	

Table 5.10: Average Values of the Single-Zone Photoionization Model; confidence regions shown are 3σ limits. For each fit the degrees of freedom are 2371.

from any data set other than *d1*, which has a significantly higher optical depth for O VIII. However, the low-hardness data sets *a4* and *b4* have significantly lower O VIII than do the high-hardness data sets *d1,d2,c2,* and *ab1*, and data set*c4* has lower O VIII than does *d1*.

Data Set	Column Density	U	$L_x \times 10^{42} erg/s$	χ^2/dof
con	$21.50^{+0.03}_{-0.03}$	$0.429^{+0.082}_{-0.079}$	11.06	1.222
inc	$21.31^{+0.04}_{-0.04}$	$0.319^{+0.114}_{-0.119}$	13.28	1.132
dec	$21.47^{+0.04}_{-0.04}$	$0.480^{+0.095}_{-0.106}$	12.23	1.081
flare	$21.44^{+0.03}_{-0.03}$	$0.349^{+0.092}_{-0.105}$	15.57	1.121
well	$21.28^{+0.05}_{-0.03}$	$0.291^{+0.154}_{-0.089}$	12.56	1.211
jump	$21.44^{+0.03}_{-0.03}$	$0.390^{+0.032}_{-0.105}$	12.45	1.232
fall	$21.44^{+0.02}_{-0.03}$	$0.386^{+0.075}_{-0.099}$	11.56	1.195
spring	$21.52^{+0.03}_{-0.03}$	$0.534^{+0.060}_{-0.083}$	12.02	1.195
trip	$21.45^{+0.03}_{-0.03}$	$0.348^{+0.204}_{-0.110}$	12.09	1.196
wobble	$21.51^{+0.03}_{-0.03}$	$0.494^{+0.076}_{-0.084}$	10.17	1.249

Table 5.11: The best-fit parameters from the photoionization code ION are shown. The slope was kept at a constant value of 1.9 for these data.

Data Set	Column Density	U	$L_x \times 10^{42} erg/s$	χ^2/dof
ab1	$21.54^{+0.04}_{-0.05}$	$0.53^{+0.09}_{-0.36}$	14.47	1.103
a2	$21.44^{+0.03}_{-0.02}$	$0.23^{+0.08}_{-0.08}$	16.70	1.147
a3	$21.34^{+0.02}_{-0.02}$	$0.29^{+0.06}_{-0.09}$	16.06	1.238
a4	$21.30^{+0.04}_{-0.02}$	$0.29^{+0.12}_{-0.08}$	16.01	1.353
b2	$21.44^{+0.04}_{-0.02}$	$0.27^{+0.12}_{-0.10}$	13.07	1.118
b3	$21.41^{+0.03}_{-0.03}$	$0.33^{+0.10}_{-0.09}$	12.53	1.219
b4	$21.32^{+0.05}_{-0.03}$	$0.29^{+0.14}_{-0.10}$	12.33	1.100
c1	$21.55^{+0.03}_{-0.04}$	$0.37^{+0.10}_{-0.15}$	11.38	1.173
c2	$21.54^{+0.03}_{-0.03}$	$0.46^{+0.07}_{-0.07}$	11.32	1.101
c3	$21.40^{+0.06}_{-0.04}$	$0.35^{+0.14}_{-0.11}$	10.85	1.095
c4	$21.39^{+0.06}_{-0.06}$	$0.30^{+0.20}_{-0.20}$	10.60	1.027
d1	$21.83^{+0.03}_{-0.03}$	$0.89^{+0.04}_{-0.04}$	7.389	1.258
d2	$21.54^{+0.05}_{-0.04}$	$0.46^{+0.13}_{-0.12}$	8.623	1.147
d34	$21.42^{+0.05}_{-0.05}$	$0.44^{+0.14}_{-0.15}$	8.267	1.089

Table 5.12: The best-fit parameters from the photoionization code ION are shown.

Photoionization Models of Total Spectrum

The soft X-ray parameters describe a hot plasma with temperature near 10^5 K. The relative strengths of the emission lines, when combined, give far more information than this- they also give information about the structure and isotropy of the warm absorber. For this reason, we model the results using one of the available photoionization codes, ION. The grid of pertinent fits to the model is shown in Table 5.10.

We next investigate the variations of the one-zone photoionization model with dynamic state by analyzing the Method C spectra. The best-fit parameters are as shown in Table 5.11. The variation of ionization parameter is substantially smaller for the dynamic states, which vary little in luminosity, than for data sets from the other three selection methods, which vary far more widely in luminosity. The basic trend of these data is to show a correlation between high column densities and high ionization parameters, which is likely to be an artifact of the fitting procedure.

The best-fit values for a one-zone photoionization model are shown in Table 5.12. A slope of 1.7 was used for Data Set d1; in all other cases a slope of 1.9 provided the best fit. Here again, the deep minimum state shows both a higher column density and ionization parameter than any of the other states; this is consistent with the previous findings of the empirical model.

Conclusions

Apparent changes in photon index for a power law spectrum are usually attributed to either changes in the reflection parameters or changes in absorption by gas or dust.

The results in the appendices demonstrate that the method of spectral selection, and not the method of spectral analysis, is the cause of the new results.

The continuum emission of the source was carefully examined using six different models. While partial reflection models are consistent with the data, simple models of partial absorption of the continuum by gas and dust fit the data best; there exists substantial evidence that the continuum is reddened due to absorption by dust. The models of partial absorption fit the data extremely well. The presence of absorbing gas and dust is consistent with UV,optical, and IR observations of this galaxy (Reynolds *et. al.* 1997), so it is likely that the continuum shape is influenced by this effect.

The data suggest that the continuum may be partially absorbed by ionizing gas, but this presence of such gas can only be determined to 1σ significance. Variation in the underlying photon index and the column density of an absorbing column of gas are measured, but both parameters increase simultaneously for all of the data sets where statistically significant variation is measured. The possibility that the variation is due to the response function of ASCA and fitting algorithms of XSPEC was then confirmed by examining a contour plot of the two parameters.

Otani's (1995) analysis of this observation using standard selection criteria indicated that the O VIII edge varied with SIS count rate according to the relation:

$$\tau_{OVIII} = (0.38 \pm 0.05) C^{-0.96 \pm 0.30} \tag{5.2}$$

suggesting that the warm absorber depends on luminosity. We found that

$$\tau_{OVIII} = (1.29 \pm 0.67)\left(\frac{L}{10^{42} erg/s}\right)^{-(0.89\pm0.57)} \tag{5.3}$$

which is consistent with Otani's result since count rate and luminosity are linearly related for a simple power law model. We also found that the O VIII edge depends on the hardness ratio R_2, despite the lack of correlation between luminosity and R_2. O VIII increases with hardness. In contrast, there is no strong relation between the O VII edge and the hardness of the source, although we did find variations of O VII with luminosity. Reynolds (1995) also found such variations.

Several factors account for the differences in Oxygen edge depths of our findings and those of the previous analyses; first, using phenomenological selection techniques we analyze the data on shorter timescales than the previous observers. Secondly, we used a more rigorous method for measuring the photon index than did previous observers, and did not allow it to vary at the same time as the oxygen edges. Finally, we included data from all four detectors in our analysis, although the two GIS detectors were only considered for energies above 1 keV. We found that we could reproduce the results of Reynolds (1995) by allowing the photon index to vary freely while fitting soft energy features. We note that our method and that of Reynolds (1995) produce nearly linear correlations between the 2–10 keV luminosity of SIS0 channel and the SIS0 count rate, while that of Otani does not. We conclude that constraining the neutral hydrogen absorption and including some method of modelling the hard energy

X-rays are critical in finding this variation, although the phenomenological method of screening makes the difference more apparent.

CHAPTER 6

CONCLUSION

At this moment, but only just in time to save the book from extinction, Orlando pushed away her chair, stretched her arms, dropped her pen, came to the window, and exclaimed, "Done!"

-Virginia Woolf, **Orlando**

In this chapter, a summary of all work in this thesis is given, and conclusions common to the analyses drawn. Some suggestions for further investigation are also given.

X-ray Variability of Active Galactic Nuclei

In Chapter 2, we demonstrated that light curves from the Seyfert galaxy NGC 3227 are consistent with constraints one would expect from a model of magnetic reconnection of a flux tube. We began by adding cooling terms associated with Compton upscattering and synchrotron radiation to the energy conservation equation for a flux tube previously derived by Fisher and Hawley (1990). Using the same technique as they, we derived a relation between the loop semi-length of the flux tube L, the loop apex temperature T_A, and the rise and decay times from the light curves. Since at present there is no empirical way to measure the apex temperature, we examined a plot of T_A vs. L for a set of flares observed on the Seyfert 1.5 galaxy NGC 3227. The result was that when regions excluded by physical constraints due to energy emission, pressure scale height and the speed of sound through the flux tube were eliminated, flux tubes were still physically plausible for the temperature range thought to be consistent with an AGN corona.

Implications on the Structure of Seyfert Galaxies

Two sources were analyzed in this work: Arkarian 120 and MCG-6-30-15. For Arkarian 120, the analysis focussed on determining the best fit parameters for the continuum shape, since it is a short observation, and this source is less observed in the X-ray than was MCG-6-30-15. For MCG-6-30-15 the analysis focussed on using new selection techniques to predict spectral changes over long observations. The two sources represent different extremes of current observations of Seyfert Galaxies: Arkarian 120 is the highest luminosity of the three, but is also the most distant, and the most obscured by Galactic hydrogen. The observation was relatively short, so only one statistically robust spectrum was analyzed. MCG-6-30-15 was characterized by rapid variability on very short timescales, for an extremely long, continuous observation.

In Chapter 3 a detailed explanation of the analysis techniques used on each of the two sources was given. The first sections described the techniques of timing analysis and spectral analysis used, which (though not exciting) are important because they are the source of different results of this work and one of the published analyses of MCG-6-30-15. The later sections describe data grouping techniques developed by the author for subsequent analysis of MCG-6-30-15. The discussion is supplemented by Appendix A, which gave a description of the models and statistical techniques used to analyze the data.

In Chapter 4, the Seyfert galaxy Arkarian 120 was analyzed. The main findings were that the soft X-rays are better fit by blackbody components than by oxygen edges which typify a warm absorber. The variability of this source, and of its hardness ratios, was suggestive that a longer observation of the galaxy would be interesting in terms of continued analysis by phenomenological grouping- particularly since this source shows flares which appear to have the same linear increase and exponential decrease as those which appeared in NGC 3227, and are characteristic of magnetic loops.

Chapter 5 contains the more interesting parts of an extensive analysis of MCG-6-30-15; the less interesting parts having been relegated to several appendices. Two classification schemes for sorting events files into spectra were created by the author (inspired by previous work by Dr. Kunieda, currently of ISAS), and applied to the data. They showed that, when grouped together, local minima had a lower degree of ionization than other phenomenologies in the spectrum- including a prolonged deep minimum at the end of the observation. The primary physical significance of this finding is that at least some of the O VII must be located as close to the nucleus as is the O VIII; the previous work suggested that O VII should be located farther from the central engine than the O VIII.

The two observations show a few similarities: both have variability in hardness ratio R_2, suggestive that the warm absorber (or other soft X-ray component, in the case of Arkarian 120) is variable. The apparent continuum variability for MCG-6-30-15 is actually due to its extremely strong, broad iron Kα line.

Concluding Remarks

Magnetic loops may well be responsible for variability of Seyfert 1 galaxies, and perhaps other AGN as well. NGC 3227 is not the only source which has individual flares which fit the linear increase and exponential decrease pattern reminiscent of solar flares; further analysis of sources in this light would be interesting as Chandra and XMM data become publicly available.

The results of the phenomenological classification schemes developed in this work are suggestive of the statistically robust correlation between X-ray spectrum and phenomenology of AGN and Galactic black holes such as Cygnus X-1. Classification by hardness ratio (or by derivative of the luminosity) seems to be very good at grouping data sets which have variation in the warm absorber. This suggests that the technique may also be applied to the data from the new generation X-ray satellites, where the exposure needed for a statistically viable spectrum is shorter.

BIBLIOGRAPHY

BIBLIOGRAPHY

[1] L. Acton "Radiative Transfer of X-rays in the Solar Corona" ApJ**225** 1069 (1978).

[2] I. Aretxaga "AGN Variability: from Seyfert Nuclei to QSO's", *Revista Mexicana de Astronomia y Astrofisica Serie de Conferencias* **6** 207A (1997).

[3] K. Arnaud. *The ASCA Data Reduction Guide, Version 2.0* Goddard Space Flight Center: NASA. 2000.

[4] D. L. Band and J. E. Grindlay "The Synchrotron Self-Compton Process in Spherical Geometries I. Theoretical Framework" ApJ **298** 128 (1985).

[5] R. Barbon, E. Capellaro, and M. Turatto. "The Asiago Supernova Catalogue" A&A **81** 421 (1989).

[6] P. Barr and R. F. Muschotzky. "Limits of X-ray variability in active galactic nuclei" Nature **320** 421 (1986).

[7] R. Barvainis and C. Lonsdale "Radio Spectra of Radio Quiet Quasars" AJ **111** 1431. (1996).

[8] Baudelaire "Harmonie du Soir" *Les Fleurs du Mal* 1886.

[9] M. C. Begelman, R. D. Blanford and M. J. Rees. "Theory of Extragalactic Radio Sources" *Reviews of Modern Physics* **56** 255 (1984).

[10] M. C. Begelman, M. Sikora and M. J. Rees. "Thermal and dynamical effects of pair production on two-temperature accretion flows" ApJ **313** 689 (1987).

[11] M. C. Begelman. "Supermassive Black Holes" *American Astronomical Society Meeting* **192** (1998).

[12] W. Benarek and R. J. Protheroe "Modulation of AGN Gamma Rays by Interaction with X-rays from an Accretion Disk Hot Spot" in *Relativistic Jets in AGNs* 303 (1997).

[13] V. E. Bianchi and L. Stella. "Measuring black hole mass through variable line profiles from accretion disks" Nature **344** 747 (1990).

[14] N. D. Birrell and P. C. W. Davies, "On falling through a black hole into another universe" Nature **272**, 35(1978).

[15] D. Biskamp "Magnetic Reconnection via Current Sheets" *Physics of Fluids* **29** 153 (1986).

[16] G. Björnsson "Optically Thin Accretion Disks in the Kerr Metric" ApJ **441** 765 (1995).

[17] R. D. Blanford "Physical Processes in Active Galactic Nuclei" in *Active Galactic Nuclei* (Springer-Verlag: 1990).

[18] H. V. D. Bradt, T. Ohashi, and K. A. Pounds. "X-ray Astronomy Missions" ARA&A **30** 391 (1992).

[19] , W. N. Brandt, W. Mathur, and M. Elvis. "A Comparison of the Hard ASCA Spectral Slopes of Broad and Narrow-line Seyfert 1 Galaxies" MNRAS **285** 25 (1997).

[20] W. N. Brandt, A. C. Fabian, T. Dotani, F. Nagase, H. Inoue, T. Kotani and Y. Segawa "ASCA observations of the iron K complex of Circinus X-1 near Zero Phase: Spectral Evidence for Partial Covering" MNRAS **283** 1071 (1996).

[21] W. N. Brandt, A. C. Fabian, K. Nandra, and S. Tsuruta "ROSAT PSPC Observations of NGC 7469 and Ark 120" MNRAS **265** 996 (1993).

[22] , B. C. Bromley, K. Chen and W. A. Miller "Line Emission from an Accretion Disk around a Rotating Black Hole: Toward a Measurement of Frame Dragging" ApJ **475** 57 (1997).

[23] G. R. Burbidge, D. Layzer, and J. G. Phillips. ARA&A **12** 502 (1974).

[24] D. Caditz and S. Tsuruta. "Adiabatic Shocks in Accretion Flows" ApJ **501** 242 (1998).

[25] I. Calvino *If on a Winter's Night a Traveler* (Harcourt-Brace, New York: 1979).

[26] R. C. Canfield *et. al.* in *Energetic Phenomena in the Sun* ed. M. Kendu and B. Woodgate. Chapter 3 Nasa Conference Publication 2439 (1986).

[27] M. Cappi, T. Mihara, M. Matsuoka, K. Hayashida, K. A. Weaver, C. Otani, "Warm Absorber, Reflection and Fe K line in the X-ray Spectrum of IC 4329A" ApJ **458** 149 (1996).

[28] P. A. Charles and F. D. Seward *Exploring the X-ray Universe*(Cambridge University Press, Cambridge: 1995).

[29] K. Chen, J. P. Halpern, and L. G. Titarchuk. " Polarization of Line Emission from an Accretion Disk and Application to ARP 102B" ApJ **483** 194 (1997).

[30] X. Chen and R. E. Taam "The Structure and Stability of Transonic Accretion Disks Surrounding Black Holes" ApJ **412** 254 (1993).

[31] J. Chiang, C. S. Reynolds, O. M. Blaes, M. A. Nowak, N. Murray, G. Madejski, H. L. Marshall, and P. Magdziarz. "Simultaneous EUVE/ASCA/RXTE Observations of NGC 5548" ApJ **528** 292 (2000).

[32] J. Clavel, G. A. Reichert, D. Alloin, D. M. Crenshaw, G. Kriss, J. H. Krolik, M. A. Malkan, H. Netzer, B. M. Peterson, W. Wamsteker, A. Altamore, T. Baribaud, P. Barr, S. Beck, L. Binette, G. E. Bromage, N. Brosch, A. I. Diaz, A. V. Filippenko, K. Fricke, C. M. Gaskell, P. Giommi, I. S. Glass, P. Gondhalekar, R. L. Hackney, J. P. Halpern, D. J. Hutter, S. Joersaeter, A. L. Kinney, W. Kollatschny, A. Koratkar, K. T. Korista, A. Laor, J. P. Lasota, E. Liebowit, D. Pelat, E. Perez, G. C. Perola, R. L. Ptak, P. Rodriguez-Pascual, E. I. Rosenblatt, A. C. Sadun, M. Santos-Lleo, R. A. Shaw, P. S. Smith, G. M. Stirpe, R. Stoner, W. H. Sun, M.-H. Ulrich, E. Van Groningen, and W. Zheng. "Steps Toward Detemination of the Size and Structure of the Broad-Line Region in Active Galactic Nuclei. I. An 8 Month Campaign of Monitoring NGC 5548 with IUE. ApJ **366** 64 (1991).

[33] J. Clavel, K. Nandra, F. Makino, K. A. Pounds, G. A. Reichert, C. M. Urry, W. Wamsteker, M. Peracaula-Bosch, G. C. Stewart, and C. Otani. "Correlated Hard X-ray and Ultraviolet Variability in NGC 5548" ApJ **393** 113 (1992).

[34] F. V. Coronitti "On the Magnetic Viscosity in Keplerian Accretion Disks" ApJ **244** 587 (1981).

[35] I. J. D. Craig, A. N. McClymont, J. H. Underwood "The Temperature Density Structure of Active Region Coronal Loops" A&A(1979).

[36] D. M. Crenshaw, S. B. Kraemer. "Intrinsic Absorption Lines in the Seyfert 1 Galaxy NGC 5548: Ultravioleet Echelle Spectra from the Space Telescope Imaging Spectrograph" **521** 572 (1999).

[37] C. T. Cunningham and J. M. Bardeen "The Optical Appearance of a Star Orbiting an Extreme Kerr Black Hole" ApJ **173** 237 (1973).

[38] C. T. Cunningham "The Effects of Redshifts and Focusing on the Spectrum of an Accretion Disk around a Kerr Black Hole" ApJ **202** 788 (1975).

[39] B. Czerny, A. Schwarzenberg-Czerny, and Z. Loska. "Power Density Spectrum of NGC 5548 and the Nature of its Variability" MNRAS **303** 148 1999.

[40] Y. Dabrowski, A. C. Fabian, K. Iwasawa, A. M. Lasenby, and C. S. Reynolds. "The Profile and Equivalent Width of the X-ray Iron Emission Line from a Disk Around a Kerr Black Hole" MNRAS(1997).

[41] K. Davidson "On Photoionization Analyses of Emission Spectra of Quasars" ApJ **218** 20 (1977).

[42] M. M. De Robertis, H. K. C. Yee and K. Hayhoe "A CCD Study of the Environment of Seyfert Galaxies: II. Testing the Interaction Hypothesis" ApJ **496** 93 (1998).

[43] R. M. González Delgado and E. Pérez. "The circumnuclear region in the Seyfert 1 Galaxy NGC 3227" MNRAS **284** 931 (1997).

[44] T. DiMatteo, A. Celotti and A. C. Fabian. "Magnetic Flares in Accretion Disk Coronae and the Spectral States of Black Hole Candidates: the Case of GX 339-4" MNRAS **304** 809 (1999).

[45] T. DiMatteo. "Magnetic Reconnection: Flares and Coronal Heating in Active Galactic Nuclei" MNRAS **299** L1 (1998).

[46] Dickey and Lockman. ARA&A **28** 215 (1990).

[47] C. Done and J. H. Krolik "Kinematics of the Broad Emission Line Region in NGC 5548" ApJ **463** 144 (1996).

[48] M. A. Dopita and R. S. Sutherland "Spectral Signatures of Fast Shocks I. Low-Density Model Grid" ApJS **102** 161 (1996).

[49] M. A. Dopita and R. S. Sutherland "Spectral Signatures of Fast Shocks II. Optical Diagnostic Diagrams" ApJ **455** 468 (1995).

[50] M. A. Dopita "Photoionising Shocks in SNRs and AGN" *Astronomy and Space Science* **233** 215 (1995).

[51] T. Dotani, A. Yamashita, A. Rasmussen, and the SIS team "Effects of Radiation Damage on SIS Performance" (NASA: 1997).

[52] J. B. Dove, J. Wilms, and M. C. Begelman "Self- Consistent Accretion Disk Corona Models for Compact Objects I: the Corona and the Spectrum of Escaping Radiation" ApJ **487** 747 (1997).

[53] D. Dultzin-Hacyan, V. Krongold, I. Fuentes-Furidi, and P. Marziani. "The Close Environment of Seyfert Galaxies and its Implication for Unification Models". ApJ **513** p. L111 (1999).

[54] J. Durrant and S. F. Brown "Coronal Loops in Solar Active Regions" **8** 137 (1989).

[55] M. Elvis, T. Maccacaro, A. S. Wilson, M. J. Ward, M. V. Penston, R. A. E. Fosbury, G. C. Perola "Seyfert Galaxies as X-ray Sources" MNRAS **183** 129 (1978).

[56] M. Elvis, F. J. Lockman, and B. J. Wilkes "Accurate Galactic N_h Values towards Quasars and AGN" AJ **97** 777 (1989).

[57] A. C. Fabian and X. Barcons "The Origin of the X-ray Background" ARA&A **30** 429 (1992).

[58] A. C. Fabian, H. Kunieda, S. Inoue et. al. PASJ **46** L59 (1994).

[59] A. C. Fabian, M. J. Rees, L. Stella and N. E. White "X-ray Fluorescence from the Inner Disc in Cygnus X-1" MNRAS **238** 729 (1989).

[60] A. C. Fabian and R. Terlevich "X-ray detection of SN1988Z with the ROSAT HRI" MNRAS **280** L5 (1996).

[61] A. C. Fabian, K. Nandra, C. S. Reynolds, W. N. Brandt, C. Otani, Y. Tanaka, H. Inoue, and K. Iwasawa. "On broad iron Kalpha lines in Seyfert 1 galaxies" MNRAS **277** L11 (1995).

[62] A. C. Fabian, S. Inoue, H. Kunieda, M. Matsuoka, T. Mihara, S. Miyamoto, C. Otani, G. Ricker, Y. Tanaka, M. Yamauchi, and T. Yaqoob "ASCA Observations of the Warm Absorber in MCG-6-30-15; the Discovery of a Change in the Column Density" PASJ **46** L59 (1994).

[63] D. Fadda, G. Giuricin, G. L. Granato, and D. Vecchies "The Near- and Mid-Infrared Continuum Emission in Seyfert Nuclei: Constraints on the Models of Obscuring Tori" ApJ **496** 117 (1998).

[64] J. W. Ferguson and G. J. Ferland "Accurate Hydrogen Spectral Simulations with a Compact Model Atom" ApJ **479** 363 (1997).

[65] G. J. Ferland and J. W. Truran "An X-ray Model for the Nebula of Nova DQ Herculis 1934" ApJ **244** 1022 (1981).

[66] G. J. Ferland and H. Netzer "Are There any Shock- Heated Galaxies?" ApJ **264** 105 (1983).

[67] G. J. Ferland "Hazy, A Brief Introduction to Cloudy" University of Kentucky Department of Physics and Astronomy Internal Report (1996).

[68] F. Fiore, G. C. Perola, M. Matsuoka, M. Yamauchi, and L. Piro "Time-resolved Spectral Analysis of Three Seyfert Galaxies Observed with Ginga" A&A **262** 37 (1992).

[69] G. H. Fisher and S. L. Hawley "An Equation for the Evolution of Solar and Stellar Flare Loops" ApJ **357** 243 (1990).

[70] J. Frank, A. King and D. Rainie *Accretion Power in Astrophysics* (Cambridge University Press, Cambridge: 1992).

[71] A. A. Galeev, R. Rosner, and G. S. Vaiana "Structured Coronae of Accretion Disks" ApJ **229** 318 (1979).

[72] J. F. Gallimore, S. A. Baum, and C. P. O'Dea, " The Subarcsecond Radio Structure in NGC 1068. I. Observations and Results" ApJ **458** 136 (1996).

[73] I. M. George and A. C. Fabian "X-ray reflection from Cold Matter in Active Galactic Nuclei and X-ray binaries" MNRAS **249** 352 (1991).

[74] I. M. George, T. J. Turner, K. Nandra, R. F. Mushotzky, and T. Yaqoob ApJS **114** 73 (1998).

[75] I. M. George, R. Mushotzky, T. J. Turner, T. Yaqoob, A. Ptak, K. Nandra, and H. Netzer. "The X-ray Spectral Variability of the Seyfert Galaxy NGC 3227" ApJ **509** 146 (1998).

[76] M. K. Geourgoulis, M. Velli, and G. Einaudi "Statistical Properties of Magnetic Activity in the Solar Corona" ARA&A **497** 957 (1998).

[77] R. Giacconi, H. Gursky, F. R. Paolini and B. B. Rossi "Evidence for X-rays from Sources outside the Solar System" Phys. Rev. Lett. **9** 439 (1962).

[78] M. Goad and A. Koratkar. "Broad Emission Line Variability as a Constraint Upon the Physical Conditions within the Broad Emission Line Region of NGC 5548" ApJ **495** 718 (1998).

[79] D. Gondek, A. A. Zdziarski, W. N. Johnson, I. M. George, K. McNaron-Brown, P. Magdziarz, D. Smith and D. E. Gruber. "The Average X-ray/gamma-ray spectrum of radio-quiet Seyfert 1s" MNRAS **282** 646 (1996).

[80] M. D. Gregg, R. H. Becker, R. L. White, D. J. Helfand, R. G. McMahon, and I. M. Hock "The FIRST Bright QSO Survey" AJ **112** 407 (1996).

[81] P. W. Guilbert, A. C. Fabian, and R. McCray "Why are Broad Emission Lines Seen in Seyfert Galaxies and not in BL Lacertae Objects?" ApJ **266** 466 (1983).

[82] H. Gursky and D. A. Schwartz "Extragalactic X-ray Sources" ARA&A **15** 541 (1977).

[83] F. Haardt "Models for the X-ray Emission from Radio Quiet AGNs" Mem. Soc. Astron. Ital. **68** 73 (1997).

[84] S. L. Hawley et. al. "Simultaneous Extreme- Ultraviolet Explorer and Optical Observations of AD Leonis: Evidence for Large Coronal Loops and the Neupert Effect in Stellar Flares" ApJ **453** 464 (1995).

[85] M. J. C. Hayes, J. L. Culhane, R. J. Blisset, P. Barr, and S. J. Bell Burnell. MNRAS **193** 15 (1980).

[86] C. Heiles "The Interstellar Magnetic Field" ARA&A **14** 1 (1975).

[87] G. Henri and P. O. Petrucci "Anisotropic Illumination of AGN's Accretion disk by a Nonthermal Source: I. General Theory and Application to the Newtonian Geometry" A&A **326** 87 (1997).

[88] K. Hitorani, M. Takahashi, S. Nitta and A. Tomimatsu "Accretion in a Kerr Black Hole Magnetosphere: Energy and Angular Momentum Transport between the Magnetic Field and the Matter" ApJ **386** 455 (1992).

[89] R. F. Howard "Solar Active Regions as Diagnostics of Subsurface Conditions" ARA&A **34** 75 (1996).

[90] Y. Ikebe, Y. Ishisaki, H. Kubo, E. Idesawa, T. Takahashi, K. Makashima, and the GIS Team "Method of GIS Background Subtraction" (1995).

[91] K. Iwasawa, A. C. Fabian, A. J. Young, and C. Matsumoto. "Variation of the Broad X-ray Iron Line in MCG-6-30-15 During a Flare" MNRAS **306** L19 (1999).

[92] K. Iwasawa, A. C. Fabian and K. Nandra. "ASCA and ROSAT Observations of NGC5548: Discrepant Spectral Indices" MNRAS **307** 611 (1999).

[93] K. Iwasawa, A. C. Fabian, G. Matt "The Iron K line Complex in NGC 1068: Implications for X-ray Reflection in the Nucleus" MNRAS **289** 443 (1997).

[94] K. Iwasawa, A. C. Fabian, S. Ueno, H. Awaki, Y. Fukazawa, K. Matsushita, and K. Makashima "ASCA PV Observations of the Seyfert 2 Galaxy NGC 4388: the Obscured Nucleus and its X-ray Emission" MNRAS **285** 683 (1997).

[95] K. Iwasawa, A. C. Fabian, C. S. Reynolds, K. Nandra, C. Otani, H. Inoue, K. Hayashida, W. N. Brandt, T. Dotani, H. Kunieda, M. Matsuoka, and Y. Tanaka "The Variable Iron K Emission Line in MCG-6-30-15" MNRAS (1996).

[96] K. Iwasawa and Y. Taniguchi "The X-ray Baldwin Effect" ApJ **413** L15 (1993).

[97] M. König and J. Timmer "Analyzing X-ray Variability by Linear State Space Models" in *Astronomical Time Series* 265 (1996).

[98] T. R. Kallman and R. McCray "X-ray Nebular Models" ApJS **50** 253 (1982).

[99] C. C. Kankelborg, A. B. C. Walker II, and R. B. Hoover "Observation and Modeling of Soft X-ray Bright Points II. Determination of Temperature and Energy Balance" ApJ **491** 952 (1997).

[100] R. Kano and S. Tsuneta ApJ **454** 934 (1995).

[101] V. Karas and R. Mucha "Accretion onto a Rotating Compact Object in General Relativity" Am. J. Phys. **61** 825 (1993).

[102] V. Karas "Fourier-phase Analysis of the Orbiting Bright Spot Model for AGN Variability" MNRAS **288** 12 (1997).

[103] V. Karas "Light Curve of a Source Orbiting a Black Hole: A Fitting Formula" ApJ **470** 743 (1996).

[104] S. Kaspi and H. Netzer. "Modeling Variable Emission Lines in Active Galactic Nuclei: Method and Application to NGC 5548" ApJ **524** 71 (1999).

[105] W. C. Keel. AJ **85** 198.

[106] M. J. Kellen "X-ray Observations and Theoretical Modeling of Active Galactic Nuclei" Ph. D. Thesis, Montana State Univeersity (1997).

[107] W. Kley "On Relativistic Discs and Rings" MNRAS **287** 26 (1997).

[108] J. A. Klimchuck and L. J. Porter Nature (1995).

[109] S. Komassa and H. Fink "Evidence for a *dusty* warm absorber in NGC 3227?" A&A **327** 483 (1997).

[110] S. Komossa and H. Fink "A ROSAT Observation of the Warm- Absorbed Soft X-ray Spectrum of NGC 4051" in *Roentgenstrahlung from the Universe* 463 (1996).

[111] K. Korista, G. Ferland and J. Baldwin "Do the Broad Emission Line Clouds See the Same Continuum that We See?" ApJ **487** 555 (1997).

[112] K. Korista,J. Baldwin, G. Ferland, and D. Verner "An Atlas of Computed Equivalent Widths of Quasar Broad Emission Lines" ApJS **108** 401 (1997).

[113] J. Kormendy and D. Richston "Inward Bound- the Search for Supermassive Black Holes in Galactic Nuclei" ARA&A **33** 581 (1995).

[114] J. K. Kotilainen "The Host Galaxies of Nearby Seyfert 1 Nuclei" *Astrophysics and Space Science* **205** 107 (1993).

[115] S. B. Kraemer, D. M. Crenshaw, A. V. Filippenko, and B. M. Peterson "Evidence for a Physically Compact Narrow-Line Region in the Seyfert 1 Galaxy NGC 5548" ApJ **499** 719 (1998).

[116] J. H. Krolik, C. F. McKee and C. B. Tarter "Two-Phase Models of Quasar Emission Line Regions" ApJ **249** 442 (1981).

[117] J. H. Krolik and G. M. Voit "What is the True Covering Factor of Absorbing Material in BALQSO's?" ApJ **497** (1998).

[118] J. H. Krolik "A Unified View of How the Study of Emission Lines Further our Knowledge of AGN" *ASP Conf. Ser. 113: IAU Colloq. 159: Emission Lines in Active Galaxies: New Methods and Techniques* **159** 459 (1997).

[119] J. H. Krolik "A New Equilibrium for Accretion Disks around Black Holes" ApJ **498** 13 (1998).

[120] H. Kunieda *et. al.* Nature **345** 786 (1990).

[121] H. Kunieda, S. Hayakawa, Y. Tawara, S. Tsuruta and K. Leighly "X-ray Spectral Variability of the Seyfert 1 Galaxy NGC 4051" ApJ **384** 482 (1992).

[122] H. Kunieda, personal communication.

[123] M. Landini and B. C. Monsignor-Fossi "The X-UV Spectrum of Thin Plasmas" A&AS **82** 229 (1990).

[124] A. Laor "Line Profiles from a Disk around a Rotating Black Hole" ApJ **376** 90 (1991).

[125] K. Leighly Ph.D. Thesis.

[126] J. P. S. Lemos "Black Holes: From Galactic Nuclei to Elementary Particles" *Proceedings of the* XXI^{th} *SAB 1995 Meeting* (1995).

[127] A. P. Lightman and W. Zdziarski "Pair production and Compton scattering in compact sources and comparison to observations of active galactic nuclei" ApJ **319** 643 (1987).

[128] A. P. Lightman and T. R. White "Effects of Cold Matter in Active Galactic Nuclei: a Broad Hump in the X-ray Spectrum" ApJ **335** 57 (1988).

[129] R. P. Lin and H. S. Hudson. Sol. Phys. **50** 153 (1976).

[130] D. N. C. Lin and J. C. B. Papaloizou "Theory of Accretion Disks II: Application to Observed Systems" ARA&A (1996)

[131] C. Loska and B. Czerny "Models of optical/UV continuum in AGN: Constraints from the NGC 5548 Monitoring Campaign" MNRAS **284** 946 (1997).

[132] R. Lupton *Statistics in Theory and Practice* (Princeton University Press, Princeton: 1993).

[133] P. Magdziarz, O. Blaes, A. A. Zdziarski, W. N. Johnson and D. A. Smith. "Broad-band Continuum and Variability of NGC 5548" *Proceedings of the Fourth Compton Symposium* 1288 (1997).

[134] P. Magdziarz and O. Blaes. "A Model of the Broad-Band Continuum of NGC 5548" *IAU Symposium* **188** 430 (1998).

[135] P. Magdziarz, O. Blaes, A. A. Zdziarski, W. N. Johnson and D. A. Smith. "A Spectral Decomposition of the Variable Optical, Ultraviolet, and X-ray Continuum of NGC 5548" MNRAS **301** 179 (1998).

[136] S. Mallarmé. "Un Coup de Des". *Oeuvres Complètes* eds. H. Mondor, G. Jean-Aubry. Paris: Gallimard, 1945.

[137] K. Makishima, Y. Maejima, K. Mitsuda, H. V. Bradt, R. A. Remillard, I. R. Tuohy, R. Hoshi, and M. Nakagawa. "Simultaneous X-ray and Optical Observations of Gx 339-4 in an X-ray High State" ApJ **308** 635 (1986).

[138] K. Mannheim "AGN Models: High-Energy Emission" in *Very High Energy Phenomena in the Universe* ed. Y. Giaruad-Heraud and J. Tran Thanh Van , 17 (1997).

[139] T. Marayama and Y. Taniguchi "Where is the Coronal Line Region in Active Galactic Nuclei" ApJ **497** (1998).

[140] P. Marziani, M. Calvani, and J. W. Sulentic ed. D. T. Wickramasinghe"On the Differences Between Radio Quiet and Radio Loud AGN" *Accretion Phenomena and Related Outflows* IAU Colloquium 163. ASP Conference Series; **121** 761 (1997)

[141] J. M. Mas-Hesse, P. M. Rodgriguez-Pascual, L. Sanz Fernandez De Cordoba, I. F. Mirabel, W. Wamsteker, F. Makino and C. Otani. "Multiwavelength analysis of active galaxies: implications on unified Seyfert Models" A&A **298** 22 (1995).

[142] S. Mathur, M. Elvis and B. Wilkes. "Multiple Velocity Components in the C IV Absorption Line of NGC 5548" ApJ **519** 605 (1999).

[143] M. Matsuoka, L. Piro, M. Yamauchi and T. Murakami "X-ray Spectral Variability and Complex Absorption in the Seyfert 1 Galaxies NGC 4051 and MCG-6-30-15" ApJ **361** 440 (1990).

[144] G. Matt, G. C. Perola and L. Stella "Multiple-Peaked Line profiles from Relativistic Disks at High Inclination Angles" A&A **267** 643 (1993).

[145] G. Matt, A. C. Fabian and R. R. Ross "Iron Kα lines from X-ray photoionized Accretion Disks" MNRAS **262** 179 (1993).

[146] G. Matt, G. C. Perola and L. Piro "The Iron Line and High Energy Bump as X-ray Signatures of Cold Matter in Seyfert 1 Galaxies" A&A **247** 25 (1991).

[147] Matt "The X-ray Spectrum of Compton-Thick Seyfert 2 Galaxies" *Memorie della Societa Astronica Italiana* **68** 127 (1997).

[148] D. McCammon, D. N. Burrows, W. T. Sanders, and W. L. Kraushaar. "The Soft X-ray Diffuse Background" ApJ **269** 107 (1983).

[149] A. N. McClymont and I. J. D. Craig. "Fast downflows in the solar transition region explained" ApJ **312** 402.

[150] T. McGlynn, K. Scollick, and N. White."Skyview: the Multi-Wavelength Sky on the Internet" McLean, B. J. *et. al.* *New Horizons in Multiwavelength Sky Surveys* IAU Symposium **179** 465 (1996).

[151] D. McKenzie, Personal Communication.

[152] T. R. Metcalf and G. H. Fisher "A Test of a New Flare Loop Scaling Law Using YOHKOH SXT and GOES Observations" ApJ **462** 977 (1996).

[153] C. W. Misner, K. S. Thorne, and J. A. Wheeler, *Gravitation* (Freeman, San Francisco, 1973).

[154] R. Misra and F. K. Sutaria. "Comparison of Various Model Fits to the Iron Line Profile in MCG-6-30-15" ApJ **517** 661 (1999).

[155] K. Mitsuda, H. Inoue, K. Koyama,K. Makishima, M. Masuoka, Y. Ogawara, N. Shibaaki, K. Suzuki, and Y. Tanaka. "Energy Spectra of Low-Mass Binary X-ray Sources Observed from Tenma" PASJ **36** 741 (1984).

[156] J. S. Mulchaey, A. S. Wilson, and Z. Tsvetanov. "An Imaging Survey of Early-Type Seyfert Galaxies. I. The Observations" ApJS **102** 309-367 (1996).

[157] C. G. Mundell, A. Pedlar, D. J. Axon, J. Meaburn, and S. W. Unger. "Neutral Hydrogen Studies of the Seyfert Galaxy NGC 3227" MNRAS **277** 641 (1995).

[158] R. F. Mushotzky , P. J. Serlemitsos, R. H. Becker, E. A. Boldt, and S. S. Holt. ApJ **220** 119 (1978).

[159] R. F. Mushotzky, C. Done, and K. A. Pounds "X-ray Spectra and Time Variability of AGN" ARA&A **31** 717 (1993).

[160] T. Muto, T. Takatsuka, R. Tamagaki, and T. Tatsumi. Prog. Theor. Phys. (Suppl. 112) Ch. 6 159 (1993).

[161] K. Nandra, K. A. Pounds, G. C. Stewart, I. M. George, K. Hayashida, F. Makino, and T. Ohashi. "Compton Reflection and the Variable X-ray Spectrum of NGC 5548" MNRAS **248** 760 (1993).

[162] K. Nandra and K. A. Pounds. "GINGA Observations of the X-ray Spectra of Seyfert Galaxies" MNRAS **268** 405 (1994).

[163] K. Nandra, I. M. George, R. F. Mushotzky, T. J. Turner and T. Yaqoob "ASCA Observations of Seyfert 1 Galaxies: II Relativistic Iron Kα emission" ApJ **477** 602 (1997).

[164] K. Nandra, I. M. George, R. F. Mushotzky, T. J. Turner and T. Yaqoob "On the Dependence of the Iron K-line Profiles with Luminosity in Active Galactic Nuclei" ApJ **488** L91 (1997).

[165] K. Nandra, K. A. Pounds, G. C. Stewart, A. C. Fabian and M. J. Rees "Detection of Iron Features in the X-ray Spectrum of the Seyfert I Galaxy MCG-6-30-15" MNRAS **236** 39 (1989).

[166] K. Nandra, K. A. Pounds and G. C. Stewart "The X-ray Spectrum of MCG-6-30-15 and its Temporal Variability" MNRAS **242** 660 (1990).

[167] K. Nandra. Ph.D. Thesis, Leister University. (1991)

[168] K. Nandra, R. F. Mushotzky, T. Yakoob, I. M. George, and T. J. Turner "Variability of the Iron K-Emission Line in the Seyfert 1 Galaxy NGC 3516" MNRAS **284** L7 (1996).

[169] P. Natarajan and J. E. Pringle. "The Alignment of Disk and Black Hole Spins in Active Galactic Nuclei" ApJ **506** L97-L100. (1998).

[170] Naval Research Laboratory Plasma Formulary.

[171] S. Nayakshin and F. Melia. "Magnetic Flares and the Observed $\tau_T \approx 1$ in Seyfert Galaxies" ApJ **490** L13 (1997).

[172] H. Netzer and B. M. Peterson "Reverberation Mapping and the Physics of Active Galactic Nuclei" *Astronomiical Time Series, Wise University 25th Anniversary* (1997).

[173] H. Netzer, T. J. Turner and I. M. George "X-ray Color Analysis of the Spectra of Active Galactic Nuclei" ApJ **435** 106 (1994).

[174] H. Netzer "X-ray Lines in Active Galactic Nuclei and Photoionized Gases" ApJ **473** 781 (1996).

[175] H. Netzer "Ionized Absorbers, Ionized Emitters, and the X-ray Spectrum of Active Galactic Nuclei" ApJ **411** 594 (1993).

[176] S. Nitta, M. Takahashi and A. Tomimatsu "Effects of Magnetohydrodynamic Accretion Flows on Global Structure of a Kerr Black-Hole Magnetosphere" Phys. Rev. D. **44** 2295 (1991). author=Nitta,S., M. Takahashi, A. Tomimatsu,

[177] P. T. O'Brien, M. R. Goad and P. M. Gondhalekar "The Luminosity-Dependent Broad-Line Region in Active Galactic Nuclei" MNRAS **275** 1125 (1995).

[178] D. E. Osterbrock and W. G. Mathews "Emission-Line Regions of Active Galaxies and QSO's" ARA&A **24** 171 (1986).

[179] D. E. Osterbrock "The Nature and Structure of Active Galactic Nuclei" ApJ **404** 551 (1993).

[180] E. C. Ostriker, J. P. Huchra, M. J. Geller, M. J. Kurz. "The Kinematics and Dynamics of the Rich Cluster of Galaxies Abell 539" AJ **96** 1775 (1988).

[181] C. Otani, T. Kii, C. S. Reynolds, A. C. Fabian,K. Iwsawa, K. Hayashida, H. Inoue and Y. Tanaka "The Variable O VIII Warm Absorber in MCG-6-30-15" PASJ **48** 211 (1995).

[182] D. N. Page and K. S. Thorne "Disk-Accretion onto a Black Hole I. Time-Averaged Structure of Accretion Disk" ApJ **191** 499 (1974).

[183] J. C. B. Papaloizou and D. N. C. Lin "Theory of Accretion Disks I: Angular Momentum Transport Processes" ARA&A **33** 505 (1995).

[184] V. I. Pariev "Hydrodynamic Accretion onto Rapidly Rotating Kerr Black Hole" MNRAS **283** 1264 (1996).

[185] E. N. Parker "The Origin of Solar Activity" ARA&A **15** 45 (1977).

[186] C. A. Perez "Observational Signatures of Rotating Black Holes" Ph.D. Thesis, Stanford University (1994).

[187] F. Perotti, E. Mattaini, E. Quadrini, E. Hard X-ray Spectral Feature Detected in the Region of MCG 8-11-11" ApJ **475** L89 (1997).

[188] B. M. Peterson and G. Ferland Nature **324** 325 (1986).

[189] B. M. Peterson, A. J. Barth, P. Berlind, R. Bertram, K. Bischoff, N. G. Bochkarev, A. N. Burenkov, F.-Z. Cheng, M. Dietrick, A. V. Filippenko, E. Giannuzzo, L. C. Ho, J. P. Huchra, J. Hunley, S. Kaspi, W. Kollatschny, D. C. Leonard, Yu. F. Malkov, T. Matheson, M. Mignoli, B. Nelson, P. Papaderos, J. Peters, R. W. Pogge, V. I. Pronik, S. G. Sergeev, E. A. Sergeeva, A. I. Shapovalova, G. M. Strippe, S. Tokarz, R. M. Wagner, I. Wanders, J.-Y. Wei, B. J. Wilkes, H. Wu, S.-J. Xue, Z.-L. Zou. "Steps Toward Determination of the Size and Strucutre of the Broadline Region in Active Galactic Nuclei. XV. Long-Term Optical Monitoring of NGC 5548" ApJ **510** 659 (1999).

[190] B. M. Peterson and A. Wandel. "Keplerian Motion of Broad-line Region Gas as Evidence for Supermassive Black Holes in Active Galactic Nuclei" ApJ **521** L95 (1999).

[191] R. Peter, K. Okada, T. Mihara, K. Makashima and E. J. M. Colber "The Broad Band X-ray Spectrum of SN 1978k and Two Other Luminous X-ray Sources in the Spiral Galaxy NGC 1313" PASJ **46** 115 (1994).

[192] P. O. Hydrodynamic Accretion onto and G. Henri "Anisotropic Illumination of AGN's Accretion disk by a Nonthermal Source: II. General Relativistic Effects" A&A **326** 99 (1997).

[193] F. J. Pineda, J. P. Delvaille, J. Huchra and M. Davis *I. A. U. Circ.* **3202** (1978).

[194] F. Ponge *Le Parti Pris des Choses* Gallimard: Paris, 1942.

[195] K. A. Pounds, T. J. Turner and R. S. Warwick "Rapid X-ray Variability of the Seyfert Galaxy MCG-6-30-15" MNRAS **221** 7 (1986).

[196] K. A. Pounds and W. N. Brandt "Steep Spectrum Seyfert Galaxies" *X-Ray Imaging and Spectroscopy of Cosmic Hot Plasmas Proceedings of an International Symposium on X-ray Astronomy, Waseda University* 209 (1996).

[197] J. Poutanen and A. C. Fabian "Spectral Evolution of Magnetic Flares and Time Lags in Accreting Black Hole Sources" MNRAS **306** L31 (1999).

[198] A. Ptak, R. Mushotzky, P. Serlemitsos, and R. Griffiths. "X-ray Variability as a Probe of Advection-Dominated Accretion in Low-Luminosity Active Galactic Nuclei" ApJ **501** L37. (1998)

[199] B. Punsly "Spectral Diagnostics of Blazar Central Engines II. Hydromagnetic Theory" ApJ **473** 178 (1996).

[200] D. M. Rawson, J. Bailey, and P. J. Francis "Neural Networks and the Classification of Active Galactic Nucleus Spectra" *Publications of the Astronomical Society of Australia* **13** 207 (1996).

[201] J. C. Raymond and B. W. Smith "Soft X-ray Spectrum of a Hot Plasma" ApJ **35** 419 (1977).

[202] J. C. Raymond, B. W. Cox and B. W. Smith "Radiative Cooling of a Low-Density Plasma" ApJ **204** 290 (1976).

[203] M. J. Rees "Black Hole Models for Active Galactic Nuclei" ARA&A **22** 471 (1984).

[204] M. J. Rees "Astrophysical Evidence for Black Holes" in *Black Holes and Relativity* R. Wald, Ed. Chandresekhar Memorial Conference, Dec. 1996.

[205] C. S. Reynolds, A. C. Fabian, K. Nandra, H. Inoue, H. Kunieda and K. Iwasawa "ASCA PV Observations of the Seyfert 1 Galaxy MCG-6-30-15: Rapid Variability of the Warm Absorber" MNRAS **227** 901 (1995).

[206] C. S. Reynolds and A. C. Fabian "Special Relativistic Effects on the Strength of the Fluorescent Kα iron line from Black Hole Accretion Disks" MNRAS **290** L1 (1997).

[207] C. S. Reynolds and A. C. Fabian "Warm Absorbers in Active Galactic Nuclei" MNRAS **273** 1167 (1995).

[208] C. S. Reynolds and M. Begelman "Iron Fluorescence from within the Innermost Stable Orbit of Black Hole Accretion Disks" ApJ **488** 109 (1997).

[209] C. S. Reynolds, M. J. Ward, A. C. Fabian and A. Celotti "A Multi-Wavelength Study of the Seyfert 1 Galaxy MCG-6-30-15" MNRAS **291** 403 (1997).

[210] C. S. Reynolds "An X-ray Spectral Study of 24 Type-1 Active Galactic Nuclei" MNRAS **286** 513 (1997).

[211] C. S. Reynolds, Ph. D. Thesis, Cambridge University, 1996.

[212] A. Robinson, E. Pérez and L. Binette "Broad Emission Lines in Active Galaxies: Horns, Bumps, and Shoulders" MNRAS **246** 349 (1990).

[213] R. Rosner, W. H. Tucker and G. S. Vaiana "Dynamics of the Quiescent Solar Corona" ApJ **220** 643 (1978).

[214] R. R. Ross and A. C. Fabian "The Effects of Photoionization on X-ray Reflection Spectra in Active Galactic Nuclei" MNRAS **261** 74 (1993).

[215] G. B. Rybicki and A. P. Lightman *Radiative Processes in Astrophysics* (John Wiley and Sons, New York: 1979).

[216] I. Salamanca D. Alloin, T. Baribaud, D. Axon, G. De Bruyn, M. Goad, P. Gondhalekar, E. Van Groningen, N. Jackson, W. Kollatschny, E. Laurikainen, A. Lawrence, J. Masegosa, P. O'Brien, D. Pelat, M. V. Penston, E. Perez, I. Perez-Fournon, A. Robinson, M. Santos-Lleo, G. M. Stirpe, C. Tadhunter, R. Terlevich, S. Unger, S. Wagner, and I. Wanders. "Spectroscopic monitoring of active galactic nuclei. 3: Size of the broad line region in NGC 3227" A&A **282** 742 (1994).

[217] J. L. R. Sara, J. T. Schmelz, A. K. Bhatia, and K. T. Strong. "Fe XVII Soft X-ray Lines: Theory and Data Comparisons" ApJ **510** 1064 (1999).

[218] R. F. Sawyer and D. J. Scalapino, Phys. Rev. D. **7** 953 (1972).

[219] R. A. Shafer "Spatial Fluctuations in the Diffuse Cosmic X-ray Background" Ph.D. Thesis, University of Maryland (1983).

[220] N. I. Shakura and R. A. Sunyaev "Black Holes in Binary Systems. Observational Appearance" A&A **24** 337 (1973).

[221] S. L. Shapiro and S. A. Teukolsky. *Black Holes, White Dwarfs, and Neutron Stars* (John Wiley and Sons, New York: 1983).

[222] N. I. Shakura and R. A. Sunyaev "A Theory of the Instability of Disk Accretion Onto Black Holes and The Variability of Binary X-ray Sources, Galactic Nuclei, and Quasars" MNRAS **175** 613 (1976).

[223] R. Sivron, D. Caditz and S. Tsuruta "Effects of Shocks on Emission from Central Engines of Active Galactic Nuclei I" ApJ **469** 542 (1996).

[224] R. Sivron and S. Tsuruta "Dense Clouds Near the Central Engine of Active Galactic Nuclei" ApJ **402** 420 (1993).

S.L. Snowden, M.J. Freyberg, P.P. Plucinsky, J.H.M.M. Schmitt, J. Truemper, W. Voges, R.J. Edgar, D. McCammon, W.T. Sanders, "First Maps of the Soft X-ray Diffuse Background from the *ROSAT* XRT/PSPC All-Sky Survey" ApJ **454** 643 (1995).

[225] H. Sponholz and D. Molteni "Steady State Shocks in Accretion Disks around a Kerr Black Hole" MNRAS **271** 233 (1994).

[226] R. Srianand and S. Shankaranarayanan "Probing the Broad-Line Regions in Active Galactic Nuclei Using Time Variability of Associated Absorption Lines" ApJ **518** 672 (1999).

[227] R. Srianand "High-Resolution Study of Associated C IV Absorption Systems in NGC 5548" ApJ **528** 617 (2000).

[228] L. Stella and R. Rosner. "Magnetic Field Instabilities in Accretion Disks" ApJ **277** 312 (1984).

[229] P. A. Sturrock *Plasma Physics: An Introduction to the Theory of Astrophysical, Geophysical and Laboratory Plasmas* (Cambridge University Press, Cambridge, 1994).

[230] J. W. Sulentic, P. Marziani and M. Calvani "Disk Models for MCG-6-30-15: The Variability Challenge" ApJ **497** (1998).

[231] R. S. Sutherland, G. V. Bicknell and M. A. Dopita "Shock Excitation of the Emission-Line Filaments in Centaurus A" ApJ **414** 510 (1993).

[232] R. Svensson "Models of X-ray and γ-ray Emission from Seyfert Galaxies" A&AS **120** 475 (1996).

[233] G. Tagliaferri, G. Bao, G. L. Israel, L. Stella and A. Treves "The Soft and Medium X-ray Variability of NGC 5548: A Reanalysis of EXOSAT Observations" ApJ **465** 181 (1996).

[234] T. Takahashi, M. Markevitch, Y. Fukazawa, Y. Ikebe, Y. Ishisaki, K. Kikuchi, K. Makishima, Y. Tawara and the ASCA analysis team "Extended Source Analysis with ASCA" (NASA: 1995).

[235] Y. Tanaka, K. Nandra, A. C. Fabian, H. Inoue, C. Otani, T. Dotani, K. Hayashida, K. Iwasawa, T. Kii, H. Kunieda, F. Makino and M. Matsuoka "Gravitationally Redshifted Emission Implying an Accretion Disk and Massive Black Hole in the Active Galaxy MCG-6-30-15" Nature **375** 659 (1995).

[236] M. Tashiro, Y. Fukazawa, E. Idesawa, Y. Ishisaki, H. Kubo, K. Makashima, Y. Ueda and the GIS team "GIS Status Report" (NASA: 1995).

[237] Tennant and Muschotzky, "The Absence of Rapid X-ray Variability in Active Galaxies" ApJ **264** 92 (1983).

[238] R. Terlevich and J. Melnick "A supernova in the nucleus of NGC5548?" Nature **333** 329 (1988).

[239] B. G. Tritz *Effects of Electron-Positron Pairs on Active Galactic Nuclei* Ph. D. Thesis, Montana State University (1990).

[240] S. Tsuruta "Some Recent Development in Problems of Quasars Like Objects" *Proceedings of the Third Marcel Grossmann Meeting on General Relativity* (1983).

[241] S. Tsuruta and M. Kellen "Disk-Corona Model of Active Galactic Nuclei with Nonthermal Pairs" ApJ **453** L9 (1995).

[242] T. J. Turner, I. M. George, K. Nandra and D. Turcan. "On the X-ray Variability in Seyfert Galaxies" ApJ **524** 667 (1999).

[243] T. J. Turner, I. M. George, K. Nandra and R. F. Mushotzky "ASCA Observation of type-2 Seyfert Galaxies: II The Importance of X-ray Scattering and Reflection" ApJ **493** 91 (1998).

[244] T. J. Turner and K. A. Pounds "The EXOSAT Survey of Emission Line AGN" Proc. 13 I.A.U. **134** p.155 (1988).

[245] M. L. G. Vargas, A. Diaz, R. Terlevich, and E. Terlevich "Testing the Consistency of the Starburst Scenario for Active Galactic Nuclei" *Astrophysics and Space Science* **205** 77 (1993).

[246] D. A. Verner, G. J. Ferland, K. T. Korista and D. G. Yakovlev "Atomic Data for Astrophysics II New Analytic Fits for Photoionization Cross Sections of Atoms and Ions" ApJ **465** 487 (1996).

[247] D. A. Verner and G. J. Ferland "Atomic Data for Astrophysics, I. Radiative Recombination Rates for H-like He-like, Li-like and Na-like ions over a Broad Range of Temperature" ApJS **103** 467 (1997).

[248] S. U. Viergutz "Radiation from Arbitrarily Shaped Objects in the Vicinity of Kerr Black Holes" *Astrophysics and Space Science* **205** 155 (1993).

[249] S. J. Wagner "Coronal Lines from BLR, NLR, and ENLR' *ASP Conf. Ser. 113: IAU Colloq.Emission Lines in Active Galaxies: New Methods and Techniques* **159** 298 (1998).

[250] A. Wandel "Spectral Dependence of the Broad Emission Line Region in Active Galactic Nuclei" ApJ **490** 131 (1997).

[251] A. Wandel, B. M. Peterson and M. A. Malkan. "Central Masses and Broad-Line Region Sizes of Active Galactic Nuclei I. Comparing the Photoionization and Reverberation Techniques" ApJ **526** 579 (1999).

[252] A. Wandel "The Black Hole-to-Bulge Mass Relation in Active Galactic Nuclei" ApJ **519** L39 (1999).

[253] I. Wanders and B. M. Peterson "A Long-Term Study of Broad Emission Line Profile Variability in NGC 5548" ApJ **466** 174 (1996).

[254] T. Wang, Y. Lu and Y. Zhou "Emission Line and Ultraviolet to X-ray Continuum Correlations: Constraints on the Anisotropy of the Ionizing Continuum in Active Galactic Nuclei" ApJ **493** 1 (1998).

[255] K. A. Weaver, J. H. Krolik and E. A. Pier "Detecting Compton Reflection and a Broad Iron Line in MCG 5-23-16 with RXTE" *Proceedings of the American Astronomical Society Meeting Dec. 1997* **191** 9003 (1997).

[256] K. A. Weaver and C. S. Reynolds. "Are the Nuclei of Seyfert 2 Galaxies Viewed Face-On?" ApJ **503** L39 (1998).

[257] D. W. Weedman "Seyfert Galaxies" ARA&A **15** 69 (1977).

[258] R. Wehrse, H. H. Störzer and G. Shaviv "The Vertical Structure and Radiation Fields of Accretion Disks in the Centres of AGN's" *Astrophysics and Space Science* **205** 163 (1992).

[259] T. R. White, A. P. Lightman, and A. A. Zdziarski. "Compton Reflection of Gamma Rays by Cold Electrons" ApJ **331** 939 (1988).

[260] B. J. Wilkes, P. J. Green, S. Mathur and J. C. McDowell "Emission Lines and the Spectral Energy Distributions of Quasars" In **Proceedings of the IAU Colloquium 159: Emission Lines in Active Galaxies: New Methods and Techniques** (1997).

[261] C. Winge, D. J. Axon, F. D. Macchetto, and A. Cappetti. "The Narrow-Line Region of NGC 4151: A Turbulent Cauldron" ApJ **487** L121 (1997).

[262] V. Woolf **Orlando** Harcourt, Brace, and World. New York: 1928.

[263] T. Yaqoob, B. McKernan, A. —tak, K. Nandra and P. J. Selemitsos "A Simple New Method for Analysing Gapped Time-Series: Search for High-Frequency Cut-off in the X-ray Power Spectrum of the Seyfert Galaxy MCG-6-30-15" ApJ **490** 25 (1997).

[264] A. A. Zdziarski, W. N. Johnson and P. Magdziarz "Broad-band gamma-ray and X-ray spectra of NGC 4151 and their implications for physical processes and geometry" MNRAS **283** 193 (1996).

[265] M. V. Zombeck *Handbook of Space Astronomy and Astrophysics, 2nd Edition* Cambridge University Press, Cambridge: 1990.

[266] Y. Y. Zhou, K. N. Yu, E. C. M. Young, J. M. Wang and E. Ma "Statistical Properties of the Big Blue Bump in Active Galactic Nuclei" ApJ **475** L9 (1997).

APPENDICES

APPENDIX A

XSPEC MODELS AND STATISTICS

This Appendix is a supplement for Chapter 3, and describes each of the models (from XSPEC or otherwise) used for data analysis. In addition, the main statistical techniques used to evaluate the goodness of fit of the models are described.

Hard X-ray Continuum

In the context of ASCA observations, hard X-rays mean those above 2 keV, which are minimally affected by the presence of the interstellar medium. Seyfert galaxies usually exhibit a powerlaw continuum, iron Kα features and in some cases the low-energy end of the compton reflection hump. This section describes the XSPEC models used to model the powerlaw continuum and (in some cases) the compton reflection hump.

The simplest model for the X-ray continuum is a powerlaw distribution:

$$f(\varepsilon) = Ae^{-\Gamma\varepsilon} \tag{A.1}$$

where A is the normalization of the distribution in Counts $keV^{-1}cm^{-2}s^{-1}$ at 1.0 keV and Γ is the photon index of the spectrum.

An alternative model of the powerlaw continuum is the broken powerlaw, which has no *a priori* physical justification, but is often useful in establishing changes in spectral shape. This model has the functional form:

$$f(\varepsilon) = Ae^{-\Gamma_1\varepsilon} \quad \varepsilon < \varepsilon_{break}$$

$$f(\varepsilon) = Ae^{-\Gamma_2\varepsilon} \quad \varepsilon > \varepsilon_{break}$$

for which ε_{break} is the energy at which the photon index changes, Γ_1 is the photon index below the break, and Γ_2 is the photon index above the break

If the nonthermal radiation from the central engine originates in the corona and is reflected off a disk, we would expect that a model describing the reflection component would more accurately describe the data. Photons reflected from an AGN accretion disk have a finite probability of undergoing a Compton reflection and being reemitted at a different energy. For an infinite, plane-parallel geometry, photons obey the transport equation (Lightman and White, 1988):

$$\frac{1}{c}\frac{\partial W}{\partial t} = -\kappa(x)\rho W \tag{A.2}$$

where W is the probability that a photon with initial energy x_0 has reached energy x without being absorbed, κ is the opacity and ρ the density of the accretion disk material. The continuum spectrum has an approximate analytical form of:

$$W(x, x_0) = exp\Big[C\Big(\frac{1}{4x_0^4} - \frac{1}{4x^4}\Big)\Big] \tag{A.3}$$

where C=10^{-5} is a constant resulting from the integration, and assumes cosmic abundances in the material. This equation is valid for low states of ionization, and assumes an isotropic source.

Exponentially cut-off power-law spectrum reflected from neutral material. See Magdziarz and Zdziarski(1995) for details. The output spectrum is the sum of the cutoff power law and the reflection component. The model can be used to obtain the reflection component (parameter *rel_refl* in XSPEC, which is often called ϵ in publications and in tables in this work). Within XSPEC, the reflection component alone can be obtained by setting $rel\_refl < 0$. The normalization of this component is just the scaling factor $|rel\_refl|$; if this is done, the user should ensure that 0 is not within the included range of the parameter. If $E_c = 0$, there is no cutoff in the power law. Version with variable iron abundance and new opacities of Balucinska and McCammon (1992, and 1994, private communication). As expected in AGNs, H and He are assumed to be fully ionized. For this model, Γ is the photon index, E_c the cutoff energy in keV, ϵ the scaling factor for reflection, z the redshift, q the iron abundance relative to solar, $\cos\theta$ the cosine of the inclination angle of the reflective material relative to the observer, and n the photon flux at 1 keV of the powerlaw in the observed frame.

Multifrequency observations of Seyfert 1 galaxies have indicated that several candidates are substantially reddened (Reynolds, 1997)(Reynolds and Fabian, 1995).A simple model for the inclusion of dust in the soft X-ray continuum is available as the XSPEC model plabs, which has the form:

$$f_{out}(\varepsilon) = f_{in}(\varepsilon)Ae^{-\alpha} \tag{A.4}$$

where A is a normalization factor and α is the index of the dust.

If the cold disk at the center of an AGN is surrounded by a hot plasma, it is equally likely that part of the continuum reaching the observer will be absorbed by this medium. Two media are likely to cause this absorption: gas and dust. A simple model for absorption of the continuum by gas is:

$$f_{out}(\varepsilon) = f_{in}(\varepsilon)(N_h e^{-\epsilon * \sigma(\varepsilon)} + 1 - \epsilon) \tag{A.5}$$

where N_h is the equivalent hydrogen column in units of 10^{22} atoms per cm^2 and ϵ is a covering factor of the continuum source by the gas. This model corresponds to the XSPEC model pcfabs for solar-abundance gases.

For comparison the six models for the photon index are shown in Figure A1 for an inclination angle of $\theta = 0$. The difference between the broken powerlaw and simple photon index is self-evident, whereas the main differences between the simple photon index and the partial reflection models occurs at high energies just below the highest energy detected by ASCA. The partially absorber powerlaw does not present any difference from the simple photon index at high energies and cannot be distinguished from models which involve variation of the warm absorber at soft energies.

Soft X-ray Continuum Models

For the more luminous Seyfert 1 galaxies, the spectrum below 2 keV typically includes absorption by the interstellar medium, absorption by O VII and O VIII, and an O VI emission line. Photons with energies below 2 keV experience absorption by the interstellar medium and absorption and emission by the plasma near the center of the AGN.

Photons from an AGN must travel through the interstellar medium (ISM) and the

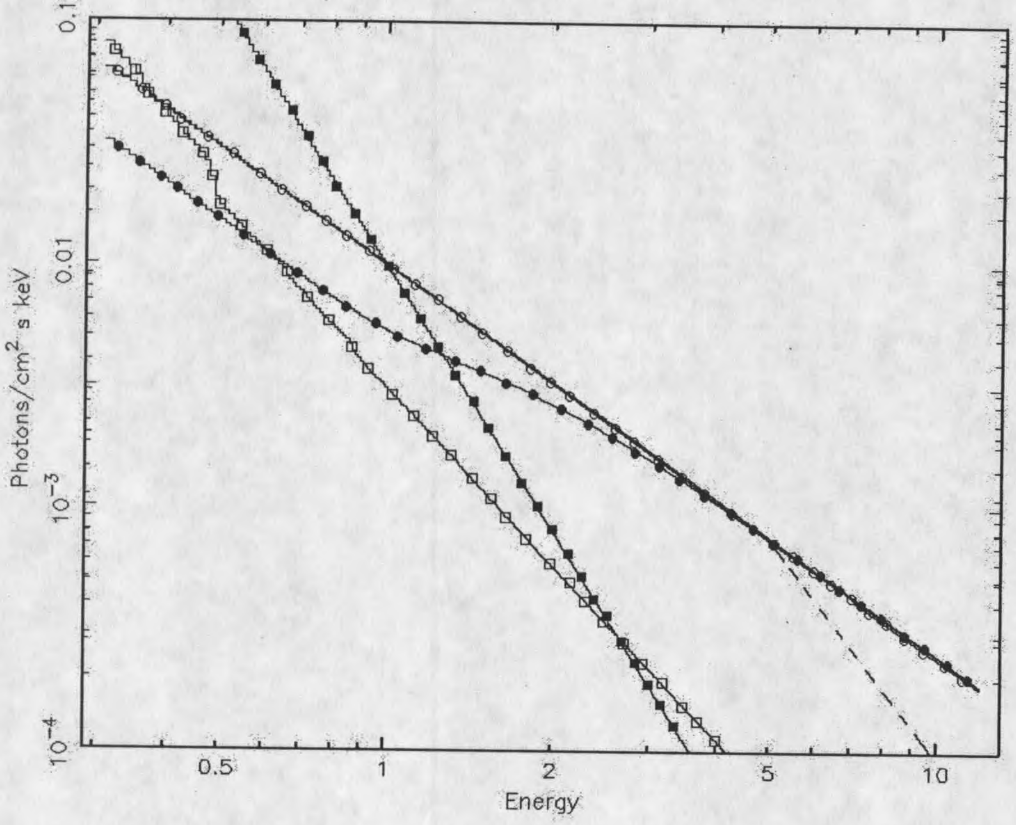

Figure A.1: Models of the Hard Continuum Spectrum; all have the same primary photon index, with other parameters adjusted to demonstrate spectral differences. Solid line: simple powerlaw, dashed line: broken powerlaw, filled squares: partial absorption by dust, filled circles: partial covering by gas, open circles: partial reflection from neutral material, open squares: partial reflection from ionized material.

portion of our galaxy in the line of site before reaching the vicinity of earth. Most of the absorption occurs within our galaxy, and is measured by radio techniques. The model used for galactic hydrogen in this work is:

$$I(\varepsilon) = I_o(\varepsilon)e^{N_h\sigma(\varepsilon)} \tag{A.6}$$

where $\sigma(\varepsilon)$ is the photon capture cross section of the interstellar medium (ISM) and N_h is the column density of the ISM in units of cm^2.

Many Seyfert 1 galaxies exhibit absorption and emission features due further ionization of the coronal and broadline plasmas. Three absorption edges are typically associated with ASCA spectra. The Fe K absorption edge energy varies from 7.1 keV for Fe I to 9.3 keV for Fe XXVI, so that the redshift-corrected edge energy indicates the ionization state of the iron on the cold disk. In most ASCA observations of Seyfert galaxies we see absorption edges due to ionized O VII and O VIII. These have the same functional form as the iron absorption edge, but correspond to energies of 0.721 keV for O VII and 0.871 keV for O VIII (Verner and Ferland, 1997).

The model used in fitting absorption edges has the form:

$$m(\varepsilon) = e^{\frac{-\varepsilon\tau}{\varepsilon_{edge}}} \quad \varepsilon \geq \varepsilon_{edge}$$

$$m(\varepsilon) = 1 \qquad \varepsilon < \varepsilon_{edge}$$

where τ is the depth of the absorption edge and ε_{edge} is the lowest energy at which photons are absorbed by the atomic process of interest. The denotation $m(\varepsilon)$ indicates that this model is multiplied by, rather than added to, other components of the continuum spectrum.

The edge depth is related to the photoionization cross section σ of the species i by (Rybicki and Lightman, 1979):

$$\tau_i = \frac{1}{\hbar}\int_{z_0}^{z} \sigma n_i d\varepsilon \tag{A.7}$$

where n_i is the number density of species i.

While ASCA does not have good effective area below 0.6 keV, we expect to find two recombination lines, one at 0.653 keV which corresponds to O VIII and another at 0.568 keV, corresponding to O VII. The ionized oxygen is thought to exist in the warm absorber, possibly in the broadline clouds. These features are fit with extremely narrow-width gaussian line profiles, since ASCA does not have adequate energy resolution to determine if the profiles experience any gravitational redshift.

Statistical Techniques

Spectra from ASCA observations are analyzed using the software package XSPEC. It uses several statistics to evaluate the goodness of fit, which are documented here.

The most common statistic to compare two binned curves of any variety in astrophysics is the χ^2 test. Consider two samples with equal numbers of points n. The first sample has points with value x_i and the second sample has an ith point with value y_i. The chi-square statistic is then:

$$\chi^2 = \sum \frac{(y_i - x_i)^2}{y_i} \tag{A.8}$$

In the context of analysis by XSPEC, the x_i are the points in the ASCA observation and the y_i are the values predicted by the model being tested.

APPENDIX B

SUPPLEMENTARY IMAGE AND LIGHT CURVE DATA

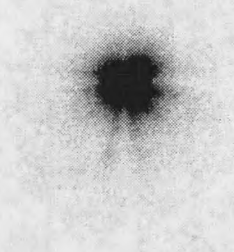

Figure A.2: GIS3 Image of MCG-6-30-15 over the course of the entire observation.

Image Analysis of MCG-6-30-15

This appendix contains images and light curves important for the analysis of MCG-6-30-15 which are important for the analysis, but are too page intensive to include in the main body of the text. The GIS3 image of the source is as shown in Figure A.2.

Light curves of MCG-6-30-15

The light curve for the full observation of MCG-6-30-15 is shown in Figure A.3. The four hardness ratios (which were defined in Chapter 3) are shown in Figures A.4 through A.7. These figures are presented here to supplement the discussion in Chapter 5.

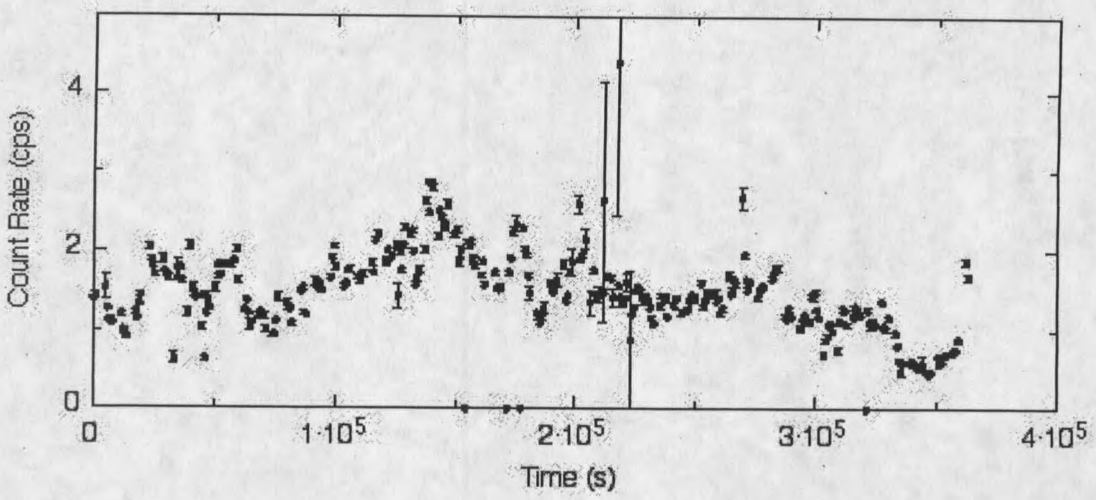

Figure A.3: Light curve for MCG-6-30-15; total counts.

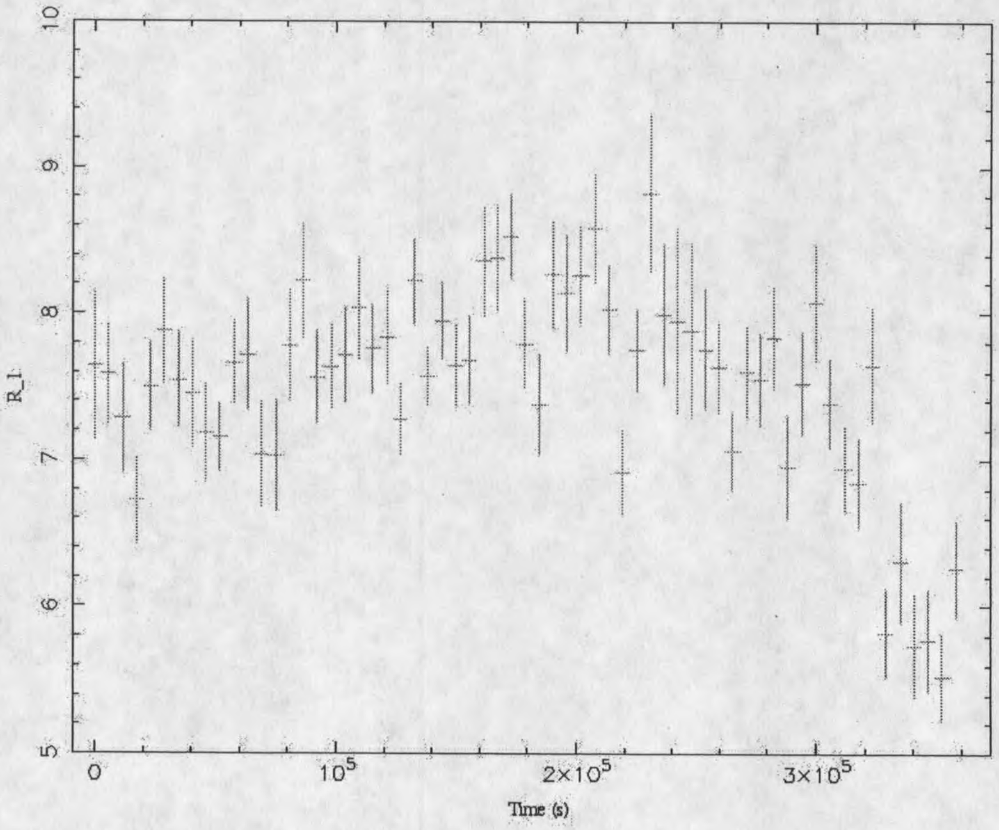

Figure A.4: R_1 vs time for MCG-6-30-15; note that hardness ratios do not have units.

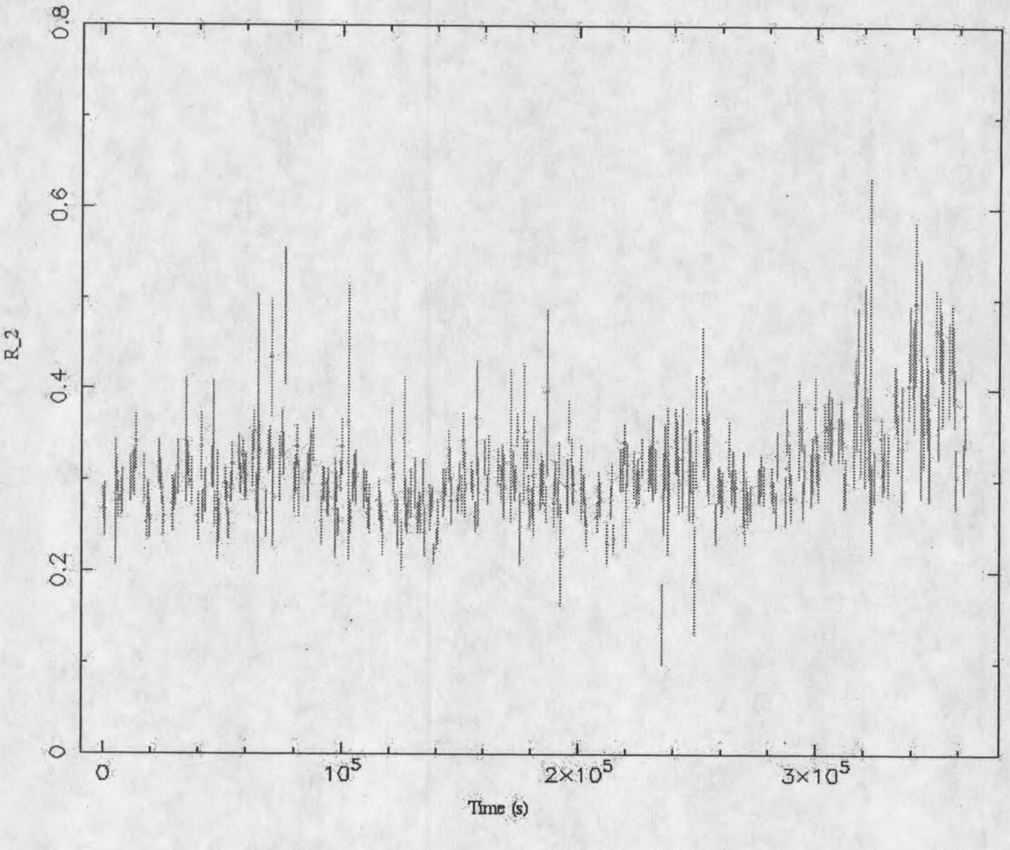

Figure A.5: R_2 vs time for MCG-6-30-15; hardness ratios are dimensionless quantities.

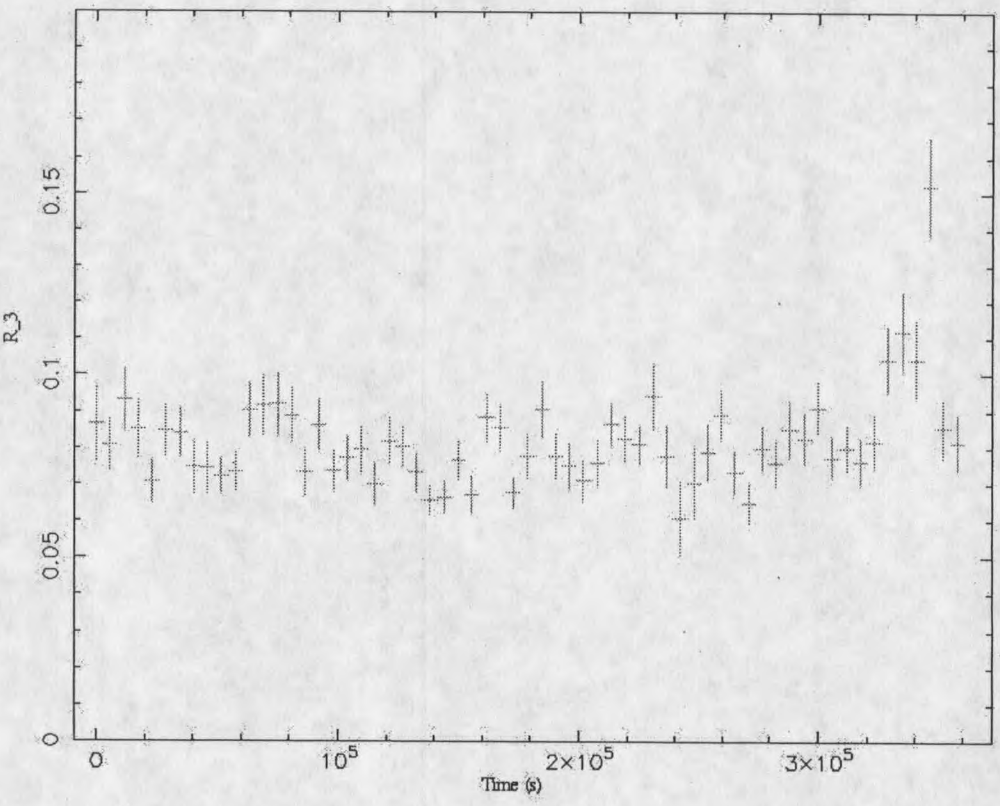

Figure A.6: R_3 vs time for MCG-6-30-15; hardness ratios are dimensionless quantities.

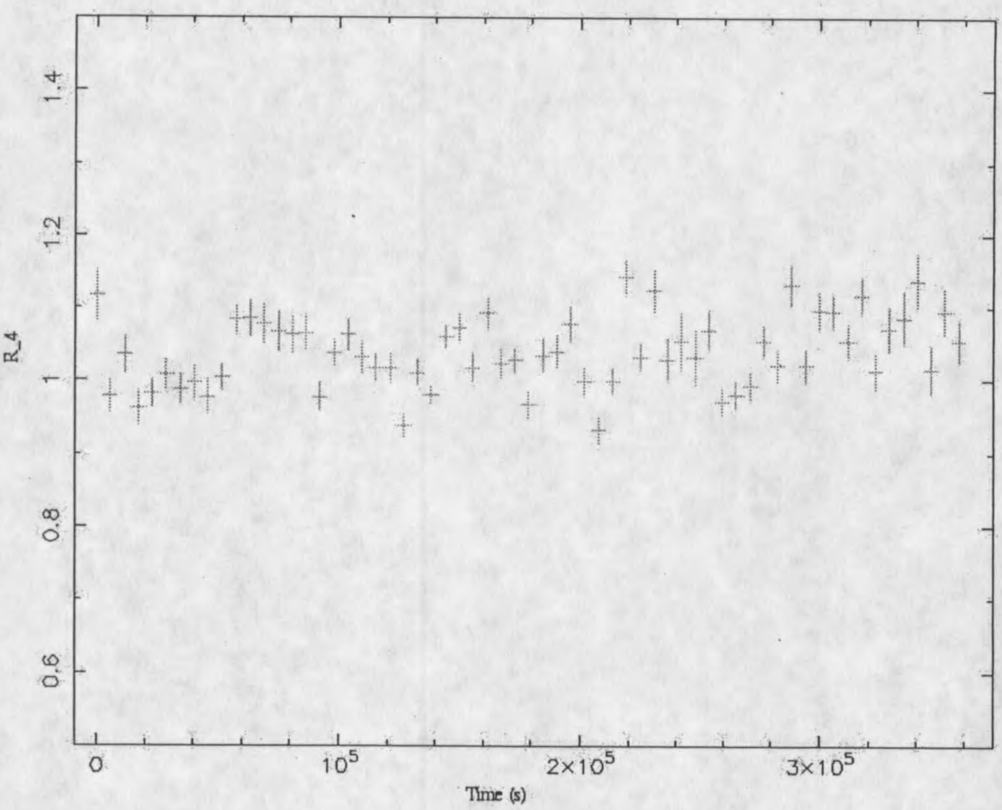

Figure A.7: R_4 vs time for MCG-6-30-15; hardness ratios ard dimensionless quantities.

Data Set	Γ_1	ε_{break}	Γ_2	χ^2	d.o.f.
constant	$1.73^{+0.14}_{-0.14}$	$6.25^{+0.59}_{-0.52}$	$2.83^{+0.61}_{-0.53}$	360.9	374
decrease	$1.86^{+0.12}_{-0.12}$	$9.0_{-2.5}$	2.7	348.9	390
fall	$1.77^{+0.14}_{-0.14}$	$6.4^{+0.8}_{-0.5}$	$2.82^{+0.74}_{-0.55}$	339.9	368
flare	$1.74^{+0.14}_{-0.14}$	$6.3^{+0.5}_{-0.4}$	$3.12^{+0.66}_{-0.56}$	356.3	375
increase	$1.83^{+0.13}_{-0.14}$	$6.8^{+2.2}_{-0.9}$	$2.51^{+0.91}_{-0.75}$	306.3	365
jump	$1.66^{+0.14}_{-0.15}$	$6.0^{+0.6}_{-0.4}$	$2.62^{+0.46}_{-0.41}$	424.5	415
spring	$1.82^{+0.15}_{0.15}$	$6.8^{+1.3}_{-0.7}$	$2.90^{+1.03}_{-0.84}$	338.5	320
trip	$1.79^{+0.15}_{-0.15}$	$9.0_{-0.7}$	8.60	294.5	243
well	$1.87^{+0.14}_{-0.14}$	$9.0_{-1.6}$	6.03	292.5	279
wobble	$1.68^{+0.19}_{-0.20}$	$6.6_{-0.7}$	$2.62^{+1.18}_{-0.96}$	219.0	208

Table A.1: Broken Photon Indices for Method C Data. Confidence regions shown are 3σ; confidence regions for Γ_2 are omitted when they exceed the soft limits for that parameter.

Spectral Analysis of MCG-6-30-15

Alternate models of the continuum spectrum are explored next. The broken powerlaw model was examined first, since it can indicate more subtle continuum changes without assigning them to either reflection or absorption. However, the model can only indicate trends in the data, and does not correspond directly to underlying physical changes in the data. The best-fit parameters for the broken powerlaw model for the Method C data is shown in Table A.1.

This dataset is consistent with a constant lower photon index Γ_1 with a value near 1.8; the dataset "jump" has a photon index lower than $\Gamma_{ave} = 1.88$ to 3σ significance. Five of the eight datasets for which have a measurable confidence region for Γ_2 have $\Gamma_2 > \Gamma_1$ to 3σ significance, although seven of the datasets have break energies within the iron line region. These data are consistent with the existence of a high-energy reflection hump, but due to the proximity of ϵ_{break} to the iron emission line none

Data Set	Γ_1	ε_{break}	Γ_2	χ^2	d.o.f.
ab1	$1.83^{+0.07}_{-0.07}$	$8.4^{+0.3}_{-0.3}$	10.0	220.9	244
a2	$1.99^{+0.05}_{-0.05}$	$9.0_{-0.4}$	$-1.3^{+4.2}$	317.7	372
a3	$2.03^{+0.05}_{-0.05}$	$9.0_{-0.4}$	$-1.3^{+5.2}$	399.7	398
a4	$2.09^{+0.06}_{-0.06}$	$8.6_{-1.4}$	$3.4^{+4.6}_{-3.1}$	277.3	307
b2	$1.85^{+0.06}_{-0.06}$	$9.0_{-0.7}$	-0.07	334.2	318
b3	$1.97^{+0.06}_{-0.06}$	$9.0_{-0.5}$	$-0.3^{+6.3}$	305.5	324
b4	$2.01^{+0.09}_{-0.09}$	$5.0^{+2.3}$	$1.64^{+0.28}_{-0.24}$	163.9	224
c1	$1.82^{+0.08}_{-0.08}$	$8.5^{+0.4}_{-0.3}$	$10.0_{-4.7}$	209.3	204
c2	$1.85^{+0.06}_{-0.06}$	$9.0_{-0.3}$	$-3.0^{+6.3}$	206.6	296
c3	$1.88^{+0.21}_{-0.13}$	$10.0_{-1.9}$	9.6	251.2	248
c4	$1.93^{+0.16}_{-0.16}$	5.0	$1.77^{+0.33}_{-0.42}$	70.71	124
d1	$1.65^{+0.05}_{-0.05}$	$8.9_{-0.3}$	$10.0_{-4.3}$	340.6	372
d1a	$1.61^{+0.09}_{-0.09}$	$5.0^{+1.7}$	$1.98^{+0.25}_{-0.22}$	216.8	240
d1b	$1.63657^{+0.17}_{-0.18}$	$9.3_{-0.8}$	-2.8	245.1	195
d2	$1.73^{+0.09}_{-0.09}$	$6.6^{+0.9}_{-0.9}$	$2.99^{+0.84}_{-0.70}$	208.9	197
d34	$1.92^{+0.09}_{-0.08}$	$9.0_{-0.6}$	-3.0	191.7	188

Table A.2: Broken Photon Indices for Method D Data. Confidence regions shown are 1σ; confidence regions for Γ_2 are omitted when they exceed the soft limits for that parameter.

provides conclusive evidence for the presence of that feature.

Finally, the best-fit parameters for the broken powerlaw model fit to the datasets extracted by Method D as shown in Table A.2.

This dataset exhibits significant differences in the low-energy photon index Γ_1 which are not clearly related to the value of the break energy. Unlike the other datasets only two of the datasets from this group show high-energy indices which are significantly higher than the low energy index. Most datasets have break energies above 8 keV, suggesting that some feature exists there, but many datasets have $\Gamma_2 < 0$.

One possible physical basis for a deviation from the continuum is that the continuum radiation is partially reflected from neutral gas in the line of sight. This

Data Set	Γ	α	χ^2	d.o.f.
constant	$1.82^{+0.17}_{-0.16}$	$0.22^{+0.17}_{-0.16}$	208.1	215
decrease	$1.76^{+0.16}_{-0.15}$	$0.16^{+0.16}_{-0.15}$	179.1	226
fall	$1.84^{+0.18}_{-0.17}$	$0.24^{+0.10}_{-0.17}$	187.0	207
flare	$1.85^{+0.17}_{-0.16}$	$0.25^{+0.17}_{-0.16}$	221.3	211
increase	$1.78^{+0.18}_{-0.16}$	$0.18^{+0.17}_{-0.16}$	197.6	209
jump	$1.77^{+0.16}_{-0.15}$	$0.17^{+0.15}_{-0.15}$	231.3	238
spring	$1.82^{+0.19}_{-0.17}$	$0.22^{+0.19}_{-0.17}$	183.0	179
trip	$1.76^{+0.22}_{-0.20}$	$0.16^{+0.22}_{-0.16}$	177.9	136
well	$1.82^{+0.22}_{-0.19}$	$0.22^{+0.22}_{-0.20}$	153.6	151
wobble	$1.77^{+0.25}_{-0.23}$	$0.17^{+0.25}_{-0.17}$	102.7	114

Table A.3: Absorption by Dust for Method C Data. Confidence regions shown are 3σ.

possibility is modelled using the native XSPEC model "pexrav", which is described in Chapter 3.

The alternative to reflection of the continuum off gas is that the continuum is partially absorbed by gas or dust along the line of sight of the galaxy. The possibility of absorption of the continuum by dust is modelled by the native XSPEC model "plabs", which was previously described in Chapter 3. This model produced better fitting statistics for the average spectrum of the complete observation than did the simple powerlaw model or the partial reflection model. In this analysis two goals are intended; first, to determine whether the dust index α is significantly different from zero which would provide further evidence that the continuum undergoes partial absorption by a column of dust and second, to find determine whether either the photon index Γ or the dust index α vary between datasets.

The model for absorption by dust was also fit to the data selected using Method C (three-point derivative classification), with best-fit parameters shown in Table A.3.

Data Set	Γ	α	χ^2	d.o.f.
ab1	$1.83^{+0.25}_{-0.22}$	$0.24^{+0.25}_{-0.22}$	117.3	118
a2	$1.87^{+0.19}_{-0.17}$	$0.27^{+0.18}_{-0.17}$	155.9	202
a3	$1.81^{+0.17}_{-0.16}$	$0.21^{+0.18}_{-0.16}$	233.5	228
a4	$1.87^{+0.24}_{-0.22}$	$0.27^{+0.24}_{-0.22}$	159.0	149
b2	$1.71^{+0.21}_{-0.19}$	$0.11^{+0.21}_{-0.11}$	168.0	161
b3	$1.92^{+0.22}_{-0.19}$	$0.17^{+0.22}_{-0.17}$	162.7	163
b4	$1.69^{+0.29}_{-0.26}$	$0.092^{+0.29}_{-0.092}$	87.57	125
c1	$1.84^{+0.32}_{-0.27}$	$0.24^{+0.32}_{-0.24}$	84.91	97
c2	$1.77^{+0.32}_{-0.19}$	$0.17^{+0.32}_{-0.17}$	94.78	144
c3	$1.85^{+0.24}_{-0.21}$	$0.25^{+0.24}_{-0.25}$	124.8	119
c4	$1.75^{+0.62}_{0.45}$	$0.15^{+0.62}_{-0.15}$	26.78	75
d1	$1.71^{+0.17}_{-0.16}$	$0.12^{+0.17}_{-0.12}$	208.6	204
d1a	$1.68^{+0.24}_{-0.21}$	$0.078^{+0.236}_{-0.078}$	103.4	117
d1b	$1.70^{+0.30}_{-0.26}$	$0.10^{+0.30}_{-0.10}$	116.3	99
d2	$1.80^{+0.34}_{0.29}$	$0.21^{+0.34}_{-0.21}$	100.1	92
d34	$1.75^{+0.35}_{-0.29}$	$0.15^{+0.35}_{-0.15}$	105.5	86

Table A.4: Absorption by Dust for Method D Data. Confidence regions shown are 3σ.

All of these data are consistent with a constant photon index with either the value $\Gamma = 1.88$ found for the simple powerlaw model or for the value $\Gamma = 1.72$ found for the dust absorption model of the average continuum spectrum. Eight of the ten datasets shown here show significant absorption of dust to 3σ significance; all ten of the datasets are consistent with a constant absorption coefficient of $\alpha = 0.14$.

Finally, we explore the possibility that the properties of the dust absorption vary with the average hardness of the spectra. The best-fit parameters of the dust absorption model for the Method D datasets are as shown in Table A.4.

The photon indices of this model are within the 3σ confidence limits of one another; all the data are consistent with both the photon index found using the dust absorption model of the observation as well as with that of the simple powerlaw model. One can note that the only datasets which have $\alpha > 0$ to 3σ confidence are the high luminosity datasets a2, a3, and a4. We may thus conclude that absorption by dust is significant for the high luminosity portions of the light curve. The data are all consistent with the model of the continuum of the entire observation, which has significant absorption by dust with index $\alpha = 0.14$. Another noteworthy characteristic of these data are that the goodness of fit statistics for this model are noticeably worse than for other models of the continuum; seven of the thirteen main datasets and one of the two subdivision (d1a) fail to meet the criterion that $\chi^2/d.o.f. < 1$.

None of the methods of analysis show any variation of the continuum, or of the absorption index of dust within the line of sight of MCG-6-30-15. However, most of the data show a $\alpha > 0$ to within 3σ confidence, so we conclude that dust is present within line of sight of MCG-6-30-15, but its physical characteristics do not vary at levels measurable by ASCA.

Next, we explore the possibility that the continuum of MCG-6-30-15 undergoes partial absorption by gas in the line of sight of the observation. Since the two parameters defining absorption by gas are interdependent, many trials determined that the column density of gas N_h and the covering fraction ϵ cannot both be measured with any degree of confidence for the lower-resolution spectra resulting from the selection methods described in Chapter 5, the method of fitting the data with the covering fraction frozen to $\epsilon = 0.5$ was adopted. The best-fit parameters for the average spectrum using this method are shown in Table A.5

This model for the average spectrum shows both a photon index and a neutral

$\Gamma = 1.915^{+0.045}_{0.044}$
$N_h = 0.52^{+0.35}_{-0.34}$
$\chi^2 = 436.0$
d.o.f. $= 508$

Table A.5: Best-fit parameters for a modified partial absorption model for the average spectrum. Errors shown are 3σ for the photon index and 1σ for N_h.

Data Set	Γ	N_h	χ^2	d.o.f.
constant	$2.24^{+0.18}_{-0.17}$	3.5	206.3	217
decrease	$1.98^{+0.16}_{-0.15}$	$1.0^{+2.5}_{-1.5}$	182.7	229
fall	$2.08^{+0.18}_{-0.16}$	$0^{+2.4}$	190.2	210
flare	$2.29^{+0.17}_{-0.16}$	$3.4^{+3.9}_{-2.6}$	222.2	215
increase	$2.20^{+0.17}_{-0.16}$	$4.6^{+5.2}_{-3.0}$	196.8	212
jump	$2.26^{+0.16}_{-0.15}$	$5.3^{+5.6}_{-3.1}$	236.6	240
spring	$2.23^{+0.19}_{-0.17}$	$3.5^{+4.6}_{-2.9}$	183.4	182
trip	$1.91^{+0.21}_{0.19}$	$0.0^{+2.9}$	182.2	139
well	$2.13^{+0.22}_{-0.20}$	$1.1^{+3.4}_{-1.1}$	153.3	152
wobble	$1.99^{+0.26}_{-0.23}$	$0.7^{+4.0}_{-0.7}$	102.6	114

Table A.6: Partial absorption by Gas for Method C data. Confidence regions shown are 1σ.

hydrogen column within 3σ confidence regions of the values determined initially. The 3σ confidence region of the hydrogen column did not exclude the possibility that no absorbing gas is present in the line of sight, so the 1σ confidence region is shown here.

Next the data selected by Method C are examined; with best-fit parameters shown in Table A.6; the corresponding best-fit data for Method D are shown in Table A.7. Several of these datasets have photon indices which differ significantly from that of the average spectrum. All datasets which have significantly differing photon indices also have column densities which are significantly different from zero.

The effective column density of the gas, which in this case is a measure of both the column density N_h and the escape fraction ϵ, varies significantly among the datasets.

Data Set	Γ	N_h	χ^2	d.o.f.
ab1	$2.56^{+0.24}_{-0.22}$	$14.20^{+22.6}_{-9.75}$	116.1	121
a2	$2.30^{+0.18}_{-0.16}$	$2.43^{+3.31}_{-2.38}$	159.2	211
a3	$2.04^{+0.16}_{-0.15}$	$0.48^{+2.33}_{0.48}$	236.7	239
a4	$2.11^{+0.22}_{-0.19}$	$0.03^{+2.30}_{-0.03}$	167.6	157
b2	$1.90^{+0.19}_{-0.17}$	$1.23^{+3.14}_{-1.23}$	169.5	169
b3	$1.92^{+0.19}_{-0.18}$	$0^{+2.69}$	176.3	171
b4	$1.78^{+0.27}_{-0.24}$	$0^{+3.86}$	88.02	118
c1	$2.57^{+0.29}_{-0.26}$	$14.7^{+30.8}_{-11.3}$	88.04	102
c2	$2.03^{+0.22}_{-0.20}$	$0^{+2.95}$	107.5	150
c3	$2.10^{+0.27}_{-0.23}$	$0.03^{+3.76}_{-0.03}$	128.9	125
c4	$1.98^{+0.52}_{-0.41}$	$0^{+8.29}$	30.46	77
d1	$2.25^{+0.17}_{-0.15}$	$7.71^{+7.75}_{-3.91}$	213.3	213
d1a	$2.22^{+0.23}_{-0.21}$	$8.48^{+18.1}_{-5.47}$	107.5	122
d1b	$2.26^{+0.29}_{-0.25}$	$9.02^{+34.0}_{-6.62}$	121.9	104
d2	$2.06^{+0.30}_{-0.26}$	$1.61^{+5.81}_{-1.61}$	103.3	97
d34	$2.00^{+0.31}_{-0.27}$	$1.90^{+6.37}_{-1.90}$	107.2	90

Table A.7: Partial absorption by Gas for Combined Luminosity and Hardness Data. These data were fit with an escape fraction frozen to ϵ=0.5 to avoid unrealistic error estimate for spectra with low N_h. Confidence regions shown are 3σ.

In particular, the datasets ab1, a2, c1, and d1 (and both subsets) have column densities of gas above 0 to 3σ significance. Many datasets have differing column densities of dust to 3σ significance; in particular, d1 has higher column density of gas than datasets c2,c3, b3, a4, and a3. Dataset b4 has lower column density than d1 to 1σ significance, and both datasets c4 and d34 are consistent with a zero column density and have fewer counts than do most other datasets. This suggests that the continuum during the deep minimum is absorbed by a larger amount of gas than the local maxima earlier in the observation. In addition, we see the first evidence for variation of the photon index for this dataset; we note that those datasets with the highest densities of absorption by gas also have the highest photon indices.

We must thus examine the possibility that the variations in this model result from

Data Set	O VII	O VIII	$L_x(10^{42} erg/s)$	χ^2/dof
flare	$\varepsilon = 0.723^{+.008}_{-.012}$	$\varepsilon = 0.867^{\pm 0.056}$	15.00	0.9389
jump	$\varepsilon = 0.724^{+0.008}_{-0.019}$	$\varepsilon = 0.891^{+0.056}_{-0.062}$	11.63	1.061
trip	$\varepsilon = 0.709^{+0.09}_{-0.019}$	$\varepsilon = 0.891^{+0.059}_{-0.07}$	10.93	1.130
well	$\varepsilon = 0.725^{+0.011}_{-0.022}$	$\varepsilon = 0.843^{+0.174}_{-0.843}$	11.34	1.141
con	$\varepsilon = 0.717^{+0.010}_{-0.016}$	$\varepsilon = 0.872^{+0.055}_{-0.046}$	10.01	1.123
dec	$\varepsilon = 0.720^{+0.009}_{-0.014}$	$\varepsilon = 0.890^{+0.0064}_{-0.0074}$	11.88	1.012
fall	$\varepsilon = 0.724^{+0.011}_{0.019}$	$\varepsilon = 0.862^{+0.063}_{-0.062}$	11.22	1.052
inc	$\varepsilon = 0.726^{+0.009}_{-0.014}$	$\varepsilon = 0.867^{+0.104}_{-0.199}$	11.82	1.079
spring	$\varepsilon = 0.723^{+0.010}_{-0.015}$	$\varepsilon = 0.891^{+0.054}_{-0.056}$	11.63	1.021

Table A.8: For both O VII and O VIII the best-fit energy and optical depth are shown.

the response function of ASCA and fitting algorithm used by XSPEC. The steep inclination angle of the ellipses which represent the confidence contours indicates that the two parameters increase each other when both are fit simultaneously. The large values for absorption column occur, in virtually every case, for datasets which also have significantly higher photon indices than the reference $\Gamma_{ave} = 1.88$. The result that partial absorption occurs significantly for at least some datasets must be considered in this light; while the data are not inconsistent with the presence of a small column of gas along the line of sight, they do not provide conclusive evidence that such a column exists. Attempts to fit the data to this model with a frozen powerlaw showed no datasets with significant column densities to 3σ significance.

The best-fit parameters for the oxygen edge energies for the Method C data sets are as shown in Table A.8. No statistically significant variation is seen. Table A.9 shows the same data for the Method D data sets; again, the variations in oxygen edge depth are not statistically significant.

Data Set	O VII	O VIII	$L_x(10^42erg/s)$	χ^2/dof
ab1	$\varepsilon = 0.718^{\pm.022}$	$\varepsilon = 0.875^{+.046}_{-.040}$	14.08	1.043
a2	$\varepsilon = .712^{+0.015}_{-0.009}$	$\varepsilon = .865^{+0.047}_{-0.056}$	16.24	1.041
a3	$\varepsilon = 0.725^{+0.009}_{-0.013}$	$\varepsilon = 0.871$	15.75	1.071
a4	$\varepsilon = 0.723^{+0.012}_{-0.014}$	$\varepsilon = .8496^{+0.0504}_{-0.0496}$	15.84	1.216
b2	$\varepsilon = 0.715^{+0.004}_{-0.012}$	$\varepsilon = 0.891^{\pm0.11}$	12.63	1.038
b3	$\varepsilon = 0.726^{\pm0.012}$	$\varepsilon = 0.850^{+0.113}_{-0.342}$	12.25	1.100
b4	$\varepsilon = 0.725^{+0.013}_{-0.020}$	$\varepsilon = 0.850^{0.113}_{-0.342}$	12.08	1.026
c1	$\varepsilon = .7186^{+0.0176}_{0.0267}$	$\varepsilon = .8751^{+0.025}_{-0.0751}$	10.89	1.156
c2	$\varepsilon = .7229^{+0.0111}_{-0.0145}$	$\varepsilon = 8745^{+0.0255}_{-0.0578}$	10.83	1.219
c3	$\varepsilon = 0.719^{+0.014}_{-0.02}$	$\varepsilon = 0.879^{+0.109}_{-0.098}$	10.52	0.9930
c4	$\varepsilon = .7210^{+0.0189}_{-0.0307}$	$\varepsilon = .8447^{+0.553}_{0.447}$	10.28	1.001
d1	$\varepsilon = .7185^{+0.0116}_{-0.0219}$	$\varepsilon = 0.9000_{-0.0219}$	6.748	1.191
d2	$\varepsilon = 0.705^{+0.017}_{-0.024}$	$\varepsilon = 0.878^{\pm0.046}$	8.201	1.108
d34	$\varepsilon = 0.729^{+0.016}_{-0.024}$	$\varepsilon = 0.869^{+0.102}_{-0.411}$	8.047	1.015

Table A.9: Here the values of the best-fit energy ε for O VII and O VIII absorption edges are shown for spectra selected by Method D.

APPENDIX C

METHOD A DATA SETS OF MCG-6-30-15

Data Set	Time interval (ksec)	Exposure(sec)	SIS0 counts	Count rate
t1	0-20	8,594	14,291	1.663
t2	20-40	6,261	15,401	2.460
t3	40-60	9,273	21,837	2.355
t4	60-80	6,461	10,760	1.665
t5	80-100	9,646	19,580	2.030
t6	100-120	7,520	17,796	2.367
t7	120-140	9,002	27,196	3.021
t8	140-160	7,920	25,903	3.271
t9	160-180	9,202	24,409	2.653
t10	180-200	8,276	16,755	2.025
t11	200-220	8,508	20,034	2.355
t12	220-240	8,460	16,607	1.963
t13	240-260	6,789	14,058	2.071
t14	260-280	9,627	21,266	2.209
t15	280-300	7,501	14,331	1.911
t16	300-320	9,957	16,393	1.646
t17	320-340	7,676	10,684	1.392
t18	340-360	10,721	9,636	0.8988

Table A.10: Selection criteria and characteristics of each of the 18 spectra selected by sequential time filters .

This appendix contains details of the temporally-selected datasets from the long observation of MCG-6-30-15 to supplement the summary given in Chapter 5. These measurements are equivalent to the previously published results of Otani *et. al.* (1995) and Reynolds (1996), and serve the purpose of demonstrating that the results presented in Chapter 5 are not an artificat of the fitting procedure used.

Selection Criteria for Temporal Data Sets

The observation was divided into 18 spectra from each consecutive 20 ksec of the observation, and denoted by the labels t1, t2, t3....t18; t1 corresponds to the first 20 ksec of the observation, t2 to the second 20 ksec of the observation, and so forth.

Data Set	Photon Index	χ^2	d.o.f.
t1	$2.00^{+0.32}_{-0.27}$	49.05	69
t2	$1.96^{+0.32}_{-0.27}$	76.01	82
t3	$2.07^{+0.24}_{-0.21}$	113.0	121
t4	$1.81^{+0.33}_{-0.28}$	84.56	73
t5	$1.78^{+0.21}_{-0.19}$	120.5	122
t6	$2.12^{+0.29}_{-0.25}$	75.21	103
t7	$1.98^{+0.21}_{-0.19}$	115.4	131
t8	$2.03^{+0.20}_{-0.18}$	140.4	145
t9	$1.84^{+0.20}_{-0.18}$	144.9	139
t10	$1.88^{+0.25}_{-0.22}$	110.5	115
t11	$2.02^{+0.25}_{-0.22}$	136.0	109
t12	$1.82^{+0.25}_{-0.22}$	93.66	106
t13	$1.99^{+0.29}_{-0.25}$	77.67	90
t14	$1.92^{+0.22}_{-0.20}$	118.3	175
t15	$1.88^{+0.30}_{-0.26}$	74.39	91
t16	$1.92^{+0.24}_{-0.21}$	118.9	110
t17	$1.78^{+0.32}_{-0.27}$	82.39	115
t18	$1.72^{+0.33}_{-0.28}$	61.64	68

Table A.11: Photon Indices for Temporal Data Selection. Confidence regions shown are 3σ.

The characteristics of these states are described in Table A.10.

Spectral Analysis of Temporal Data Sets

The photon indices of the temporal spectra were measured in the same manner as for the average spectrum of the observation. The results are shown in Table A.11. While the results are suggestive of a photon index change during the deep minimum at the end of the observation, the results are statistically consistent with the value obtained for the total observation of 1.88.

Table A.12 contains several points worth noting. First, the two photon indices of this model are different to 1σ significance for several of the datasets, suggesting

Data Set	Γ_1	ε_{break}	Γ_2	χ^2	d.o.f.
t1	$1.80^{+0.19}_{-0.19}$	8.79	10	125.9	146
t2	$1.79^{+0.21}_{-0.31}$	5	$1.75^{+0.38}_{-0.34}$	144.1	149
t3	$1.96^{+0.15}_{-0.15}$	9.0	3.1	206.0	217
t4	$1.76^{+0.21}_{-0.20}$	8.8	10	141.8	129
t5	1.56 ± 0.18	$6.18^{+1.48}_{-0.74}$	$2.27^{+0.63}_{-0.54}$	222.9	222
t6	$1.92^{+0.17}_{-0.16}$	9.0	-2.4	173.6	188
t7	$1.74^{+0.16}_{-0.16}$	6.4	$2.55^{+0.72}_{-0.61}$	236.1	244
t8	$1.759^{+0.155}_{-0.154}$	$6.37^{+0.77}_{-0.65}$	$2.83^{+0.71}_{-0.61}$	230.7	266
t9	$1.83^{+0.14}_{-0.13}$	9.0	-1.5	239.1	252
t10	$1.72^{+0.20}_{-0.20}$	6.33	$2.39582^{+0.85}_{-0.68}$	198.4	193
t11	$1.84^{+0.17}_{-0.15}$	$8.82_{-0.61}$	9.99995	243.2	199
t12	$1.81^{+0.16}_{-0.16}$	8.46	$2.3^{+3.7}_{-2.6}$	168.2	191
t13	$1.95^{+0.18}_{-0.17}$	8.89	-3	172.7	162
t14	1.88612	9.0	0.976233	241.9	269
t15	$1.73^{+0.20}_{-0.21}$	$6.78^{+2.22}_{-0.86}$	$2.75^{+1.41}_{-1.08}$	154.9	161
t16	$1.72^{+0.15}_{-0.15}$	8.8	$10_{-8.6}$	241.7	204
t17	$1.67^{+0.20}_{-0.19}$	9.0	10	145.6	176
t18	1.53 ± 0.19	$8.62^{+0.38}_{-0.78}$	10	125.9	133

Table A.12: Broken Photon Indices for Temporal Data. Confidence regions shown are 1σ.

Data Set	Γ	α	χ^2	d.o.f.
t1	$1.78^{+0.30}_{-0.26}$	$0.18^{+0.30}_{-0.18}$	53.78	79
t2	$1.76^{+0.28}_{-0.25}$	$0.16^{+0.28}_{-0.16}$	79.03	84
t3	$1.82^{+0.21}_{-0.19}$	$0.22^{+0.21}_{-0.19}$	116.5	124
t4	$1.72^{+0.31}_{-0.27}$	$0.12^{+0.31}_{-0.12}$	85.31	72
t5	$1.68^{+0.20}_{-0.18}$	$0.08^{+0.11}_{-0.08}$	126.2	124
t6	$1.83^{+0.25}_{-0.22}$	$0.23^{+0.25}_{-0.22}$	81.40	106
t7	$1.79^{+0.19}_{-0.18}$	$0.19^{+0.19}_{-0.18}$	116.0	134
t8	$1.83^{+0.19}_{-0.17}$	$0.22^{+0.19}_{-0.17}$	147.5	148
t9	$1.73^{+0.19}_{-0.17}$	$0.13^{+0.19}_{-0.13}$	146.9	141
t10	$1.75^{+0.23}_{-0.20}$	$0.15^{0.23}_{-0.15}$	113.9	115
t11	$1.80^{+0.23}_{-0.20}$	$0.19^{+0.23}_{-0.19}$	140.5	110
t12	$1.74^{+0.23}_{-0.21}$	$0.14^{+0.23}_{-0.14}$	100.9	108
t13	$1.82^{+0.27}_{-0.24}$	$0.22^{+0.27}_{-0.22}$	82.17	90
t14	$1.75^{+0.20}_{-0.18}$	$0.15^{+0.20}_{-0.15}$	120.7	177
t15	$1.78^{+0.27}_{-0.24}$	$0.18^{0.27}_{-0.18}$	80.76	92
t16	$1.78^{+0.22}_{-0.20}$	$0.18^{+0.22}_{-0.18}$	128.0	111
t17	$1.70^{+0.39}_{-0.26}$	$0.10^{+0.29}_{-0.10}$	82.76	115
t18	$1.67^{+0.39}_{-0.26}$	$0.07^{+0.30}_{-0.07}$	61.99	68

Table A.13: Absorption by Dust for Temporal Data. Confidence regions shown are 3σ.

that the physics of the continuum is more than a simple powerlaw. Second, unlike the single photon index model, we see variations in the low energy powerlaw for this dataset. The softer powerlaw for the last four datasets is almost certainly the result of inclusion of a few counts from the Fe Kα absorption line, which does not correlate to the physics of the continuum.

The datasets extracted according to Method A are analyzed first, with best-fit parameters shown in Table A.13. Here we see no significant variation in the photon index, which is consistent with the findings of the simple powerlaw model. All datasets are within 3σ error of the powerlaw slope of Γ=1.88 measured for the average spectrum. Some evidence for the presence of dust in the line of sight exist; the

Data Set	Γ	N_h	χ^2	d.o.f.
t1	$1.98^{+0.28}_{-0.24}$	$0.0^{+3.8}$	53.99	82
t2	$1.91^{+0.27}_{-0.24}$	$0.0^{+3.9}$	81.36	85
t3	$2.03^{+0.21}_{-0.19}$	$0.0^{+2.7}$	116.5	126
t4	$1.84^{+0.29}_{-0.26}$	$0.0^{+4.4}$	86.95	75
t5	$1.95^{+0.20}_{-0.18}$	$3.1^{+4.7}_{-3.1}$	124.8	127
t6	$2.05^{+0.25}_{-0.22}$	$0.0^{+3.0}$	81.40	107
t7	$2.02^{+0.19}_{-0.18}$	$0.85^{+3.09}_{-0.85}$	118.1	136
t8	$2.28^{+0.19}_{-0.18}$	$4.2^{+5.6}_{-3.2}$	145.3	150
t9	$1.85^{+0.18}_{-0.17}$	$0.0^{+2.4}$	146.9	144
t10	$2.22^{+0.23}_{-0.21}$	$6.7^{+43.1}_{-4.8}$	111.1	119
t11	$2.18^{+0.23}_{-0.20}$	$3.3^{+6.2}_{-3.3}$	139.6	113
t12	$1.94^{+0.23}_{-0.20}$	$1.1^{+3.8}_{-1.1}$	100.7	110
t13	$2.04^{+0.26}_{-0.23}$	$0.01^{+3.9}_{-0.01}$	82.20	92
t14	$2.09^{+0.21}_{-0.19}$	$2.6^{+4.3}_{-2.6}$	122.3	179
t15	$2.08^{+0.27}_{-0.24}$	$1.8^{+5.3}_{-1.8}$	80.37	94
t16	$2.22^{+0.23}_{-0.20}$	$4.9^{+9.1}_{-4.0}$	127.9	114
t17	$1.79^{+0.28}_{-0.25}$	$0^{+3.7}$	82.95	117
t18	$1.86^{+0.29}_{-0.25}$	$1.6^{+5.9}_{-1.6}$	62.46	71

Table A.14: Partial absorption by Gas for Temporal Data. Confidence regions shown are 1σ.

datasets t3,t6,t7, and t8 all have $\alpha > 0$ to 3σ significance. The data are consistent with a constant absorption index $\alpha = 0.14$ found for the average spectrum.

Next, the possibility that the properties of a column of absorbing gas might vary is examined. The best-fit parameters for the data selected using Method A are shown in Table A.14. Several of the datasets show deviation in photon index from both that determined by the simple powerlaw model for the average spectrum ($\Gamma_{ave} = 1.88$) and that determined for the partial absorption model for the average spectrum; datasets t8, t10, t11, and t16 all have photon indices higher than this value to within 1σ significance. Only two of the datasets differ significantly from one another; t17 has a lower photon index than does t8. Three datasets (t8, t10, and t16) have N_h

Data Set	O VII	O VIII	$L_x(10^{42} erg/s)$	χ^2/dof
t1	$\varepsilon = 0.724^{+0.020}_{-0.026}$	$\varepsilon = 0.854^{+0.131}_{-0.281}$	9.291	1.018
t2	$\varepsilon = 0.723^{+0.018}_{-0.020}$	$\varepsilon = 0.871^{+0.151}_{-0.119}$	14.05	1.056
t3	$\varepsilon = 0.727^{+0.016}_{-0.012}$	$\varepsilon = 0.950$	13.52	1.045
t4	$\varepsilon = 0.714^{+0.018}_{-0.026}$	$\varepsilon = 0.933^{+0.106}_{-0.123}$	9.575	1.001
t5	$\varepsilon = 0.722^{+0.013}_{-0.018}$	$\varepsilon = 0.870^{+0.108}_{-0.104}$	11.85	1.138
t6	$\varepsilon = 0.725^{+0.016}_{-0.020}$	$\varepsilon = 0.846^{+0.104}_{-0.460}$	13.59	1.021
t7	$\varepsilon = 0.726^{+0.010}_{-0.021}$	$\varepsilon = 0.871^{noerr}$	17.10	1.117
t8	$\varepsilon = 0.723^{+0.011}_{-0.015}$	$\varepsilon = 0.858^{+0.056}_{-0.074}$	19.16	0.9865
t9	$\varepsilon = 0.714^{+0.094}_{-0.033}$	$\varepsilon = 0.900^{+0.050}_{-0.100}$	15.77	1.038
t10	$\varepsilon = 0.710^{+0.016}_{-0.021}$	$\varepsilon = 0.862^{+0.081}_{-0.069}$	11.76	1.125
t11	$\varepsilon = 0.717^{+0.006}_{-0.018}$	$\varepsilon = 0.871^{noerr}$	13.53	1.116
t12	$\varepsilon = 0.724^{+0.015}_{-0.023}$	$\varepsilon = 0.864^{+0.104}_{-0.079}$	11.42	1.062
t13	$\varepsilon = 0.723^{+0.016}_{-0.021}$	$\varepsilon = 0.875^{+0.078}_{-0.077}$	11.97	1.055
t14	$\varepsilon = 0.717^{+0.013}_{-0.020}$	$\varepsilon = 0.913^{+0.046}_{-0.072}$	12.71	1.092
t15	$\varepsilon = 0.727^{+0.016}_{-0.033}$	$\varepsilon = 0.864^{+0.102}_{-0.104}$	11.02	1.000
t16	$\varepsilon = 0.718^{+0.013}_{-0.024}$	$\varepsilon = 0.898^{+0.039}_{-0.046}$	9.835	1.141
t17	$\varepsilon = 0.721^{+0.021}_{-0.024}$	$\varepsilon = 0.904^{+0.137}_{-0.046}$	7.982	1.006
t18	$\varepsilon = 0.714^{+0.029}_{-0.033}$	$\varepsilon = 0.894^{+0.056}$	5.081	1.289

Table A.15: The best-fit edge energy ε is tabulated together with 3σ uncertainty limits for both the O VII and O VIII absorption edges.

significantly higher than the value for the average spectrum of the observation; these are the only datasets which have gas column density which differs significantly from zero.

Table A.15 shows the best-fit energies for the oxygen absorption edges; the edge energies remain constant to well within measurement error.

Finally, we attempt to fit the data with a one-zone photoionization model. The results are as shown in Table A.16. Here the data are fit with the tables created by ION with a 50% covering factor; as before, they are statistically indistinguishable from the 100% covering factor; the column density is adjusted to compensate.

Data Set	Column Density	U	$L_x x10^{42} erg/s$	χ^2/dof
t1	$21.3891^{+0.0569}_{-0.0642}$	$.407306^{+0.1480}_{-0.1868}$	9.557	1.098
t2	$21.4441^{+0.0426}_{-0.0427}$	$.4577^{+0.1045}_{-0.1548}$	14.46	1.101
t3	$21.4510^{+0.0391}_{-0.0378}$	$.5307^{+0.0782}_{-0.1040}$	13.82	1.110
t4	$21.5463^{+0.0437}_{-0.0508}$	$.5000^{+0.1094}_{0.1554}$	9.958	1.039
t5	$21.5024^{+0.0335}_{-0.0284}$	$.3935^{+0.0959}_{-0.0817}$	12.30	1.214
t6	$21.4066^{+0.0411}_{-0.0417}$	$.4887^{+0.0992}_{-0.1855}$	13.83	1.100
t7	$21.2882^{+0.0422}_{-0.0288}$	$.2798^{+0.1337}_{-0.0972}$	17.23	1.237
t8	$21.4120^{+0.0377}_{-0.00277}$	$.3130^{+0.1324}_{-0.0819}$	19.45	1.111
t9	$21.4619^{+0.0221}_{-0.0253}$	$.1778^{+0.0696}_{-0.0978}$	16.26	1.093
t10	$21.4499^{+0.0371}_{-0.0295}$	$.2380^{+0.1452}_{-0.1005}$	12.12	1.168
t11	$21.3930^{+0.0227}_{-0.0308}$	$.1896^{+0.0896}_{-0.1000}$	13.90	1.201
t12	$21.4999^{+0.0387}_{-0.0358}$	$.4296^{+0.1015}_{-0.1078}$	11.81	1.100
t13	$21.5164^{+0.0421}_{-0.0484}$	$.5078^{+0.0962}_{-0.1445}$	12.41	1.180
t14	$21.4094^{+0.0348}_{-0.0419}$	$.3674^{+0.1127}_{-0.1162}$	12.93	1.198
t15	$21.5169^{+0.0424}_{-0.0535}$	$.5370^{+0.0851}_{-0.1501}$	11.42	1.079
t16	$21.7345^{+0.0359}_{-0.0359}$	$.7282^{+0.0591}_{-0.0636}$	10.50	1.203
t17	$21.7516^{+0.0403}_{-0.0425}$	$.8321^{+0.0540}_{-0.0644}$	8.564	1.078
t18	$22.1059^{+0.0246}_{-0.0665}$	$1.014^{+0.020}_{-0.070}$	5.755	1.296

Table A.16: The best-fit parameters from the photoionization code ION are shown. In all cases except t17 and t18 the slope used was 1.9; for t17 and t18 a slope of 1.7 consistently gave better fitting statistics.

APPENDIX D

METHOD B DATA SETS OF MCG-6-30-15

Data Set	Criterion	Exposure	SIS0 counts	Count Rate
l1	$C > C_a + 2\sigma$	6,843	25,753	3.76
l2	$C_a + \frac{3}{2}\sigma < C < C_a + 2\sigma$	7,064	22,915	3.24
l3	$C_a + \sigma < C < C_a + \frac{3}{2}\sigma$	14,487	41,699	2.88
l4	$C_a + \frac{3}{4}\sigma < C < C_a + \sigma$	6,494	17,273	2.658
l5	$C_a + \frac{1}{2}\sigma < C < C_a + \frac{3}{4}\sigma$	12,118	30,251	2.50
l6	$C_a + \frac{1}{4}\sigma < C < C_a + \frac{1}{2}\sigma$	14,003	32,374	2.31
l7	$C_a < C < C_a + \frac{1}{4}\sigma$	15,889	33,803	2.13
l8	$C_a - \frac{1}{4}\sigma < C < C_a$	9,985	19,735	1.98
l9	$C_a - \frac{1}{2}\sigma < C < C_a - 0.25\sigma$	16,300	29,988	1.84
l10	$C_a - \frac{3}{4}\sigma < C < C_a - \frac{1}{2}\sigma$	13,474	22,395	1.66
l11	$C_a - \sigma < C < C_a - \frac{3}{4}\sigma$	10,330	15,113	1.46
l12	$C_a - \frac{3}{2}\sigma < C < C_a - \sigma$	11,819	14,610	1.24
l13	$C < C_a - \frac{3}{2}\sigma$	12,508	9,556	0.764

Table A.17: Here the criteria and features of spectra selected by luminosity (Method B) are shown. The quantities C_a and σ were obtained from the statistics of the combined light curve for the observation.

This Appendix contains the results of spectral analysis of luminosity filtered (Method B) data sets for MCG-6-30-15.

Selection Criteria for Luminosity Selected Data Sets

The spectra was also divided into 12 luminosity-selected bins, denoted l1 (a spectra from the states with the highest luminosities) through l12 (a spectra from the states with the lowest luminosities). The characteristics of the luminosity- selected states are described in detail in Table A.17. The cutoffs for the luminosity-selected spectra were chosen in two manners; first, they were based upon the statistics of the light curve, and second, they were chosen so that each set would have a roughly equitable exposure time.

When dividing a long observation into smaller pieces to analyze the time variation of spectral features, most observers confine themselves to either strict temporal binning, in which they take extract spectra from each consecutive 20 ksec of the observation, or by luminosity filters, in which they group events on the light curve with the similar luminosities into spectra. Previous analyses of this observation have already used these methods, most notably Otani *et.al.* (1995), Reynolds and Fabian (1995), and Iwasawa *et.al.* (1996). These methods, while rigorous, have several drawbacks. Temporal selection ignores the variations of the source on timescales shorter than the usual 20 ksec binning time, despite the fact that many AGN (including the present target) are known to vary on timescales of minutes. Luminosity filtering methods are non-ideal because they do not differentiate between states of the same luminosity which are far separated in the observation, and could then have different physics, nor do they distinguish between different dynamic behavior, such as increasing, decreasing, or extremal states, of the same luminosity.

Spectral Analysis for Luminosity Selected Data Sets

Some spectral features (such as the iron lineshape) vary with the the luminosity of the source. The Method B datasets are ideal for showing whether the continuum slope is one of these; they are fit to the simple powerlaw model with best-fit parameters shown in Table A.18.

While Table A.18 shows that the photon indices of each data set are within error of the photon index of the spectrum of the complete observation, several datasets are not satisfactorily fit by a single photon index model.

Data Set	Photon Index	χ^2	d.o.f.
l1	$2.05^{+0.24}_{-0.22}$	104.3	159
l2	$2.01^{+0.23}_{-0.20}$	101.1	142
l3	$2.04^{+0.21}_{-0.19}$	181.4	166
l4	$2.13^{+0.24}_{-0.22}$	138.6	125
l5	$2.06^{+0.20}_{-0.18}$	140.5	167
l6	$2.03^{+0.19}_{-0.18}$	153.2	175
l7	$1.90^{+0.21}_{-0.19}$	136.6	157
l8	$2.01^{+0.20}_{-0.18}$	157.5	171
l9	$2.07^{+0.19}_{-0.17}$	196.3	211
l10	$1.86^{+0.21}_{-0.19}$	138.1	135
l11	$1.83^{+0.19}_{-0.17}$	192.4	180
l12	$1.97^{+0.18}_{-0.17}$	222.5	193
l13	$1.89^{+0.21}_{-0.19}$	211.5	220

Table A.18: Photon Indices for each dataset of the Luminosity Filtered Regions. Confidence regions shown are 3σ.

Next, the possibility that the shape of the continuum has changes correlated with luminosity is examined. Datasets extracted using Method B were fit to the broken powerlaw model with results as shown in Table A.19.

Here some variation in the lower photon index Γ_1 is evident; in particular, dataset l9 has a photon index higher than that of datasets l10,l11,l12, and l13, as well as than the average photon index for the simple powerlaw model of the total observation, $\Gamma_{ave} = 1.88$. One dataset (l7) has a break energy within the iron Kα energy range, and serves only to show that the photon indices above and below this feature do not differ substantially from one another. The rest of the datasets have break energies above 8 keV, suggesting that any differences between Γ_1 and Γ_2 should be interpreted in the context of the beginning of the cold reflection feature seen in GINGA observations of this object. While the confidence regions for Γ_1 are small enough to draw conclusions about the continuum, many of the confidence regions for Γ_2 exceeded the limits

Data Set	Γ_1	ε_{break}	Γ_2	χ^2	d.o.f.
l1	$2.02^{+0.13}_{-0.12}$	9.0	8.8	103.2	156
l2	$2.05^{+0.13}_{-0.12}$	8.8	-1.3	99.73	138
l3	$2.03^{+0.11}_{-0.11}$	9.0	2.7	181.4	163
l4	$2.17^{+0.13}_{-0.13}$	9.0	-3	136.0	121
l5	$2.04^{-0.11}_{-0.10}$	8.6	1.7	138.6	163
l6	$2.08^{+0.11}_{-0.10}$	8.4 ± 0.8	$0.89^{+2.25}_{-1.8}$	149.2	170
l7	$1.96^{+0.20}_{-0.20}$	5.0	$1.81^{+0.21}_{-0.19}$	135.4	153
l8	$2.03^{+0.12}_{-0.10}$	8.6	0.97	155.1	168
l9	$2.12^{+0.10}_{-0.09}$	9.0	-3	191.3	206
l10	$1.79^{+0.12}_{-0.11}$	8.7	$10_{-5.8}$	133.2	133
l11	$1.83^{+0.10}_{-0.10}$	9.0	2.11	191.0	176
l12	$1.88^{+0.10}_{-0.10}$	8.6	$10_{-4.6}$	209.7	189
l13	$1.89^{+0.12}_{-0.11}$	9.0	2.4	211.3	215

Table A.19: Broken Photon Indices for Luminosity Data. Confidence regions shown are 1σ; confidence regions for Γ_2 are omitted when they exceed the soft limits for that parameter.

available for the model, and thus are not available.

Next, the possibility that the characteristics of reflection vary with luminosity is explored using datasets extracted by Method B. The best-fit parameters are shown in Table A.20.

The datasets extracted by Method B all overlap the 3σ confidence limits of $\Gamma_{ave} = 1.88$, confirming the results from Method A that any reflective geometry remains constant over the observation. The only change seen is in Ω, which again varies widely, but this variation does not achieve statistical significance.

The possibility that the properties of the dust in the line of sight depends on the luminosity of the galaxy is explored in Table A.21, which shows the best-fit parameters for spectra selected by Method B.

This dataset is consistent with constant photon index 1.88 of the simple powerlaw

Data Set	Γ	ϵ	*theta*	Ω	χ^2	d.o.f.
l1	$1.95^{+0.30}_{-0.28}$	1.0	28.7	1.04	108.4	163
l2	$2.13^{+0.21}_{-0.33}$	1.0	31.3	2.0	103.7	145
l3	$1.87^{+0.36}_{-0.18}$	1.0	28.2	2.0	186.7	171
l4	$2.23^{+0.23}_{-0.34}$	1.0	31.3	1.96	144.8	129
l5	$1.86^{+0.36}_{-0.17}$	1.0	34.5	2.0	144.8	174
l6	$2.16^{+0.18}_{-0.30}$	1.0	31.5	1.96	157.7	181
l7	$1.83^{+0.25}_{-0.24}$	1.0	29.1	1.0	138.6	164
l8	$2.15^{+0.18}_{-0.31}$	1.0	31.4	1.0	162.1	179
l9	$2.21^{+0.17}_{-0.30}$	1.0	31.3	2.0	201.0	220
l10	$1.68^{+0.36}_{-0.18}$	1.0	28.3	2.0	148.4	141
l11	$1.75^{+0.25}_{-0.24}$	1.0	28.9	1.0	195.9	187
l12	$1.75^{+0.30}_{-0.16}$	1.0	28.3	2.0	229.2	201
l13	$1.72^{+0.36}_{-0.19}$	1.0	28.3	2.0	213.0	226

Table A.20: Partial absorption by Gas for Method B Data. Confidence regions shown are 3σ.

Data Set	Γ	α	χ^2	d.o.f.
l1	$1.81^{+0.27}_{-0.23}$	$0.21^{+0.27}_{-0.21}$	101.7	153
l2	$1.81^{+0.25}_{-0.22}$	$0.21^{+0.25}_{-0.21}$	92.99	134
l3	$1.78^{+0.23}_{-0.20}$	$0.19^{+0.23}_{-0.19}$	174.7	158
l4	$1.85^{+0.28}_{-0.24}$	$0.25^{+0.82}_{-0.16}$	134.1	117
l5	$1.81^{+0.22}_{-0.20}$	$0.24^{+0.22}_{-0.20}$	136.6	158
l6	$1.82^{+0.22}_{-0.20}$	$0.22^{+0.22}_{-0.20}$	144.6	164
l7	$1.74^{+0.23}_{-0.21}$	$0.15^{+0.23}_{-0.15}$	129.1	148
l8	$1.82^{+0.23}_{-0.20}$	$0.22^{+0.23}_{-0.20}$	152.8	161
l9	$1.84^{+0.21}_{-0.19}$	$0.24^{+0.21}_{-0.19}$	193.9	201
l10	$1.71^{+0.23}_{-0.20}$	$0.15^{+0.23}_{-0.15}$	136.1	128
l11	$1.72^{+0.21}_{-0.19}$	$0.13^{+0.21}_{-0.13}$	186.9	168
l12	$1.74^{+0.19}_{-0.18}$	$0.19^{+0.19}_{-0.18}$	208.6	183
l13	$1.73^{+0.24}_{-0.21}$	$0.17^{+0.24}_{-0.17}$	203.5	209

Table A.21: Absorption by Dust for Luminosity Data. Confidence regions shown are 3σ.

Data Set	Γ	N_h	χ^2	d.o.f.
l1	$2.17^{+0.25}_{-0.22}$	$1.88^{+4.75}_{-1.88}$	103.7	157
l2	$2.01^{+0.23}_{-0.20}$	$0^{+3.16}$	101.1	140
l3	$2.25^{+0.22}_{-0.11}$	$3.55^{+5.79}_{-3.28}$	179.9	164
l4	$2.32^{+0.25}_{-0.23}$	$3.19^{+6.69}_{-3.19}$	137.5	123
l5	$2.37^{+0.21}_{-0.19}$	$5.94^{+11.9}_{-4.04}$	136.7	165
l6	$2.17^{+0.20}_{-0.18}$	$2.20^{+3.78}_{-2.20}$	152.1	173
l7	$1.90^{+0.21}_{-0.19}$	$0^{+2.88}$	136.6	155
l8	$2.01^{+0.20}_{-0.18}$	$0^{+2.52}$	157.5	169
l9	$2.07^{+0.19}_{-0.17}$	$0.01^{+2.58}_{-0.01}$	196.3	209
l10	$2.18^{+0.22}_{-0.20}$	$6.41^{+42.8}_{-4.43}$	135.5	133
l11	$1.97^{+0.20}_{-0.18}$	$2.31^{+3.94}_{-2.31}$	191.3	178
l12	$2.35^{+0.19}_{-0.17}$	$7.98^{+8.06}_{-4.15}$	206.4	191
l13	$2.24^{+0.23}_{-0.38}$	$6.89^{+14.4}_{-4.52}$	206.1	218

Table A.22: Partial absorption by Gas for Luminosity Data. Confidence regions shown are 1σ.

model of the average spectrum, and also with the photon index of 1.72, the best-fit value for the average spectrum and a dust absorption model. Here the datasets l4, l5,l6, l8, l9, and l12 show dust absorption coefficients which differ significantly from 0; all the data are consistent with $\alpha = 0.14$ as found for the average spectrum. We conclude that the dust absorption does not vary significantly within the accuracy measured by these data.

Next the Method B datasets are examined in order to determine whether the physical characteristics of partial covering by gas could change with luminosity. The best-fit parameters for the partial covering model are as shown in Table A.22.

Five of the thirteen datasets selected by Method B have photon indices which are higher than that of the average spectrum to 1σ significance. These five also have column densities which are significantly nonzero, as does one dataset (l13) which has a photon index within error of the average spectrum. Three of the four lowest

Data Set	O VII	O VIII	$L_x(10^{42} erg/s)$	χ^2/dof
l1	$\varepsilon = 0.722$	$\varepsilon = 0.865^{+0.056}_{-0.070}$	20.81	1.002
l2	$\varepsilon = 0.729^{+0.010}_{-0.017}$	$\varepsilon = 0.856^{0.124}$	17.99	0.9977
l3	$\varepsilon = 0.722^{+0.008}_{-0.014}$	$\varepsilon = 0.867^{+0.070}_{-0.083}$	15.98	1.041
l4	$\varepsilon = 0.719^{+0.010}_{-0.026}$	$\varepsilon = 0.850^{+0.116}_{-0.191}$	14.60	1.018
l5	$\varepsilon = 0.724^{+0.013}_{-0.018}$	$\varepsilon = 0.871^{+0.078}_{-0.102}$	13.87	1.067
l6	$\varepsilon = 0.7174^{+0.0098}_{-0.0175}$	$\varepsilon = 0.8732^{+0.1314}_{-0.0832}$	12.69	1.098
l7	$\varepsilon = 0.7144^{+0.0093}_{-0.0152}$	$\varepsilon = 0.8700^{+0.0699}_{-0.0638}$	11.76	1.071
l8	$\varepsilon = 0.7158^{+0.0118}$	$\varepsilon = 0.8726^{+0.0193}_{-0.0914}$	10.93	0.9716
l9	$\varepsilon = 0.7210^{+0.0119}_{-0.0139}$	$\varepsilon = 0.8846^{+0.0439}_{-0.0531}$	10.19	1.064
l10	$\varepsilon = 0.7262$	$\varepsilon = 0.8809$	9.063	1.052
l11	$\varepsilon = 0.7341^{+0.0148}_{-0.0235}$	$\varepsilon = 0.8555^{+0.0482}_{-0.0626}$	8.040	1.034
l12	$\varepsilon = 0.7249^{+0.0673}_{-0.0242}$	$\varepsilon = 0.8798^{+0.0382}_{-0.0432}$	6.715	1.102
l13	$\varepsilon = .7116^{+0.0313}_{-0.0353}$	$\varepsilon = .8960^{+0.0482}_{-0.0484}$	3.943	1.271

Table A.23: The peak energy for the absorption line ε and the optical depth τ are listed for each of the spectra selected by luminosity.

luminosity datasets show high column densities, as do the datasets l3, and l5, which represent medium luminosity data.

The two previous observations used the temporally selected data to make statements about the variation of the oxygen edges with luminosity. Here we use the data selected directly according to luminosity state (Method B) to analyze this supposition; the best-fit parameters are shown in Table A.23.

The optical depth of O VIII is anticorrelated with luminosity; this finding is in agreement with the previous observations (Otani *et. al.* 1995; Reynolds 1996). The relation between luminosity and O VIII optical depth was fit with several functions; the best-fitting result came from a power relationship:

$$\tau_{08} = (2.66 \pm 0.08)e^{(0.069\pm0.014)L_{42}} + (0.78 \pm 0.22)e^{-(2.01\pm0.11)L_{42}} \quad \text{(A.9)}$$

which fits the data well partly because the highest luminosity state (which originates from the peak of the bright flare) has a slightly higher column depth than the other high luminosity states. For comparison to previous observations, we can also examine a single exponential:

$$\tau_{O8} = (1.29 \pm 0.67)\left(\frac{L}{10^{42} erg/s}\right)^{-(0.89\pm0.57)} \tag{A.10}$$

which is not within measurement error of their results. The reason for the discrepancy with the results of Reynolds (1996) is that his photon index was allowed to vary at the same time as were the edge depths. The results differ from those of Otani *et. al.* (1995) because they plotted their results against gross SIS count rate; repetition of their method showed that the SIS count rate is not linearly related to the 2–10 keV luminosity as measured by the GIS detectors because most of the counts on an SIS detector are from photons below 2 keV.

Next, we explore the variation of the one-zone photoionization model with luminosity by analyzing the Method B datasets. The best-fit parameters are as shown in Table A.24.In all cases except l12 and l13 the slope used was 1.9; for these spectra slope of 1.7 consistently gave better fitting statistics.

The ionization parameter is significantly higher for the low luminosity datasets than the high luminosity datasets, which is counterintuitive, but consistent with the previous observation that O VIII is anti-correlated to luminosity and O VII correlated to it. The key to explaining this lies in the fact that the column density of ionized

Data Set	Column Density	U	$L_x x 10^{42} erg/s$	χ^2/dof
l1	$21.3770^{+0.0376}_{-0.0346}$	$.3300^{+0.1191}_{-0.0878}$	21.17	1.131
l2	$21.3979^{+0.0283}_{-0.0387}$	$.3486^{+0.0866}_{-0.1026}$	18.30	1.113
l3	$21.4001^{+0.0265}_{-0.0193}$	$.2890^{+0.0925}_{-0.0548}$	16.35	1.197
l4	$21.3924^{+0.0350}_{-0.0305}$	$.2908^{+0.1248}_{-0.0976}$	14.98	1.106
l5	$21.4237^{+0.0363}_{-0.0295}$	$.3263^{+0.1184}_{-0.0877}$	14.20	1.133
l6	$21.4051^{+0.0318}_{-0.0247}$	$.2926^{+0.1102}_{-0.0845}$	13.11	1.188
l7	$21.4518^{+0.0317}_{-0.0288}$	$.3205^{+0.0968}_{-0.1100}$	12.18	1.171
l8	$21.4384^{+0.0328}_{-0.0258}$	$.2649^{+0.1198}_{-0.0974}$	11.30	1.008
l9	$21.4735^{+0.0278}_{-0.0269}$	$.4289^{+0.0812}_{-0.0809}$	10.53	1.162
l10	$21.4852^{+0.0375}_{-0.0352}$	$.4640^{+0.0902}_{-0.1063}$	9.479	1.146
l11	$21.5399^{+0.0283}_{-0.0338}$	$.5246^{+0.0532}_{-0.0100}$	8.328	1.107
l12	$21.5773^{+0.0454}_{-0.0450}$	$.6573^{+0.0810}_{-0.0904}$	7.037	1.194
l13	$21.7634^{+0.0442}_{-0.0485}$	$.9290^{+0.0528}_{-0.0669}$	4.265	1.334

Table A.24: The best-fit parameters from the photoionization code ION are shown.

material (U) also depends on luminosity- the low luminosity states also have substantially higher material column densities. This suggests that during the deep minimum (which corresponds to dataset l13, and the period prior to the deep minimum to l12), the source is partially obscured by a cloud of gas (and possibly dust) which decreases the overall luminosity and accounts for the extra column density of material.

APPENDIX E

SELECTION OF METHOD C AND D DATA SETS

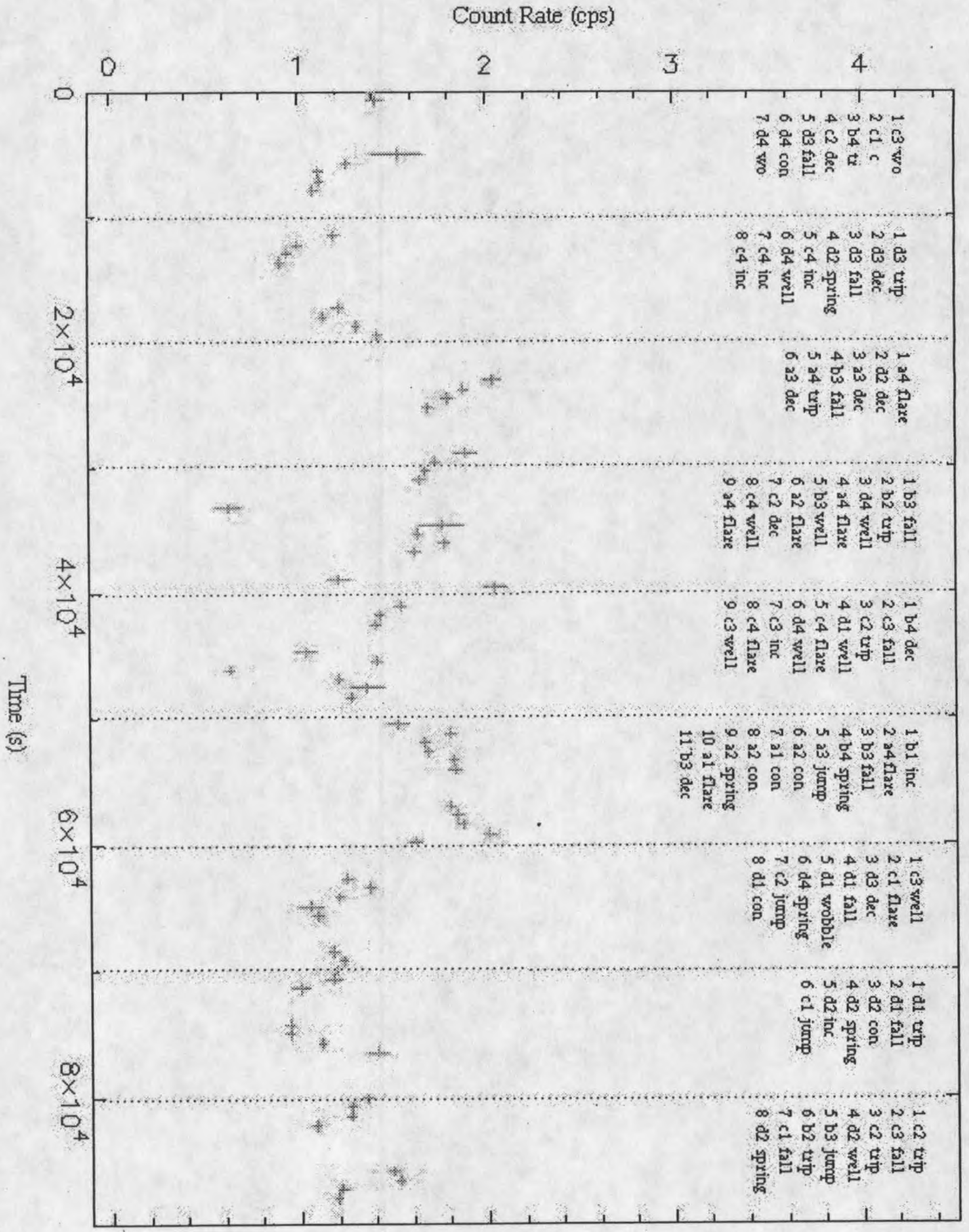

Figure A.8: Classification of each point on the light curve using the two schemes discussed in this section.

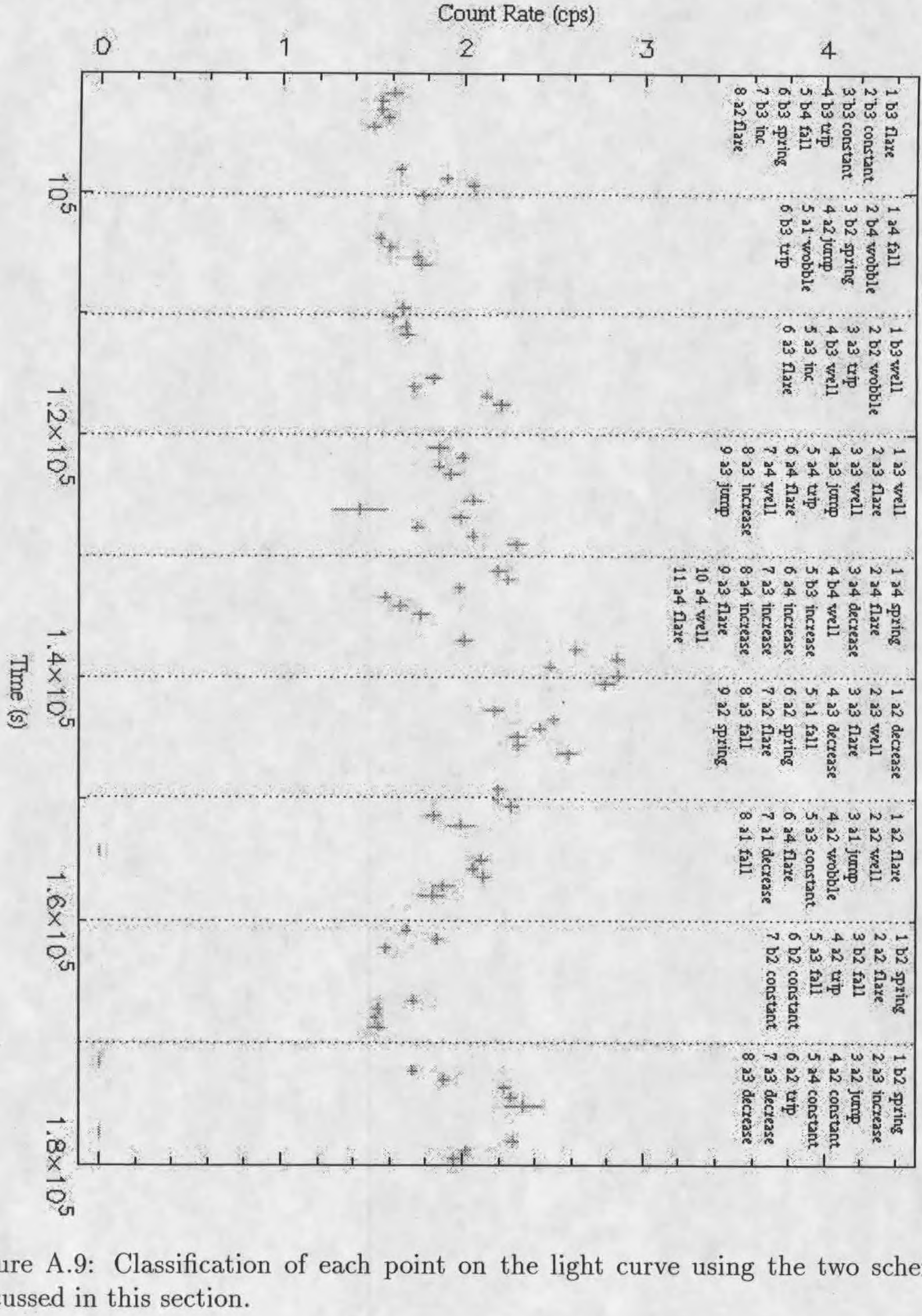

Figure A.9: Classification of each point on the light curve using the two schemes discussed in this section.

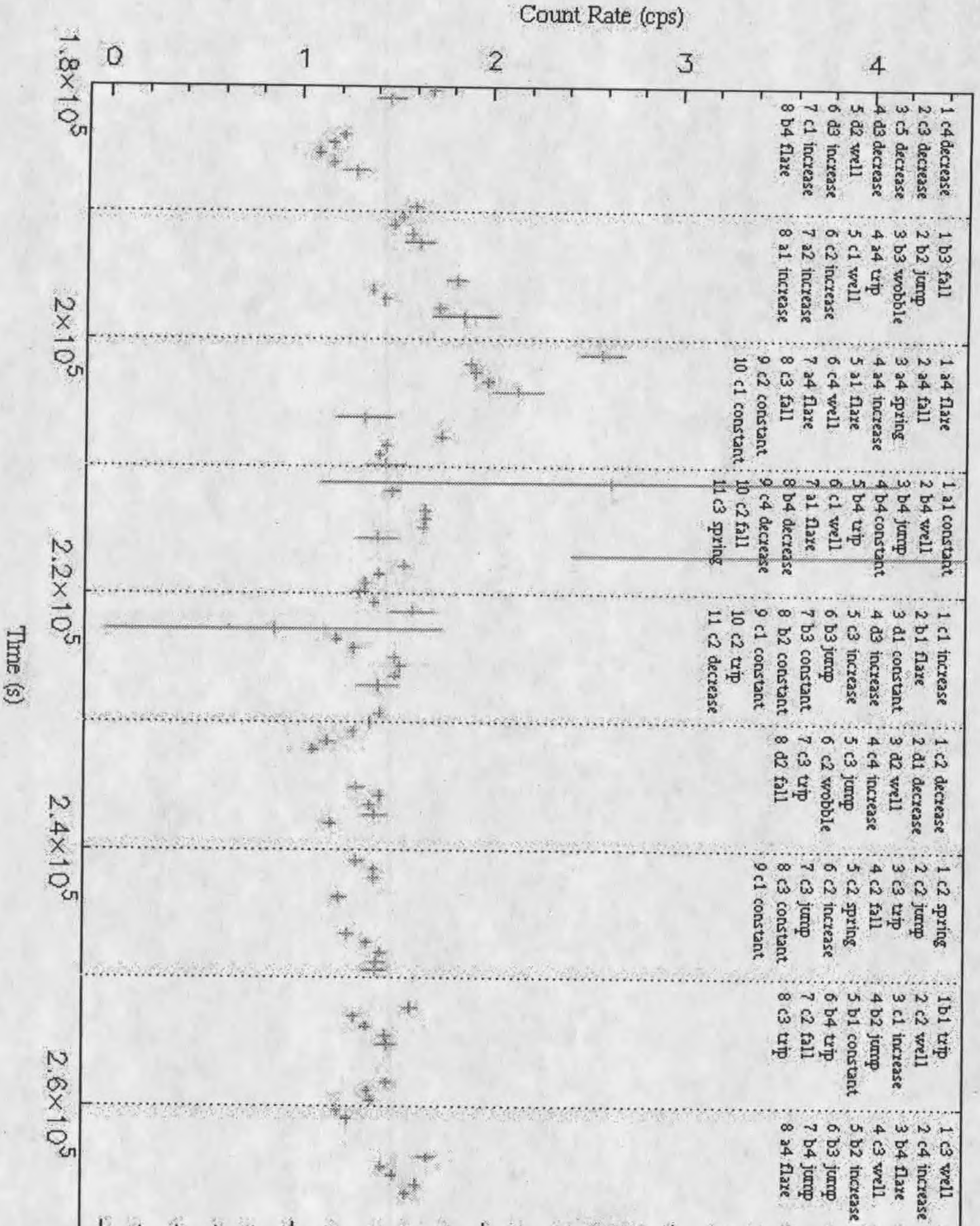

Figure A.10: Classification of each point on the light curve using the two schemes discussed in this section.

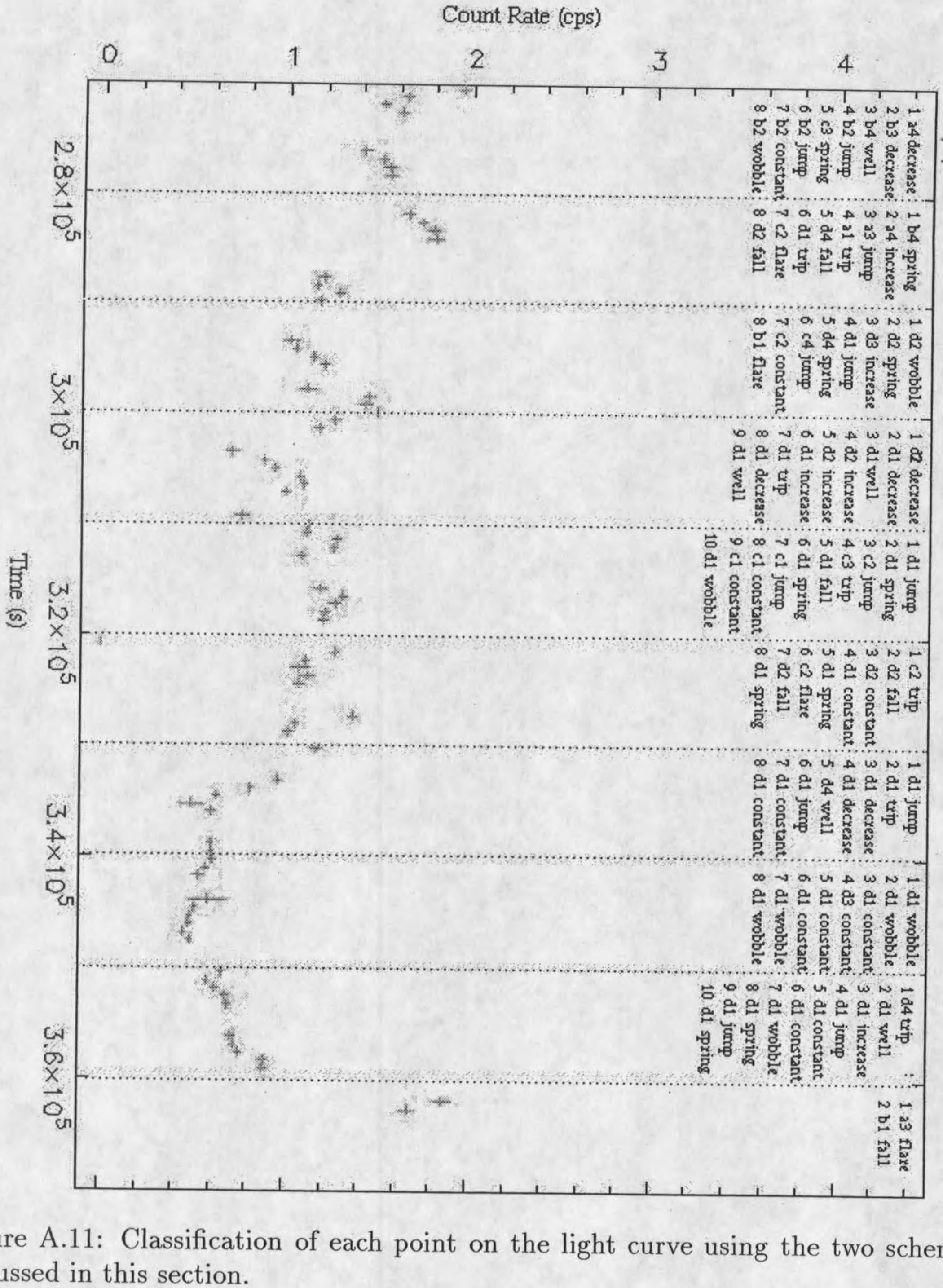

Figure A.11: Classification of each point on the light curve using the two schemes discussed in this section.